Vertical Transport of Sediment from Muddy Buoyant River Plumes in the Presence of Different Modes of Interfacial Instabilities

Mohamad Rouhnia

Dissertation submitted to the Faculty of the
Virginia Polytechnic Institute and State University
in partial fulfillment of the requirements for the degree of

Doctor of Philosophy
in
Civil Engineering

Kyle B. Strom, Chair
Jennifer L. Irish
Nina Stark
Xiaofeng Liu

August 11, 2016
Blacksburg, Virginia

Keywords: River Plume, Sediment Removal, Settling Velocity, Interface Instability, Floc

Vertical Transport of Sediment from Muddy Buoyant River Plumes in the Presence of Different Modes of Interfacial Instabilities

Mohamad Rouhnia

ABSTRACT

This study focuses on deposition processes from sediment laden buoyant river plumes in deltaic regions. The goal is to experimentally examine the effects of various physical phenomena influencing the rate at which sediment is removed from the plume. Previous laboratory and field measurements have suggested that, at times, sedimentation can take place at rates higher than that expected from individual particle settling (i.e., CW_s). Two potential drivers of enhanced sedimentation are flocculation and interfacial instabilities. We experimentally measured the sediment fluxes from each of these processes using two sets of laboratory experiments that investigate two different modes of instability, one driven by sediment settling and one driven by fluid shear. The settling-driven and shear-driven instability sets of experiments were carried out in a stagnant stratification tank and a stratification flume respectively. In both sets, continuous interface monitoring and concentration measurement were made to observe developments of instabilities and their effects on the removal of sediment. Floc size was measured during the experiments using a separate floc camera setup and image analysis routines. Results from the stratification tank experiments suggest that the settling-driven gravitational instabilities do occur in the presence of flocs, and that they can produce sedimentation rates higher than those predicted from floc settling. A simple cylinder based force balance approach adopting the concept of critical Grashof number was used to develop a model for the effective settling velocity under settling-driven

instabilities that is a function of sediment concentration in the plume only. Results from the stratification flume experiments show that under shear instabilities, the effective settling velocity is greater than the floc settling velocity, and increases with plume velocity and interface mixing. The difference between effective and floc settling velocity was denoted as the shear-induced settling velocity. This settling rate was found to be a strong function of the Richardson number, and was attributed to mixing processes at the interface. Conceptual and empirical analysis shows that the shear-induced settling velocity is proportional to URi^{-2}.

Following the experiments, analyses were made among contributions of different mechanisms on the total deposition rate, and the locations that the various mechanisms may be active in the length of a plume. This analysis leads to a conceptual discretization of a plume into three zones of sedimentation behavior and Richardson number. The first zone is the supercritical near-field plume with intense interface mixing. Zone two represents the subcritical region where interface mixing still occurs, and zone three is the high Richardson number zone where mixing at the interface is effectively nonexistent. In zones one and two, individual floc settling and shear-induced settling mechanisms play the major roles in removing sediment from the plume. While, shear-induced settling rate was found to be maximum near the river mouth, its share of the total settling rate increases in the crossshore direction, since sand and large particulates deposit near the inlet and only small particles (with relatively low settling velocity) remain as the plume propagates. The third zone, starts when the interfacial mixing diminishes and leaking commences.

This study was supported by the Petroleum Research Fund: PRF51958-ND8.

Acknowledgments

I would like to express my special appreciation and deepest gratitude to my advisor Dr. Kyle Strom, who has been an excellent mentor for me over the past few years. Thank you for all your support and guidance, and the countless hours you have invested in me. I was always amazed with your personality and professionalism, and enjoyed your organized mind, helpful ideas, and deep insights. I wish you all the best in your life and career.

I would also like to thank my other advisory committee members, Dr. Jennifer Irish, Dr. Nina Stark, and Dr. Xiaofeng Liu, for their precious time and brilliant suggestions. Thank you all for your great feedbacks and supports. I have really enjoyed working with you, and highly value each of your contributions to this effort. I should also thank the ASC, Petroleum Research Fund for providing financial support and assisting me in continuing my education. The financial support provided by the Civil and Environmental Department at Virginia Tech is gratefully acknowledged. The receipt of the Curry Fellowship was one of the most meaningful events of my graduate studies.

In addition, my thanks go out to graduate fellow students, Duc Tran and Brandon Dillon who helped in setting up the lab facilities. A special mention is necessary for Celso Castro Bolinaga whose friendship made my time in Blacksburg more enjoyable.

Finally, I take this opportunity to express the gratitude from my deep heart to my beloved parents, and wonderful sisters, whose support and love cannot be expressed in words. Last, but absolutely not least, I would like to thank my fiancee, Nina, for her love and encouragement during my pursuit of the Doctorate.

Contents

List of Figures

List of Tables

1 Introduction

1.1 Overview

Rivers are the primary pathways of sediment transport from land to ocean waters, with a yearly load of approximately 10^{10} metric tons worldwide (Milliman and Syvitski, 1992). Terrestrial sediment is in turn the host of organic carbon, nutrients, and contaminants all of which may deposit and be preserved in deltaic zones, or may be carried and mixed by ocean currents to deposit elsewhere on the shelf or deeper basin. Mud-rich freshwater discharges are often less dense than the ambient saltwater, and therefore develop into positively buoyant (hypopycnal) plumes that loft over the receiving ambient saltwater and distribute sediment over the prodelta and broader shelf region (Mulder and Syvitski, 1995; Gladstone and Pritchard, 2010). Knowledge of the mechanisms that lead to sediment removal from such plumes is an integral part of predicting where the sediment delivered to the coast eventually deposits to aid in sustaining coastal marshes, build subaqueous deltas and clinoforms, or act as source mud for wave-supported gravity flows (Syvitski et al., 1998; Maxworthy, 1999; Hill et al., 2000; McCool and Parsons, 2004; Nowacki et al., 2012). Therefore, understanding sediment removal mechanisms from mud-rich buoyant river plumes is important for understanding deltaic processes such as land building, shoaling, and the eventual building of continental shelfs.

In a buoyant plume, sediment particles descend under the influence of gravity at rates that can be defined by typical settling velocity equations (Dietrich, 1982; Ferguson and Church, 2004). Removal of sediment due to gravity acting on the particles is referred to here as individual particle settling. Most computational models and common practice set the vertical removal flux as a product of the local plume sediment concentration and the individual, gravitational settling velocity of the particulates (Hoyal et al., 1999b; Harris et al., 2005; Chen et al., 2010). However, for mud-rich river plumes, additional mechanisms potentially influence the vertical flux of sediment into the lower ambient waters. One of these processes is flocculation. Flocculation can increase the downward flux of mud from river discharges over that predicted by individual settling rate of unaggregated river sediment (Hill et al., 2000; Kineke et al., 2000; Fox et al., 2004; Partheniades, 2009; Strom and Keyvani, 2016). Flocculation, the process of aggregation and breakup of clay and silt size material, complicates the estimation of the individual particle settling velocity since floc size and density become functions of the local flow and sediment condition (Krone, 1963; Dyer, 1989; Winterwerp and van Kesteren, 2004; Strom and Keyvani, 2011). The increase of particle settling velocity due to the formation of flocs is one possible driver of enhanced sediment removal from buoyant river plumes (Hill et al., 2000).

Another mechanism that potentially influences the vertical flux of sediment is gravitational instability formation at the stratification interface of the riverine and estuarine fluids. The formation of such instabilities can lead to the onset of downward convection of particles in small negatively buoyant cells of fluid and sediment (Green, 1987; Hoyal et al., 1999a,b;

Parsons et al., 2001; McCool and Parsons, 2004; Yu et al., 2014; Burns and Meiburg, 2015). Gravitational instabilities develop in stagnant, or possibly laminar, stratified systems that are initially stable. Gravitational instabilities are classified by their initiation mechanism as double diffusive (Green, 1987; Chen, 1997; Hoyal et al., 1999a; Parsons and Garcia, 2000) or settling- driven (Hoyal et al., 1999b; Blanchette and Bush, 2005). The general outcome of either of these two initiation mechanisms is the creation of a layer of fluid near the interface that is denser than the fluid below it, leading to downward advection of the sediment laden fluid at rates that exceed the individual particle settling velocity. Interfacial instabilities can also be driven by shear between the plume and the receiving water body, and potentially enhance the vertical flux of sediment by some form of shear-induced (1) density anomaly (Maxworthy, 1999; McCool and Parsons, 2004) or (2) turbulent flux (Spahn et al., 2009; Nowacki et al., 2012).

Double-diffusive instabilities develop due to the difference in rates at which sediment, salt, and heat diffuse across the interface. The classic double-diffusion problem is that of saltwater fingering at a thermocline (Turner, 1967; Green and Kirk, 1971). In this system, salt diffuses upward into the warm freshwater layer and heat diffuses downward into the saltwater layer. The result of the two-way diffusion is an unstable band of more dense fluid near the interface that breaks into a regular and symmetric pattern of downward and upward convective fingers (Figure 1.1). Double-diffusive fingering can also occur in thermally stratified systems with warm suspensions of sediment overlying cooler clear water (Houk and Green, 1973; Green, 1987; Hoyal et al., 1999a; Parsons et al., 2001). Key in the development

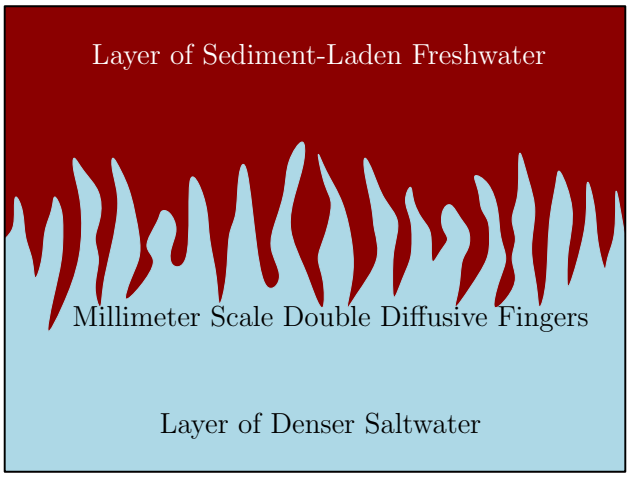

Figure 1.1: Schematic of double diffusive symmetric downward and upward convective fingers

of double-diffusive fingering for suspensions of sediment is that the sediment in the buoyant layer settles very slowly so that substance diffusion, and not particle settling, is primarily responsible for changes in the vertical density profiles (Burns and Meiburg, 2012; Yu et al., 2013; Burns and Meiburg, 2015; Yu et al., 2014). Within the band of conditions conducive to double diffusion, transport of sediment within the fingers can be a significant contribution to the total downward sediment flux (Green, 1987; Hoyal et al., 1999a). Diffusive convection process is common in warm sediment-laden plumes. However, the resulting particle scavenging rate is generally insignificant except rare extreme cases where sediment loads are extremely high and the temperature gradients are favorable (Hoyal et al., 1999a).

In settling-driven systems, the band of heightened density is generated by particles settling across the saltwater interface at a rate that is much faster than the upward diffusion of salt (Burns and Meiburg, 2012; Yu et al., 2013). This produces an unstable band of sediment-laden saltwater, the so-called interface layer, sitting between the muddy freshwater and the underlying clear saltwater (Hoyal et al., 1999b; Parsons et al., 2001; Blanchette and

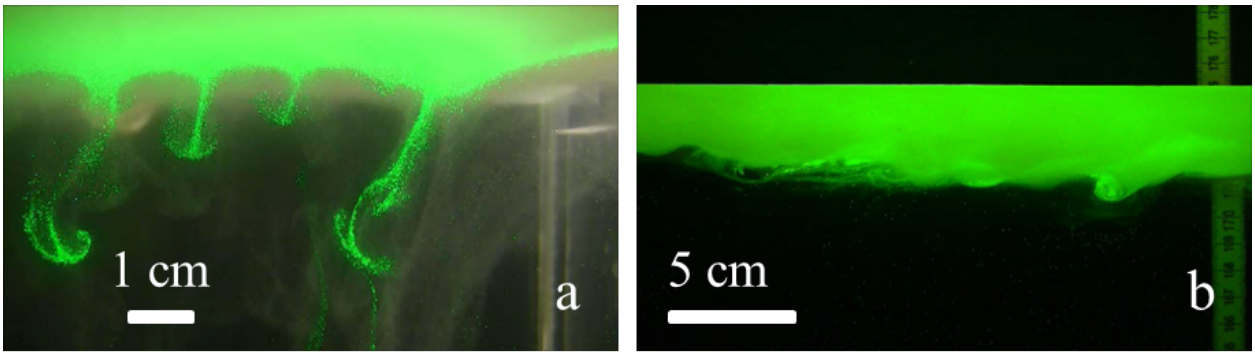

Figure 1.2: a) A snapshot of settling-driven gravitational instabilities, also known as leaks b) A snapshot of shear instabilities at the density interface of the plume and ambient saltwater

Bush, 2005). The interface layer thickens with time, and eventually breaks away in the form of leaks (Hoyal et al., 1999b; Parsons et al., 2001) (Figure 1.2a). A few defining characteristics of the settling-driven leaking mechanism are the general creation of the interface layer below the initial stratification contact, the onset of Rayleigh-Taylor generated plume like instability structures, asymmetry in the downward and upward interface motions, and centimeter-scale instability spacing, as oppose to the millimeter-scale double-diffusive generated fingering (Hoyal et al., 1999b; Burns and Meiburg, 2012; Yu et al., 2013). Within the band of conditions conducive to leaking, transport of sediment within the leaks can be a significant contribution to the total downward sediment flux (Yu et al., 2014; Burns and Meiburg, 2015).

In actively flowing river discharges, it seems less likely that double-diffusive or settling driven instabilities will form and augment or replace individual particle settling, since these instabilities have only been observed in stagnant two-layer systems. However, the difference in velocity between the two layers can produce shear instabilities in the form of Kelvin-Helmholtz vortices or Holmboe cusps at the base of the plume (Yuan and Horner-Devine,

2013) (Figure 1.2b). These instabilities are known to be important features in the exchange of water mass and momentum across the interface (Christodoulou, 1986; Geyer and Smith, 1987), and it has been suggested that they might also increase the vertical flux of sediment through the interface by creating packets of fluid and sediment within the instability that are locally more dense than the underlying ambient fluid (Raju and Meiburg, 1995; Dreier et al., 2000). The more dense packets of fluid and sediment could then lead to small downward convecting plumes that result in rapid vertical transport of sediment (Maxworthy, 1999; McCool and Parsons, 2004; Henniger and Kleiser, 2012). A related, but slightly different and more general, mechanism for enhanced removal of sediment from buoyant plumes under the effects of shear instabilities is that of turbulent diffusion across the interface (Spahn et al., 2009; Nowacki et al., 2012).

When observing different modes of interface instabilities, one is forced to consider whether or not these instabilities significantly impact the removal rate of sediment, and, if they do, under what conditions each mechanism operates over the length of a plume. The resulting vertical sediment flux due to the above mechanisms has been a topic of interest in past experimental and theoretical studies (Hoyal et al., 1999b; McCool and Parsons, 2004; Henniger and Kleiser, 2012; Yu et al., 2014; Burns and Meiburg, 2015). Previous studies have shown that the downward sediment flux can be higher than what would be expected from simple unaggregated individual particle settling, $Flux > W_s C$, in river mouth plumes (Hill et al., 2000; Kineke et al., 2000; Fox et al., 2004; McCool and Parsons, 2004; Spahn et al., 2009; Henniger and Kleiser, 2012; Nowacki et al., 2012). Some have attributed the increases

in the flux to the presence of instabilities of one kind or another (McCool and Parsons, 2004; Henniger and Kleiser, 2012; Nowacki et al., 2012; Yu et al., 2014; Burns and Meiburg, 2015). Yet, others have observed that the fluxes can be predicted using the product of the concentration and individual particle settling even in the presence of density instabilities (Hoyal et al., 1999b). The variation in flux from that of the product of local concentration with individual particle settling velocity, leads to the idea of defining an effective settling velocity, $W_{s,eff}$ to relate the actual flux of sediment to the underlying water as a function of the local plume suspended sediment concentration, C, i.e. $Flux = W_{s,eff}C$. In this way, the effective settling velocity accounts for mechanisms in addition to individual particle settling that impact the downward flux of sediment. In this dissertation, I focus on (1) experimentally identifying and quantifying the effects of settling-driven gravitational instabilities and shear instabilities on the vertical flux of suspensions of clay sediment; (2) modeling these processes in terms of an effective settling velocity; and (3) identifying the zones in which each of these mechanisms likely operate over the length of a river mouth plume. In the following section, I first present the specific research questions and hypotheses tested in each component of my study. Chapter 1 is then concluded with an overview of the approaches used to test these hypotheses. Chapters 2, 3, and 4 constitute self-contained papers on the topics of vertical flux in the presence of settling-driven instabilities (Chapter 2), shear-driven instabilities (Chapter 3), and an analysis of different vertical transport rates over the length of a plume (Chapter 4). As of the writing of this thesis, Chapter 2 has been published in the Journal of Geophysical Research: Oceans; Chapter 3 has been submitted to the same journal and

is currently under review; and Chapter 4 is in preparation and will be submitted for review soon.

1.2 Study Objectives

The overarching goal of this study is to improve understanding and modeling of the vertical transport of sediment from river mouth plumes in the presence of different modes of instabilities that may or may not have effects on sediment removal. To do so, one needs to understand the physical processes that happen below the resolution of most computational models, and to find a way to incorporate them back into the coarser models. In this way, the average physics can be captured even if the model approach is not inherently resolving the phenomena.

For the settling-driven gravitational instabilities, discrepancies exist in expressing the deposition flux between experimental study of Hoyal et al. (1999b) and numerical simulations of Yu et al. (2014) and Burns and Meiburg (2015). Also, in all past work on the topic, flocculation has been suppressed or left out of the analysis picture, even though it could have a profound impact on the settling process. As a result, the scientific community lacks the data to determine whether or not flocculation impacts the development of the instabilities. And no method exists to predict the removal rate of sediment in the presence of such instabilities based on integral quantities in the upper layer.

For the shear instabilities, most work has focused on the transient propagation of the initial head through a stagnant basin (Maxworthy, 1999; Parsons et al., 2001). However, sedimentation from the steady, or near steady, body of the plume is far more significant than

that of the transient head with regard to total delivery of sediment to the coastal region. The only laboratory study that examined the role of shear on the sediment removal rate from the body of a plume is racetrack flume experiments of McCool and Parsons (2004), in which a linear relationship between the non-dimensional turbulent kinetic energy dissipation rate and vertical sediment flux was found. In their experiments, they did not allow sediment to flocculate, and the mechanics of the experiments themselves suggest that additional work should be done to substantiate their findings. Therefore, the mechanism of enhanced flux due to shear is not well understood, and no simple model exist to predict the effective settling velocity in the presence of shear based on the integral flow and sediment characteristics of the plume.

A distinction between leaking and shear-induced settling is whether or not there is turbulence mixing at the interface between the plume and the receiving water body. If there is, then settling-driven Rayleigh-Taylor structures are not expected. However, when mixing is suppressed due to the lack of mean plume advection, an interface layer can form that develops leaking. To our knowledge, no study has defined the transition from settling under the effects of shear instabilities to that under leaking. Since differences exist both in the nature of the two phenomena and in the conditions that lead to dominance of one mechanism over the other, it is of interest to seek to understand where, and under what conditions, these different mechanisms may impact or drive sedimentation.

In Chapter 2, we further investigate the development of downward convecting plumes of sediment arising from gravitational instabilities and their impact on vertical sediment

flux through physical experiments. We wish to expand on previous experimental work by allowing clay-size sediment to flocculate, examining the general behavior under a larger range of sediment concentration, and by measuring the downward velocity of the convecting plumes that develop. We collected the data required for development of a model that wraps up the effects of settling-driven instabilities into a single effective setting velocity, and compared the total vertical sediment flux with the expected individual floc settling flux. Our primary hypothesis is that settling-driven gravitational instabilities control the downward flux of sediment when operating and that the sediment flux can be linked to bulk properties of the upper layer when leaking occurs.

In Chapter 3, we further explore the role of interface shear on the effective settling velocity from freshwater suspensions of mud flowing over clear saltwater, and collect the data required for development of a model that wraps up the effects of the shear instabilities into a single effective setting velocity by measuring the total vertical sediment flux. We hypothesize that shear-induced settling can be significant enough to compete with individual floc settling and that the added flux can be linked to the mixing process at the stratification interface.

In Chapter 4, we make quantitative comparisons between the two mechanisms, to better understand their role in the total removal of sediment over the length of a plume. We make the comparisons in terms of conditions that lead to dominance of one mechanism over the other, and the orders of the magnitude of their influence on the effective settling velocity. The goal of Chapter 4 is to present an analysis that seeks to contextualize the removal rates and zones of operation of these mechanisms over the length of a plume. We suggest that the

shear-induced particle entrainment ceases and the potential for leaking commences, where interfacial entrainment is essentially zero.

1.3 Approaches

To test the hypotheses of Chapters 2 and 3, two sets of experiments are designed in which the effects of settling-driven and shear-driven modes of interface instability are captured and investigated separately. One set of experiments examines interface instabilities and sediment removal from a buoyant, flocculated freshwater suspension overlying saltwater, in a laboratory stagnant stratification tank. In this set of experiments, measurements were made with time of the change in concentration in the upper and lower layers, the floc size, and the downward velocity of the leaks. In the second set of laboratory experiments, sedimentation from buoyant freshwater suspensions of kaolinite clay overlying saltwater is again investigated but, this time, with the addition of mean longitudinal flow of the upper layer. In these experiments, measurements of sediment concentration were made with time of both the entering and exiting flows. In addition, we measured vertical profiles of velocity and salinity through the shear layer along with the distribution of floc sizes in both upper and lower layers. Of significance in the experimental design is that we collect data on the effective settling velocity under steady-state conditions. Achieving steady-state was deemed important for our study since there can be significant differences in the mixing properties of a propagating plume or current head and the steady-state body (MacDonald and Geyer, 2004; Yuan and Horner-Devine, 2013), and because it is the steady or quasi-steady body that delivers the largest volume of sediment during a storm event.

In both sets of experiments, the floc size measurements were used to calculate an average floc settling velocity, and the effective settling velocity of each condition was obtained using a suspended sediment mass conservation box model. In each of Chapters 2 and 3, details regarding the experimental setup, procedures, conditions, and data analysis methods are given following a general introduction to the specific topic of the chapter. Below, a brief overview of how the data is used to test the hypotheses is given.

In Chapter 2, the floc settling velocities and the box model are used to predict the maximum sediment removal rates due to individual floc settling. To test the primary hypothesis, the predictions are compared to the actual removal rates obtained from the experimental measurements of concentration. The effective settling velocity is compared to the floc settling velocity and the downward velocity of the leaks under different initial conditions. Data from the experiment is then combined with theory to develop a model for effective settling velocity, and hence removal rate, based on bulk fluid and sediment properties.

Similarly, in Chapter 3, the hypothesis is tested by comparing the floc settling velocities and the effective settling velocities. Then, visual observations and data are combined with conceptual theory to develop a model for the effective settling.

In Chapter 4, a comparison is made of the magnitudes of the floc settling velocity and the expected settling velocities under the effects of settling-driven and shear-driven interface instabilities over a range of hypothetical river mouth plume conditions that are loosely based on the conditions of Merrimack River (Massachusetts). A simplified buoyant jet model that includes a flocculation model is used to compute the hydraulic characteristics and the floc

sizes within the hypothetical steady-state plume in the crossshore direction. Calculations of the leak and shear-induced settling velocities are made using the semi-empirical relations developed in Chapter 2 and 3 of this study. This comparison is followed by a qualitative discussion on the conditions leading to operation of each of the mechanisms over the length of a plume.

The methods, results, discussion, and conclusion of each aspect of this study are presented separately in Chpaters 2, 3, and 4 as part of each individual paper. In Chapter 5, a summary of conclusions from all aspects of this study are given along with a list of the presentations and publications that resulted from the body of work.

Bibliography

Blanchette, F. and Bush, J. W. M. (2005). Particle concentration evolution and sedimentation-indiced instabilities in a stably stratified environment. *Physics of Fluids*, 17:073302.

Burns, P. and Meiburg, E. (2012). Sediment-laden fresh water above salt water: linear stability analysis. *Journal of Fluid Mechanics*, 691:279–314.

Burns, P. and Meiburg, E. (2015). Sediment-laden fresh water above salt water: nonlinear simulations. *Journal of Fluid Mechanics*, 762:156–195.

Chen, C. F. (1997). Particle flux through sediment fingers. *Deep Sea Research*, 44, No. 9-10:1645–1654.

Chen, S.-N., Geyer, W. R., Sherwood, C. R., and Ralston, D. K. (2010). Sediment transport and deposition on a river-dominated tidal flat: An idealized model study. *Journal of Geophysical Research*, 115(C10040).

Christodoulou, G. C. (1986). Interfacial mixing in stratified flows. *Journal of Hydraulic Research*, 24:77–92.

Dyer, K. R. (1989). Sediment processes in estuaries: future research requirements. *Journal of Geophysical Research*, 94(C10):14327–14339.

Geyer, W. R., Hill, P. S., and Kineke, G. C. (2004). The transport, transformation and dispersal of sediment by buoyant coastal flows. *Continental Shelf Research*, 24(7-8):927 – 949.

Geyer, W. R. and Smith, J. D. (1987). Shear instability in a highly stratified estuary. *Journal of Physical Oceanography*, 17:1668–1679.

Gladstone, C. and Pritchard, D. (2010). Patterns of deposition from experimental turbidity currents with reversing buoyancy. *Sedimentology*, 57:53–84.

Green, T. (1987). The importance of double diffusion to the settling of suspended material. *Sedimentology*, 34:319–331.

Green, T. and Kirk, R. (1971). Descent rates of salt fingers. *Nature (Physical Science)*, 232:123–124.

Harris, C. K., Traykovski, P. A., and Geyer, W. R. (2005). Flood dispersal and deposition by near-bed gravitational sediment flows and oceanographic transport: A numerical modeling study of the Eel River shelf, northern California. *Journal of Geophysical Research*, 110(C09025).

Henniger, R. and Kleiser, L. (2012). Temporal evolution, morphology, and settling of the sediment plume in a model estuary. *Journal of Physics of Fluid*, 24:086601.

Hill, P. S., Milligan, T. G., and Rockwell Geyer, W. (2000). Controls on effective settling velocity of suspended sediment in the Eel River flood plume. *Continental Shelf Research*, 20(16):2095–2111.

Houk, D. and Green, T. (1973). Descent rates of suspension fingers. *Deep Sea Research*, 20:757–761.

Hoyal, D. C. J. D., Bursik, M. I., and Atkinson, J. F. (1999a). The influence of diffusive convection on sedimentation from buoyant plumes. *Marine Geology*, 159(1-4):205 – 220.

Hoyal, D. C. J. D., Bursik, M. I., and Atkinson, J. F. (1999b). Settling-driven convection: A mechanism of sedimentation from stratified fluids. *Journal of Geophysical Research*, 104:7953–7966.

Kineke, G. C., Woolfe, K. J., Kuehl, S. A., Milliman, J. D., Dellapenna, T. M., and Purdon, R. G. (2000). Sediment export from the sepik river, papua new guinea: evidence for a divergent sediment plume. *Continental Shelf Research*, 20:2239–2266.

Krone, R. B. (1963). A study of rheological properties of estuarine sediments. Committee on Tidal Hydraulics Final Report 63-88, Waterways Experiment Station, Corps of Engineers, US Army.

MacDonald, D. G. and Geyer, W. R. (2004). Turbulent energy production and entrainment at a highly stratified estuarine front. *Journal of Geophysical Research*, 109, C05004:doi:10.1029/2003JC002094.

Maxworthy, T. (1999). The dynamics of sedimenting surface gravity currents. *Journal of Fluid Mechanics*, 392(1):27–44.

McCool, W. W. and Parsons, J. D. (2004). Sedimentation from buoyant fine-grained suspensions. *Continental Shelf Research*, 24:1129–1142.

Milliman, J. D. and Syvitski, P. M. (1992). Geomorphic/tectonic control of sediment discharge to the ocean: The importance of small mountainous rivers. *Journal of Geology*, 100:525–544.

Mulder, T. and Syvitski, J. P. M. (1995). Turbidity currents generated at river mouths during exceptional discharges to the world oceans. *Journal of Geology*, 103(3):285–299.

Nowacki, D. J., Horner-Devine, A. R., Nash, J. D., and Jay, D. A. (2012). Rapid sediment removal from the columbia river plume near field. *Continental Shelf Research*, 35:16–28.

Parsons, J. D., Bush, J. W. M., and Syvitski, J. P. M. (2001). Hyperpycnal plume formation from riverine outflows with small sediment concentrations. *Sedimentology*, 48(2):465–478.

Parsons, J. D. and Garcia, M. H. (2000). Enhanced sediment scavenging due to double-diffusive convection. *Journal of Sedimentary Research*, 70(1):47–52.

Partheniades, E. (2009). *Cohesive Sediments in Open Channels*. Butterworth-Heinemann/Elsevier, Burlington, MA.

Spahn, E. Y., Horner-Devine, A. R., Nash, J. D., Jay, D. A., and Kilcher, L. F. (2009). Particle resuspension in the columbia river plume near field. *Journal of Geophysical Research*, 114:C00B14, doi:10.1029/2008JC004986.

Strom, K. and Keyvani, A. (2011). An explicit full-range settling velocity equation for mud flocs. *Journal of Sedimentary Research*, 81:921–934.

Strom, K. and Keyvani, A. (2016). Flocculation in a decaying shear field and its implications for mud removal in near-field river mouth discharges. *Journal of Geophysical Research, Oceans*, 121:doi:10.1002/2015JC011169.

Syvitski, J. P., Skene, K. I., Nicholson, M. K., and Morehead, M. D. (1998). Plume1.1: Deposition of sediment from a fluvial plume. *Computers and Geosciences*, 24:159–171.

Turner, J. (1967). Salt fingers across a density interface. *Deep Sea Research*, 14(5):599 – 611.

Winterwerp, J. C. and van Kesteren, W. G. M. (2004). *Introduction to the physics of cohesive sediment in the marine environment*, volume 56 of *Developments in Sedimentology*. Elsevier, Amsterdam, The Netherlands.

Yu, X., Hsu, T.-J., and Balachandar, S. (2013). Convective instability in sedimentation: linear stability analysis. *Journal of Geophysical Research*, 118:256–272.

Yu, X., Hsu, T.-J., and Balachandar, S. (2014). Convective instability in sedimentation: 3d numerical study. *Journal of Geophysical Research: Oceans*, 119:8141–8161.

Yuan, Y. and Horner-Devine, A. R. (2013). Laboratory investigation of the impact of lateral spreading on buoyancy flux in a river plume. *Journal of Physical Oceanography*, 43:2588–2610.

2 Sedimentation from Flocculated Suspensions in the Presence of Settling-Driven Gravitational Interface Instabilities

2.1 Introduction

Modeling the vertical flux of sediment from river mouth discharges is an integral part of understanding where sediment delivered to the coast eventually deposits to build subaqueous deltas and clinoforms or act as source mud for wave-supported gravity flows. In most forms of modeling, deposition flux is set using a grain-size specific settling velocity multiplied by the local concentration (Geyer et al., 2004; Harris et al., 2005; Chen et al., 2010). However, for buoyant mud plumes lofting over saltwater (hypopycnal river discharges), two additional mechanisms can potentially influence the vertical flux of sediment from the plume to the lower ocean waters. One of these processes is flocculation, which can complicate the estimation of the individual particle settling velocity since floc size and density is a function of the local flow and sediment conditions (Krone, 1963; Dyer, 1989; Winterwerp and van Kesteren, 2004; Partheniades, 2009; Strom and Keyvani, 2011). The other is the potential of gravitational instability formation near the stratification interface and the onset of downward advection of the fluid and sediment mixture in small negatively buoyant plumes (Green, 1987; Geyer and Smith, 1987; Hoyal et al., 1999a,b; Parsons et al., 2001).

Gravitational instabilities can develop in stratified systems that are initially stable due

to differences in substance diffusion rates, particle settling, or mixing. Each of these mechanisms is briefly discussed below, but the general outcome of any of these three mechanisms is the creation of a layer of fluid near the interface that is denser than the fluid below it. At first, resisting forces may keep this layer in place. But, with time, the gravitational forces can overcome the resisting forces and lead to downward advection of the sediment-laden fluid at rates that can exceed the individual particle settling velocity. Such instabilities are classified by their initiation mechanism as being double diffusive (Green, 1987; Chen, 1997; Hoyal et al., 1999a; Parsons and Garcia, 2000), settling (Hoyal et al., 1999b; Blanchette and Bush, 2005), or shear (Geyer and Smith, 1987; Maxworthy, 1999; McCool and Parsons, 2004) driven gravitational instabilities.

Diffusion, settling, and shear mixing can all be active at any given time, but one process often dominates the system behavior (Hoyal et al., 1999a; Parsons et al., 2001; Burns and Meiburg, 2012; Yu et al., 2013, 2014; Burns and Meiburg, 2015). A distinction between these three mechanisms is whether or not there is turbulent mixing at the interface between the hypopycnal river discharge and the receiving water body. If there is, then shear or turbulence is likely the mechanism leading to gravitationally unstable packets of fluid and sediment (Maxworthy, 1999; Parsons et al., 2001; McCool and Parsons, 2004). However, in cases where mixing is suppressed due to lack of mean plume advection, or very strong stratification, gravitationally unstable mixtures of fluid and sediment can develop due either to, or in combination to, the double-diffusive or settling-driven mechanisms. In this paper, we focus on this second category of instability where interface shear is suppressed.

2.1.1 Interface Instabilities In The Absence Of Turbulent Mixing

Double-diffusive instabilities develop due to the different rates at which the substances in the upper and lower layers diffuse across the interface. The classic double-diffusion problem is that of saltwater fingering at a thermocline (e.g., Turner, 1967; Green and Kirk, 1971). In this system, salt diffuses upward into the warm freshwater layer and heat diffuses downward into the saltwater layer. The result of the two-way diffusion is an unstable band of locally more dense fluid near the interface that develops into a regular and symmetric pattern of downward and upward convecting fingers of alternating densities. Double-diffusive fingering can also occur in thermally stratified systems with warm suspensions of sediment overlying cooler clear water (Houk and Green, 1973; Green, 1987; Hoyal et al., 1999a; Parsons et al., 2001). Key in the development of double-diffusive fingering for suspensions of sediment is that the sediment in the buoyant layer settles very slowly so that substance diffusion, and not particle settling, is primarily responsible for changes in the vertical density profiles (Burns and Meiburg, 2012; Yu et al., 2013; Burns and Meiburg, 2015; Yu et al., 2014). Within the band of conditions conducive to double diffusion, transport of sediment within the double-diffusive fingers can be a significant contribution to the total downward sediment flux (Hoyal et al., 1999a).

For the settling-driven mechanism, the band of heightened mixture density is generated by particles settling down across the saltwater interface at a rate that is much faster than the upward diffusion of salt. This produces an unstable band of sediment-laden saltwater, i.e., the so-called interface layer, sitting between the muddy freshwater and the underlying

clear saltwater. This phenomenon has been experimentally observed by Hoyal et al. (1999b), Parsons et al. (2001), and Blanchette and Bush (2005) and examined through linear stability analysis by Burns and Meiburg (2012) and Yu et al. (2013) and Direct Numerical Simulation (DNS) by Yu et al. (2014) and Burns and Meiburg (2015). A few defining characteristics of the settling-driven mechanism are the general creation of the interface layer below the initial stratification contact (Hoyal et al., 1999b), the onset of Rayleigh-Taylor generated plume like structures, asymmetry in the downward and upward interface motions, and the overall larger length scales of the instabilities and instabilities spacing (centimeter scale) compared to the double-diffusive generated fingering (millimeter scale) (Hoyal et al., 1999b; Blanchette and Bush, 2005; Burns and Meiburg, 2012; Yu et al., 2013; Burns and Meiburg, 2015; Yu et al., 2014). Further key observations regarding settling-driven instabilities have been that (1) the thickness of the interface layer at the commencement of downward convection tends to thicken as concentration goes down (Hoyal et al., 1999b), (2) that the spacing between points of downward convection tends to also be inversely related to concentration (Hoyal et al., 1999b; Yu et al., 2013), and (3) that the diameters of the instabilities may increase with concentration or sediment settling velocity (Yu et al., 2013).

The level of influence, and resulting vertical instability characteristics, of double-diffusive versus the settling-driven mechanism has been a topic of primary interest in both experimental and theoretical work. The basic questions examined revolve around the types of boundary conditions that lead to dominance of one mechanism over the other, and how the different instabilities dictate the mechanics of the system. These questions are pertinent

to our study as well. We briefly review here some of the main findings thus far.

In a series of two different experiments, Hoyal et al. (1999b) and Hoyal et al. (1999a) clearly showed both the double diffusive and settling driven modes can develop in sediment suspensions. In the body of work, Hoyal et al. presented a theoretical argument based on flux calculations as to when one mode would dominate over the other. They concluded that for freshwater sediment plumes, thermal stratification is likely needed if double-diffusive instabilities are to dominate the interface. This conclusion would likely restrict the double diffusive mechanism to lake environments. When salt is the primary stratifying agent (coastal environments), they suggested that it is far more likely that settling-driven instabilities will dominate.

Parsons et al. (2001) further investigated the instability mechanism question for a warm, sediment-laden freshwater plume overlying cooler ambient saltwater. The primary outcome of the study was a phase diagram depicting the dominate instability mode as a function of a thermal stabilizing ratio and sediment concentration. Parsons et al. (2001) similarly concluded that thermal stratification and high sediment concentrations are likely needed for double diffusion to dominate. In addition, they identified an instability that is different than classic double-diffusive fingering. They referred to these persistent, downward flowing plumes or corridors of fluid and sediment as leaks. These leaks were thought to be similar to the settling-driven instabilities of Hoyal et al. (1999b) and to form at low sediment concentrations in the absence of thermal stratification.

More recently, the studies of Burns and Meiburg (2012, 2015) and Yu et al. (2013,

2014) have been particularly helpful in understanding key differences in initial conditions that will lead to the onset of double-diffusive or settling-driven Rayleigh-Taylor or leaking instabilities in coastal settings. Both research groups used linear stability analysis to examine the first order instability growth rates under a spectrum of initial conditions. They then extended their analyses with fully-nonlinear 2 and 3D DNS that allow for detailed probing of the interface velocities, concentrations, and fluxes. The initial studies of Burns and Meiburg (2012) and Yu et al. (2013) both suggested that when the Stokes diameter of the sediment in the freshwater layer is greater than approximately 10 μm, it is likely that settling-driven convection will dominate at isothermal conditions under salt induced stratification. The 3D simulations of Yu et al. (2014) for three different particles sizes (2, 4, and 20 μm) under a range of concentrations (4-32 g/l) confirmed and further teased out the conditions that will lead to different instability modes by showing that for unflocculated clay (d=2-4 μm) salt stratification at isothermal conditions should lead to double-diffusive dominated instabilities. However, as sediment size shifts up into the silt range (d=20 μm), the dominant mode shifts toward settling driven leaking. In their simulations, the difference in mode and instability morphology is clearly visible. Rather than using raw sediment size, Burns and Meiburg (2015) showed that the dominate instability mode could be related to a key interface thickness ratio, H/l_s, where H is the thickness of the downward expanding sediment interface region and l_s is the diffusive interface thickness of the salinity profile. For small values, $H/l_s <$O(0.1), the interface develops double-diffusive fingering, while for larger values, $H/l_s >$O(0.1), Rayleigh-Taylor processes dominate. Moreover, Burns and Meiburg

(2015) shows the thickness ratio is linearly related to a group of nondimensional variables, $V_P R_s Sc^{0.5}$, which is a nondimensional ratio of the inward and outward sediment fluxes into the interface region; V_P is the nondimensional particle settling velocity, Sc is the Schmidt number, and R_s is the stability ratio.

When observing such interface instabilities, one is forced to consider whether or not these instabilities significantly impact the removal rate of sediment from a plume. Based on a box-model of concentration in the upper and lower layers, Hoyal et al. (1999b) concluded that simply expressing the deposition flux as a product of local concentration and Stokes settling velocity was sufficient to describe the time evolution of concentration in the upper and lower layers. From this it would seem that the instabilities work to create well-mixed condition in the lower layer, but that they do not greatly impact calculation of sediment removal from the upper layer. However, Burns and Meiburg (2015) and Yu et al. (2014) both show that settling-driven Rayleigh-Taylor instabilities or leaks can produce substantial downward flux of sediment. Defining an effective settling velocity of the mixture as being equal to the spatially averaged advective flux from the instabilities divided by the average concentration, Yu et al. (2014) showed that instability driven effective settling velocities is a function suspended sediment concentration and that it can reach values on the order of centimeters per second for silt size sediment (d=20μm) when concentrations are on the order of 20 g/l. Effective settling velocities for d=20 μm sediment on the order of centimeters per second is much higher than its 0.36 mm/s Stokes velocity. Additionally, effective settling velocities for mud mixtures (unflocculated clay with Stokes diameters of 4 μm of 10 to 30

g/l was found to reach up into the millimeter per second range.

2.1.2 Study Objectives

The aim of our study is to further investigate the development of downward convecting plumes of sediment arising from gravitational instabilities and their impact on vertical sediment flux through physical experiments. We wish to expand on previous experimental work by examining stratification due to salt, allowing clay-size sediment to flocculate, examining the general behavior under a larger range of sediment concentration, and by measuring the downward velocity of the convecting plumes that develop. The data generated from the experiments will then be used to investigate the following three questions. (1) Do flocs hinder or alter the nature of the interface instabilities? (2) Is the downward flux of sediment due to interface instabilities significant enough to compete with flocculation enhanced individual particle settling when the two processes are simultaneously occurring? And, (3) can effective settling velocity be modeled in a simple way based on bulk fluid and sediment properties in the upper layer? Our primary hypothesis is that gravitational instabilities control the downward flux of sediment.

2.2 Methods

Our experiments were conducted in a laboratory tank starting with an initial sharp stratification interface between a buoyant flocculated kaolinite suspension and clear saltwater. In the experiments, measurements were made with time of the change in concentration, C, in the upper and lower layers, the floc size, d_f, and the downward velocity of the convecting

plumes, V_f. The floc size measurements are then used to calculate floc settling velocities, $W_{s,f}$, and these velocities are used, along with a mass conservation box model, to predict the maximum sediment removal rates due to individual floc settling. To test the primary hypothesis, the predictions are compared to the actual removal rates obtained from the experimental measurements of C. The box model and time series data for C are also used to back calculate an effective settling velocity, $W_{s,eff}$, and this is compared to the floc settling velocity and the downward velocity of the individual plumes under different initial conditions. Data from the experiment is combined with theory to develop a model for effective settling velocity, and hence removal rate, based on bulk fluid and sediment properties.

2.2.1 Experimental Setup

The stratification tank was equipped with two sliding barriers to facilitate the creation of a sharp interface between the upper and lower layers at the beginning of each run. The top section of the tank was 30 cm deep and had a cross section of 30×15 cm^2; the bottom section was 40 cm deep and had cross sectional dimensions of 30×30 cm^2 (Figure 2.1a). The tank dimensions were designed to allow for placement and operation of the instrumentation and to allow for enough space for multiple instabilities to form across the stratification interface. Measurement of sediment concentration was carried out at two elevations in the tank using a pair of OBS 3+ sensors. Both sensors were calibrated with mixtures of the flocculated kaolinite used in the experiment, and were place to sample along the centerline of the tank. One sampled near the bottom of the lower layer (10 cm above the bottom of the tank). The other was positioned in the upper layer to sample at the interface. A digital camcorder

was placed outside the tank to monitor the overall development and velocity of the interface instabilities. Lighting for the video was provided by a laser sheet passing through the center of the tank (Figure 2.1a).

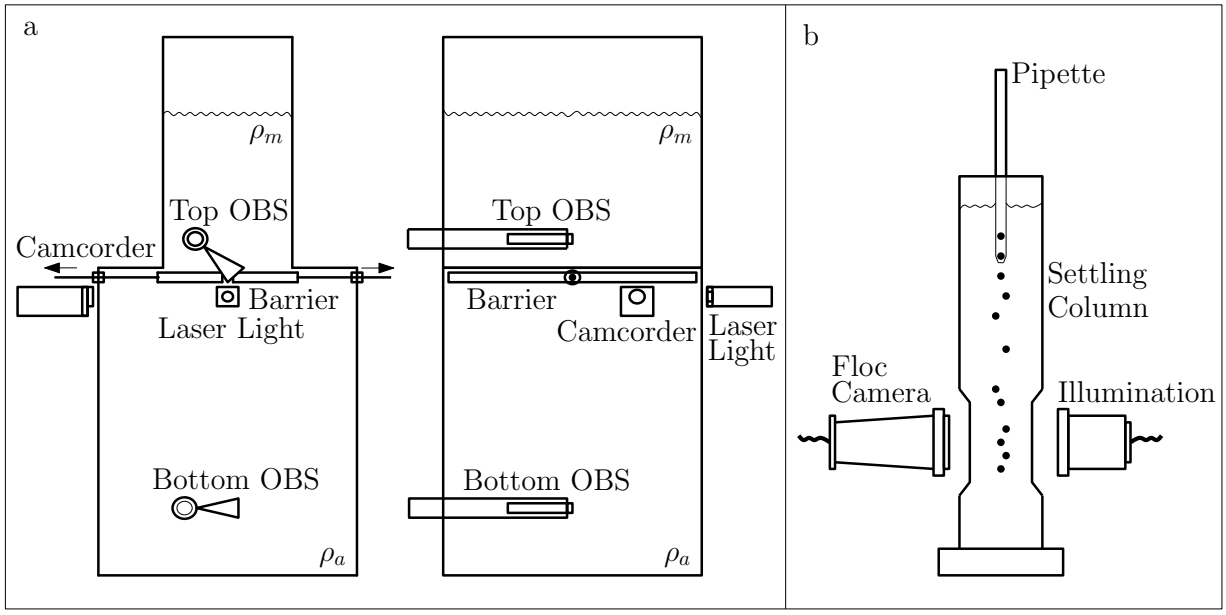

Figure 2.1: a) Front and side view of laboratory tank, and position of experimental equipment b) Floc camera system setup

During the experiments, physical samples of the flocculated suspension were gently extracted from the interface using an eight-millimeter inner diameter modified pipette. Similar methods of floc sampling have been used by Gratiot and Manning (2004); Manning et al. (2007); Mietta et al. (2009); Manning and Schoellhamer (2013). The pipette was then fixed to the top of a settling column, and a floc camera system was used to image the flocs as they settled out of the pipet (Figure 2.1b). Images were collected at a frequency of 1 Hz. In one low-concentration experiment, flocs were measured within the stratification tank instead of removing the flocs with the pipette. However, this method did not work for the higher

concentration experiments due to low lighting and overlapping flocs. The floc camera is a 1392-1040 pixel AVT Firewire progressive scan monochrome camera with a 2x objective magnification lens (Kumar et al., 2010). Floc sizes were measured using the image processing routines of Keyvani and Strom (2013).

2.2.2 Experiment Conditions and Procedures

For each experiment, a 10 liter sample of pure kaolinite clay with a disaggregated d_{50} of 5.7 μm was first prepared. To do this, kaolinite clay was introduced to 200 ml of tap water and sonified for 15 minutes. The sonified mixture was then introduced to a small mixing chamber filled with 10 liters of tap water that had been left to sit for 24 hours to ensure that the water was at room temperature. The suspension was then stirred for one hour in a rotating-paddle chamber to generate a flocculated suspension. During mixing, rhodamine dye was added to the mixing chamber to provide better contrast in the experiment between the upper and lower layers when illuminated with the laser.

The lower layer fluid was prepared by adding salt to 36 liters of tap water that had been sitting at room temperature for 24 hours. The salinity of the mixture was set by adding specific amounts of salt by mass to the water while mixing. Following this, the salinity was checked with an Atago salt meter to ensure that the desired salinity had been reached. The lower region of the tank was then filled with the saltwater up to the sliding barriers (Figure 2.1a). The barriers where then closed and 8 liters of the floc suspension was very gently placed in the upper section of the tank using a siphon.

Each run commenced by opening the stratification barriers. Opening the barriers

Table 2.1: Summary of stratification tank experimental conditions and raw results of 11 runs

Run	C_o	S	$\beta^{'}C_o$	R_s	$W_{s,f}$	V_f	$W_{s,eff,ex}$	F_{ex}	F_{dd}	f	$V_P R_s Sc^{0.5}$	α	λ	$W_{s,fb}$
-	mg/l	ppt	-	-	mm/s	mm/s	mm/s	$mg/s.m^2$	$mg/s.m^2$	-	or H/l_s	-	-	mm/s
1	370	5.5	0.000231	18.27	0.096	0.83	0.044	16.3	2.8	0.17	9.11	0.053	2.8	-
2	390	10.0	0.000243	31.35	0.161	0.84	0.048	18.7	3.0	0.16	15.36	0.057	2.7	-
3	400	15.0	0.000249	45.73	0.447	0.74	0.044	17.6	3.2	0.18	22.22	0.059	2.6	0.15
4	850	5.0	0.000530	7.24	0.288	1.10	0.070	55.3	8.6	0.16	2.73	0.059	2.6	0.18
5	800	10.0	0.000499	15.28	0.624	1.34	0.065	52.0	7.9	0.15	5.89	0.049	3.0	0.18
6	1400	5.5	0.000873	4.83	0.404	2.30	0.20	280	16.8	0.06	1.55	0.087	2.0	0.20
7	1300	15.0	0.000810	14.07	0.143	2.87	0.35	455	15.2	0.03	4.62	0.122	1.5	-
8	2400	5.5	0.001496	2.82	0.191	3.79	0.60	1440	34.4	0.02	0.75	0.158	1.2	0.17
9	2400	10.5	0.001496	5.35	0.159	3.49	0.60	1440	34.4	0.02	1.43	0.172	1.1	0.15
10	2800	5.0	0.001745	2.20	0.348	4.80	0.65	1820	42.2	0.02	0.56	0.138	1.4	0.17
11	2800	9.0	0.001745	3.93	0.413	4.05	0.65	1820	42.2	0.02	1.00	0.160	1.2	0.10

produced very mild long-wavelength sloshing, but this disturbance damped in less than 1 minute to produce a sharp contact between the upper and lower layers. Similar to Parsons et al. (2001), we found the time it took for this wave to damp out to be small relative to the time it took for interface instabilities to form. Throughout the experiment, OBS readings and video were collected along with multiple pipette samples taken from the vicinity of the interface for floc characterization. A summary of the experimental conditions for the 11 runs are presented in Table 2.1. We consider runs 1-3 to be low initial concentration, C_o, runs, 4-7 as moderate C_o, and 8-11 as high C_o experiments. It should be noted that the system was initially stably stratified based on bulk properties in all experiments. The stability ratio, R_s, is used to quantify this, $R_s = (\rho_a - \rho_{fw})/(\rho_m - \rho_{fw})$ where, ρ_m is the mixture density, ρ_a is the salt-water density, and ρ_{fw} is the freshwater density. R_s >1 therefore indicates a stably stratified system (Table 2.1). The top layer mixture densities are calculated as $\rho_m = \rho_{fw}(1+\beta^{'}C_o)$, where $\beta^{'}$ is the volumetric expansion coefficient defined as $\beta^{'} = \delta\rho/\rho\delta C$, and C_o is the initial sediment concentration expressed in units of mass/mass.

2.3 Results: Observations and Data

2.3.1 General Behavior

Once a sharp and stationary interface developed, sediment from the upper layer began slowly settling across the initial fresh to saltwater interface, thereby creating a region of saltwater containing suspended sediment (Figure 2.2). This band of sediment-enriched saltwater is referred to as the interface layer (Hoyal et al., 1999b). Bulk density calculations indicate that the interface layer was heavier than the underlying clear saltwater once initiated; though the layer did not immediately begin to descend as a gravity current. Instead, the interface thickened with time as sediment continued to settle toward the floor of the tank. After a few minutes of growth, the bottom of the interface layer developed surface instabilities that began to descend as small sediment gravity currents. The time lag between the start of the experiment and the first occurrence of descending plumes varied among experiments and was strongly correlated with C_o and the overall interface thickness. Lower concentrations resulted in thicker interface layers and longer times to incipient plume descent (ranged from less than 5 minutes at high concentrations up to 10 minutes for lower concentrations).

Once the first one to two plumes began to descend, the interface layer ceased to thicken and a distinct leaking or descending-plume phase of the experiments commenced. Initial leaks tended to be rather narrow and to develop the well-known anchor shape at their head as they descended (Figure 2.3). Rather than breaking away and detaching from the interface as distinct packets of fluid and sediment, unstable locations tended to persist and to open up corridors for the interface fluid and sediment mixture to descend. Following inception,

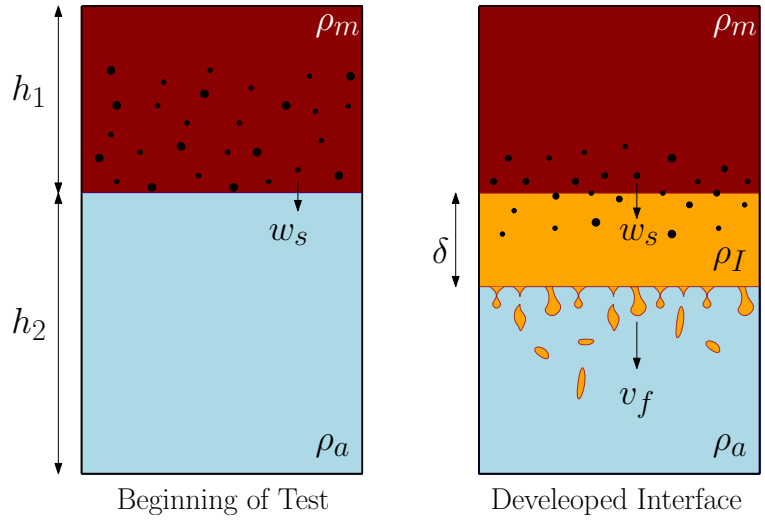

Figure 2.2: Schematic of interface processes in stratification tank experiments

the number of leaks present over the bottom of the interface increased with time. In most cases, during the period of strong leaking, the interaction between descending plumes was significant. Interacting plumes led to changes in descent paths and coalescence of plumes to form larger clouds of particles. During the state of strong leaking, concentration in the upper layer dropped at its fastest rate. This phase continued until the sediment source diminished. We refer to the downward flowing of fluid and sediment as a result of settling-driven instability growth in a general way as leaks (Parsons et al., 2001) or as descending plumes. This is done to be consistent with the literature in distinguishing the process from double-diffusive driven fingering (which we did not see). While we retain this shorthand terminology throughout the paper, it should be noted that our understanding of the Parsons et al. (2001) definition of leaking seemed to be most appropriate for our low-concentration experiments. At higher concentrations, the interfaced instabilities seem to us to look more like a combination of persistent leaks and classic break-away Rayleigh-Taylor instabilities.

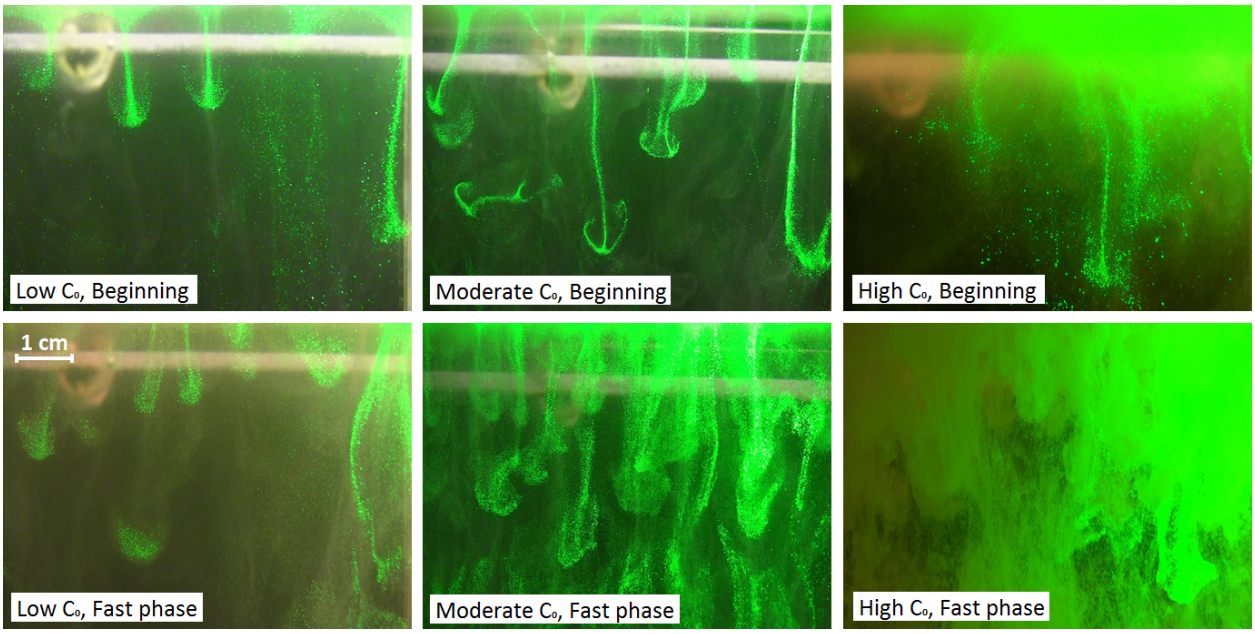

Figure 2.3: Sample images from development and movement of leaks at the interface from different runs with different initial concentrations

Visually, our general observation was that descending plumes tended to thicken with increases in concentration (Figure 2.3). However, a range of plume thicknesses of approximately 0.2 cm at the narrowest up to 1 cm at the thickest was observed in almost all experiments. C_o did have a consistent influence on the time to incipient leaking and on the number of plumes present during the leaking phase. Increases in C_o resulted in faster times to leaking and an overall higher number of plumes (Figure 2.3). The increase in plume number, and the slight increase in plume size, with C_o resulted in a much higher fraction of the bottom plane of the interface layer experiencing active leaking for high C_o runs compared to lower C_o runs.

A summary of the primary experimental data from the 11 runs is presented in Figure 2.4. The top layer time series for C show that there is a lag in time from the start of the

experiment to the point where any decrease in C is observed at the sampling location. At first, one might expect that this delay represents the time to leaking. However, the delay is significantly longer, in most cases, than the lag between the start of the experiments and leak inception. The time to leak inception is denoted on each plot by the first dashed line. The second dashed line, from left to right, denotes the start of strong leaking and rapid decay in C.

In general, floc sizes increased throughout the experiments. Measurement of floc size was difficult and resulted in spot measurements rather than true time series data. Floc sizes ranged up to 150 μm with an average floc size of approximately 80 μm. In general, floc size increased during the experiments up to the point of rapid reduction in concentration and the size seemed to be a function of both concentration and time with larger time lags before rapid removal and larger initial concentrations leading to larger flocs. Differences in floc sizes between experiments could also be due to different mixing conditions experienced during preparation of the initial freshwater and sediment mixture. Higher paddle speeds were needed for the high concentrations to keep all particles in suspension, and it is well known that higher mixing conditions produce smaller flocs (Tambo and Hozumi, 1979).

Of note in these experiments is the observation that salinity did not significantly increase in the bottom few centimeters of the freshwater layer even during the strong leaking phase. This seems to indicate that the salt diffusion front was much smaller than that of the downward propagating sediment front, and that convection in the interface layer did not result in saltwater being transported up into the freshwater layer. This is consistent with

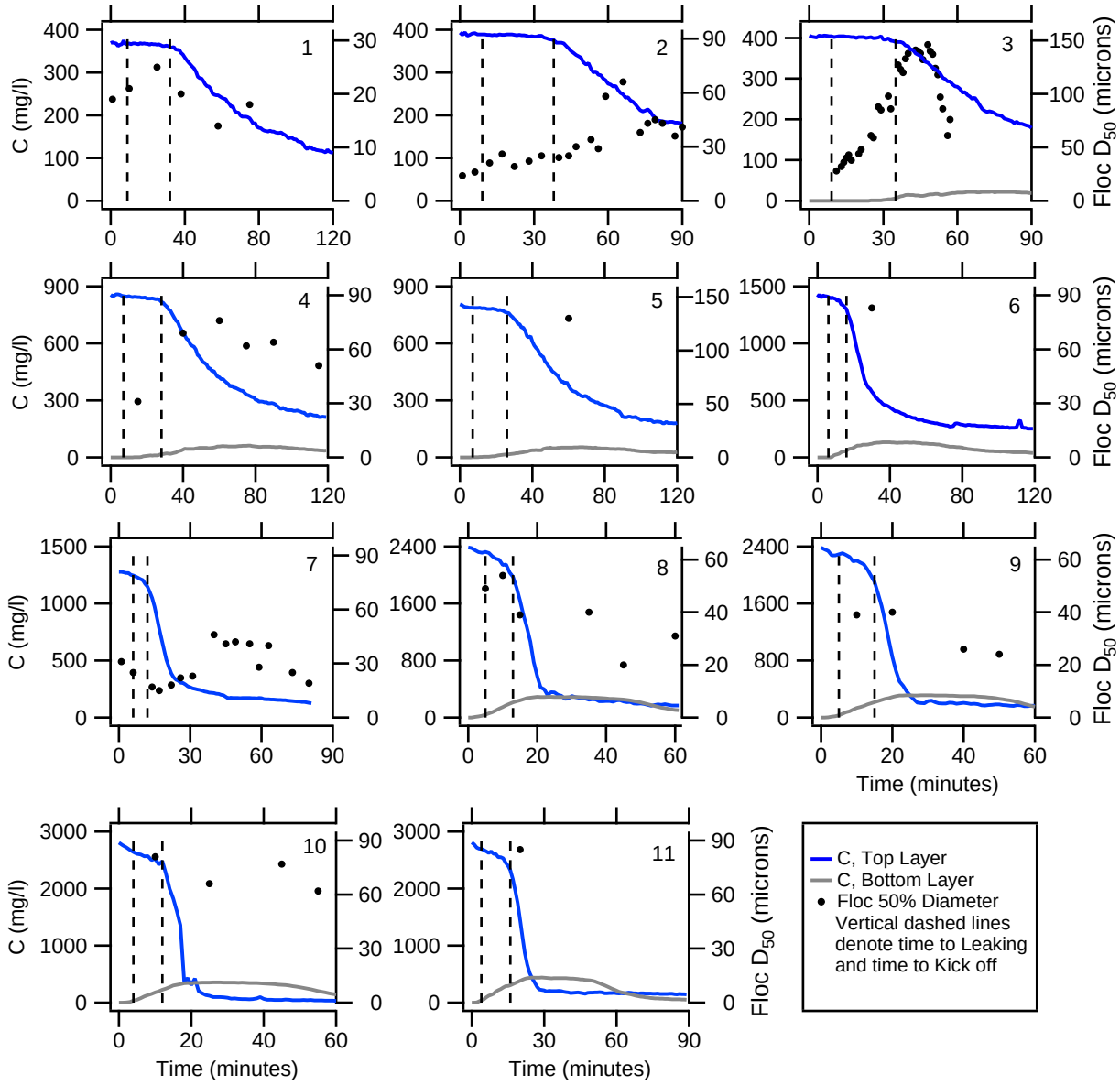

Figure 2.4: Concentration time series and floc size data from 11 runs of stratification tank experiment

the findings of Burns and Meiburg (2015) who show that in the Rayleigh-Taylor instability regime, the salt stratification interface acts as lid to the overturning instabilities below.

2.3.2 Floc, Leak, and Effective Velocity

Data from the experiments allows for calculation and comparison of three different process rates related to vertical movement of sediment. These three process rates are the individual particle and floc settling velocity, the leak velocity, and the effective settling velocity.

Both the primary particle and floc settling velocities were calculated using particle size data and settling velocity equations. For the primary particles, the d_{50} of the sonified particle distribution was used along with Stokes settling velocity equation. Since the primary particles were the same in each experiment, a single Stokes settling velocity of $W_{s,p} = 0.029$ mm/s was used for all experiments. For the flocs, the size data from the image analysis routines was used along with the settling velocity equation Strom and Keyvani (2011):

$$W_{s,f} = \frac{g R_s {d_f}^{n_f-1}}{b_1 \nu {d_p}^{n_f-3} + b_2 \sqrt{g R_s {d_f}^{n_f} {d_p}^{n_f-3}}} \tag{2.1}$$

In equation (2.1), $W_{s,f}$ is the floc settling velocity, g is the gravitational acceleration, R_s is the submerged specific gravity of the particles, d_f and d_p are the floc diameter and the primary particle size respectively, n_f is the floc fractal dimension, ν is the water kinematic viscosity, and b_1 and b_2 are shape dependent parameters. Based on other flocculation experiments with the same sediment and water mixture (Kumar et al., 2010; Strom and Keyvani, 2011), a fractal dimension of n_f=2 along with shape coefficients of b_1=18 and b_2=0.548 where used.

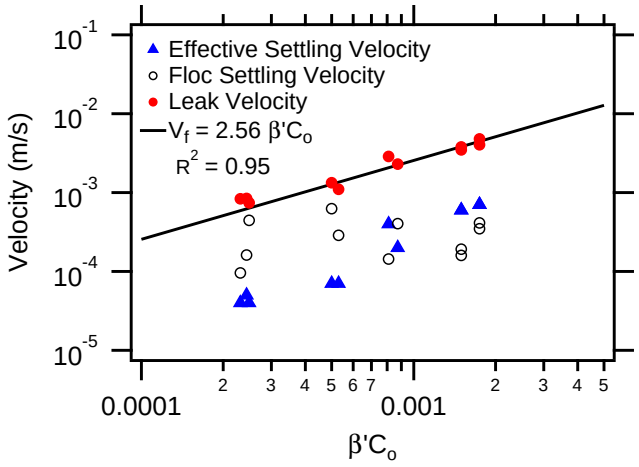

Figure 2.5: Averaged floc settling velocities, fitted effective settling velocities, and averaged settling driven convective plume descent rates of 11 runs of stratification tank experiment, linear relationship between leak descent rates and initial concentrations at the top layer

The averaged floc settling velocities from different runs of the experiment are presented in Figure 2.5 and Table 2.1.

Images of the interface and descending plumes were extracted from the digital video at 0.5 second intervals to measure the plume descent rates. Descent rate was determined by measuring the vertical location of the descending plume head in each image and dividing this by the time between the images. Individual plume descent rates were generated by averaging the measured velocity of a single plume over 5 image frames (2.5 seconds of time in total). Several plumes for each experimental condition were then averaged together to produce a single, average plume descent rate for each set of boundary conditions, V_f (Table 2.1).

The third velocity extracted from the data is what we have termed the effective settling velocity, $W_{s,eff}$. The effective settling velocity is defined in this study as the settling velocity needed to produce agreement between a simple time-dependent box model for C and the OBS measurements collected from the bottom of the upper layer during the fast removal

phase. The box model is based on the conservation of sediment mass and the assumptions that no mass is sourced to the upper layer, that the upper layer is well mixed (which visually appeared to be a reasonable assumption), and that mass is lost through the bottom plane at a rate of $\rho W_s C A$, where W_s is a generic settling velocity and A is the cross-sectional area of the upper portion of the tank. Under these assumptions, the governing equation for C simplifies to:

$$\frac{d(Ch_1A)}{dt} = -W_s C A \tag{2.2}$$

or,

$$C(t) = C_o \exp\left(-W_s t/h_1\right) \tag{2.3}$$

where, C_o is the initial concentration, h_1 is the depth of the layer, and t denotes time. The effective settling velocity was found by allowing W_s in equation (2.3) to be a regression parameter when fitting equation (2.3) to the experimental data during the period of initial quick decay in C (Figure 2.4). The value of W_s that produced the best fit between equation (2.3) and the data was defined as $W_{s,\mathit{eff},ex}$. It should be noted that our definition of $W_{s,\mathit{eff},ex}$ differs from that of Yu et al. (2014) and Burns and Meiburg (2015) who both use the spatially-averaged instability advective flux $\langle W^{'}C^{'}\rangle$, where $W^{'}$ is the local vertical velocity fluctuation and $C^{'}$ is the local concentration fluctuation calculated from the DNS runs, to define the effective settling velocity as $W_{s,\mathit{eff}} = -\langle W^{'}C^{'}\rangle/\langle C\rangle$. In our case, we opt for the box model definition because we do not have a way to reliably measure $\langle W^{'}C^{'}\rangle$ in the laboratory.

Averaged floc settling velocities, plume descent velocities, and effective settling veloci-

ties are given in Table 2.1 and plotted in Figure 2.5 as a function of fractional excess density. A few observations can be made regarding the three different velocities. First, the descent speed of the plumes is higher than both the floc settling velocity and the effective settling velocity. Second, the effective settling velocity and the floc settling velocity are similar in magnitude. Third, the floc settling velocity is relatively uncorrelated with the fractional excess density, whereas both the plume velocity and effective velocity appear to be proportional to $\beta' C_o$; regression gives V_f=2.56$\beta' C_o$ with R^2=0.95 (Figure 2.5).

2.4 Results: Removal Rates

2.4.1 What Process Dominates Removal?

Three processes that could impact the vertical removal rate of sediment from the upper layer are: double diffusive flux, individual particle settling, and settling driven convection. The question of which process is most responsible for the observed decrease in C is discussed here by looking at the initial conditions of our study in light of past work and by comparing the predicted and observed flux values associated with the different processes.

Based on the average floc settling velocities ($W_{s,f}$=0.1 to 0.6 mm/s $\Rightarrow$ a Stokes diameter of 10 to 30 μm) and the fact that the tank was at isothermal conditions, it is likely that the observed convection was not driven by double diffusion (Hoyal et al., 1999a,b; Parsons et al., 2001; Burns and Meiburg, 2012; Yu et al., 2013, 2014; Burns and Meiburg, 2015). For example, use of the Parsons et al. (2001) interface instability phase diagram would lead to a classification of our experiments as leaking due to the absence of a temperature gradient and our relatively low sediment concentrations (C <4 g/l). Moreover, estimation of the

Burns and Meiburg (2015) interface thickness ratio H/l_s indicates that H/l_s is greater than 0.1 for all of our experiments (Table 2.1). According to Burns and Meiburg (2015), H/l_s values greater than 0.1 result in Rayleigh-Taylor type instabilities. H/l_s was calculated for our experiments from the $H/l_s = V_P R_s Sc^{0.5}$ relation of Burns and Meiburg (2015) using our experimental conditions to calculate R_s, $V_P = W_{s,p}/(\nu g \beta' C)^{1/3}$, and $Sc = \nu/D_s$ where, D_s is the diffusion coefficient of salt.

Estimates of the theoretical double-diffusive flux can be made using the model of Schmitt (1979) as modified by Green (1987). The model gives the maximum downward flux at an initial sharp interface as:

$$F_{dd} = 0.05\rho\Big(gD\beta'\Big)^{1/3}(C_o)^{4/3} \tag{2.4}$$

where, D is the diffusion coefficient of the fastest diffusing substance. Assuming that salt is the faster diffusing substance and taking the salt diffusivity as 1.611×10^{-9} m^2/s, the theoretical double-diffusive fluxes, F_{dd}, can be calculated for each experiment. The ratio of the F_{dd} to the observed flux, $F_{ex} = \rho W_{s,eff} C_o$ are presented in Table 2.1 ($f = F_{dd}/F_{ex}$). A value of f <1 in all cases supports the initial assumption that double diffusion is likely not the mechanism primarily responsible for the observed decay in C.

The ability of individual particle settling to explain the concentration time series was examined using the Stokes velocity of the primary particles and the settling velocity of the flocs in equation (2.3). Figure 2.6 shows the predicted $C = C(t)$ trends for both of these settling velocities along with the observed data and back-calculated $W_{s,eff,ex}$ trends.

Removal due to Stokes settling is presented here for reference purposes only. In all cases, Stokes settling of primary clay particles greatly under predicts the sediment removal rate. This is to be expected since the majority of the particles in the upper layer were flocculated. Additionally, the disparity between the predicted $C = C(t)$ with $W_{s,p}$ and the observed data increases with increases in C_o (Figure 2.6 runs 1 and 11). Predictions using the floc settling velocity are much closer to the observed trends. However, there is a systematic deviation between the observations and floc settling flux predictions in that floc settling over estimates the observed removal rate at low initial concentrations and under estimates the observations at high concentrations (Figure 2.6). This trend can also be seen in Figure 2.5 with the near independence of $W_{s,f}$ with $\beta^{'} C_o$.

2.4.2 Effective Settling Velocity Model

The predictions of $C = C(t)$ using either the primary particle or floc settling velocity cannot fully explain the functionality of the observations. This conclusion, combined with the observations of strong convection in the experiments and the apparent correlation between $W_{s,eff}$ and V_f (Figure 2.5) supports the primary study hypothesis that settling instabilities at the interface influence the flux of sediment from the top to bottom layers. The analysis below is devoted to developing a simple model based on initial upper layer concentration to estimate removal fluxes under the influence of settling driven convection.

A model for downward flux due to leaking must include the velocity of the descending plumes, V_f, the overall fractional plume cross-sectional area, A_f, and C. To scale the descent rate of plumes, an analysis similar to the double-diffusion finger velocity model of Green and

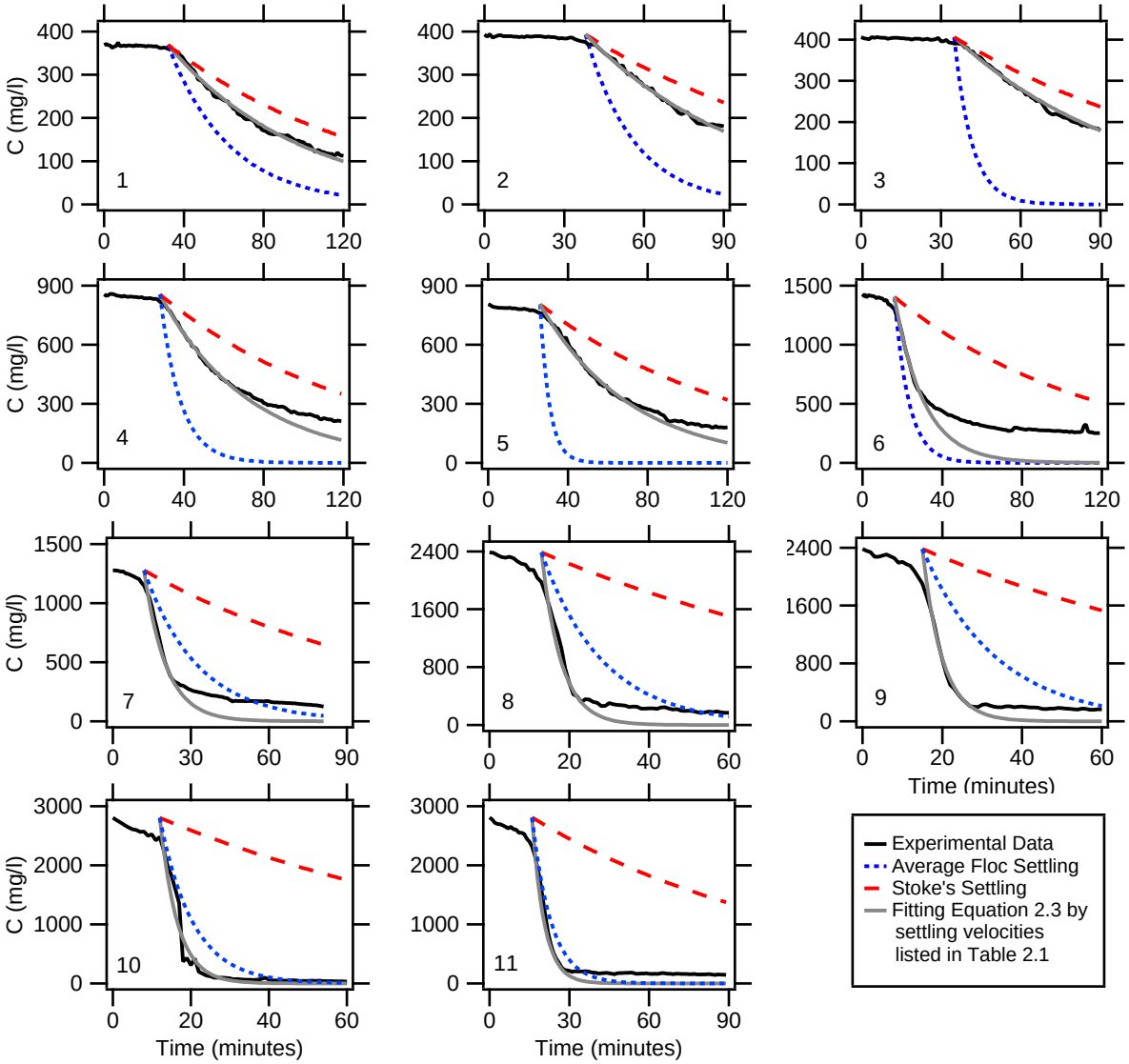

Figure 2.6: Comparison of one-layer system individual particle settling process predictions to stratification tank experimental data

Kirk (1971) is used. Using their model is reasonable since Houk and Green (1973) found that salt and sediment fingers are analogous in many ways; especially, when the driving force is gravity. In Green and Kirk (1971), salt fingers are treated as solid cylinders that descend under their own weight and are opposed by buoyancy and viscous shear. The force balance on the descending plume leads to linear dependence of the descent rate on C in the overlying layer (Green, 1987; Parsons et al., 2001).

$$\frac{\pi r^2}{4} h \rho_I g - \frac{\pi r^2}{4} h \rho_a g = 2\pi r h \rho_a \nu_a \frac{V_f}{r} \tag{2.5}$$

where, ν_a is the kinematic viscosity of ambient fluid (saltwater solution), r is the plume diameter, h is the plume height, ρ_a is the density of ambient fluid and ρ_I is the density of the interface region. Taking the plume thickness, r, as a constant leads to:

$$V_f = \frac{r^2 g}{8\nu_a} \left(\frac{\rho_I - \rho_a}{\rho_a} \right) = K \left(\frac{\rho_I - \rho_a}{\rho_a} \right) \tag{2.6}$$

where, K is a constant coefficient. Treating plume thickness as a constant is the most crucial assumption in the proposed model since a spectrum of sizes was observed in the experiments. Additionally, plume thickness likely depends, at least to some extent, on the initial concentration and settling velocity (Hoyal et al., 1999b; Yu et al., 2013). Nevertheless, we use a constant plume thickness in the formulation that follows as a first approximation.

Assuming that the concentration in the interface layer is equal to that in the lower regions of top layer (where the OBS measurements are made), the interface density can

be calculated as $\rho_I = \rho_a(1 + \beta C_o)$. Plugging ρ_I into equation (2.6) leads to the linear relationship between plume descent rate and the initial concentration (Green, 1987; Parsons et al., 2001):

$$V_f = K\beta' C_o \tag{2.7}$$

This theoretical linear relation between V_f and $\beta' C_o$ was also observed in the experimental data with K=2.56 (Figure 2.5). Even though the convective descending plumes in our experiments are initiated by settling instead of double diffusion, the relationship between V_f and $\beta' C_o$ is the same as that of Green (1987) (Figure 2.7). This behavior confirms that the downward plume velocity is due to the bulk change in fluid density generated by sediment in the interface layer. The finger descent rates from the Parsons et al. (2001) experiments are also included in Figure 2.7. In general, their measured velocities are slower than those from Green (1987) and our study. Parsons et al. (2001) suggests that the slower speeds are likely due to increase mixing of the buoyant layer with ambient fluids once it is released from the lock-exchange box; resulting in less density contrast that the point of fingering than the initial inlet concentration would predict. Nevertheless, the linear relationship of V_f and $\beta' C_o$ of the source layer can still be observed.

To define a flux due to transport of particles within the descending plumes, the total cross-sectional area experiencing leaking needs to be defined. During the experiments it was visually observed that the total active cross-sectional area increased with C (Figure 2.3). Hoyal et al. (1999b) proposed that both spacing and diameter of instabilities should be proportional to the thickness of the interface layer, δ. In our case this would mean that

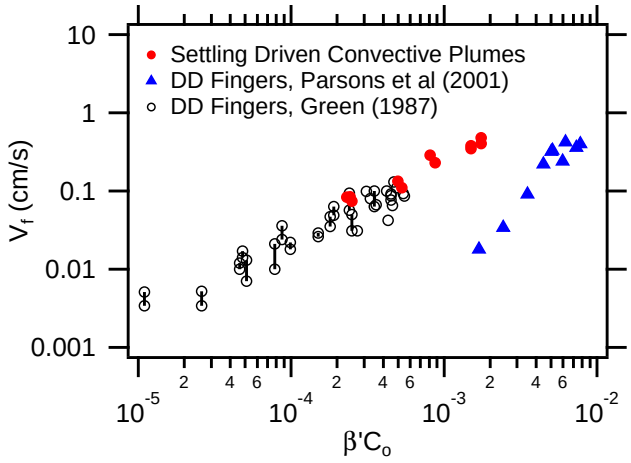

Figure 2.7: Comparison of convective plume (leak) descent rates from this study with finger velocities from Green (1987) and Parsons et al. (2001)

as C_o goes up and the interface layer thins, both the spacing and diameter of the descending plumes should also go down. This would result in thin and tightly packed plumes at high concentrations and thick ones with larger spacing at low concentrations. In our experiments it was difficult to see any systematic change in the plume thickness. If anything, plumes tended to thicken as concentration went up. However, we did observed a systematic decrease in the spacing between instabilities with increased C_o or decreased δ similar to Hoyal et al. (1999b).

Hoyal et al. (1999b) proposed that the onset of leaking was analogous to thermal plume formation at a heated flat plate, and that a critical condition for the onset of leaking could be defined using a critical Grashof number of 1000. Here, we adopt the same approach and critical Grashof number, Gr,

$$Gr = \frac{g^{'}\delta^3}{\nu^2} = 1000 \tag{2.8}$$

where, δ is the characteristic length scale of the process and $g^{'}$ is the reduced gravity defined

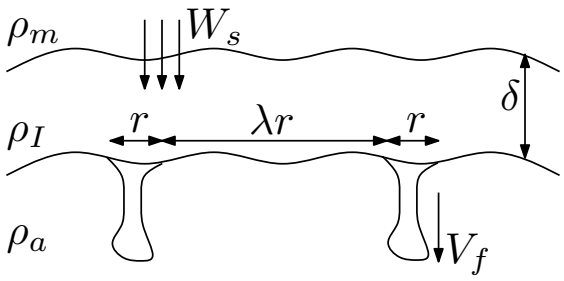

Figure 2.8: Presentation of non-dimensional instability (leak) spacing parameter

as $g^{'} = g\Delta\rho/\rho = g\beta^{'}C_o$. To derive a relationship between concentration and effective area of active leaking, we used the distance between the instabilities as the characteristic length scale in the Grashof number. This is similar to the assumption of Hoyal et al. (1999b) since they take δ as being the thickness of the interface layer, but then propose that the spacing of the instabilities is directly proportional to δ.

Inline with our stated assumption of constant leak thicknesses, the average distance between the leaks is taken as being equal to the thickness of the interface layer and as a multiple of leak thickness, $\delta = \lambda r$ (Figure 2.8). This leads to a non-dimensional instability wavelength, $\lambda = \delta/r$. Note that λ plays the same role as ϕ in Hoyal et al. (1999b); however, we have opted for different notation since we keep plume thickness constant. Substituting instability wavelength, λr, and reduced gravity in equation (2.8) leads to:

$$Gr = \frac{g\beta^{'}C_o\lambda^3 r^3}{\nu^2} \tag{2.9}$$

Rearranging and regrouping the constant terms leads to a function for λ based on the

initial top layer concentration:

$$\lambda = K^{'}\left(\beta^{'}C_o\right)^{-1/3} \tag{2.10}$$

Here, $K^{'}$ is a dimensional constant. To relate the non-dimensional instability spacing parameter, λ, to effective cross-sectional area, a non-dimensional ratio for active area defined as $\alpha = A_f/A$ is proposed. A_f is the portion of the cross section that is occupied by descending plumes and A is the whole cross-sectional area. Correlation between non-dimensional instability spacing and active area based on pure geometry is given by:

$$\alpha = 0.22(\lambda)^{-4/3} \tag{2.11}$$

Combining the geometry relation (equation (2.11)) and the Grashof condition (equation (2.10)) yields the area fraction of active leaking as a function of concentration in the upper layer and a critical Grashof number. Since the flux due to leaking can be described by,

$$F_{s,f} = \rho A_f V_f C = \alpha \rho A V_f C \tag{2.12}$$

the combination of equations (2.11), (2.10) and the plume descent velocity equation (2.7) into equation (2.12) results in model for sediment being advected with the plume descent velocity that is based on concentration in the upper layer and a critical Grashof number.

Unfortunately measurements of the α in the experiments could not be made. However, assuming that the reduction in C from the top OBS is primarily a function of leaking, it is possible to examine the functionality of α. This is done by setting the measured effective

settling velocity and downward flux equal to the leaking flux:

$$AW_{s,eff,ex}C = \alpha AV_fC \tag{2.13}$$

This allows for α to be calculated from the measured $W_{s,eff,ex}$ and V_f simply as $\alpha = W_{s,eff,ex}/V_f$. Then, using the measured α values and the geometric spacing relationship (equation (2.11)), the non-dimensional spacing parameter λ can be also be calculated. Values of α and λ from this procedure are listed in Table 2.1. α and λ for each experiments are also compared to the functionality predicted by equations (2.10) and (2.11) in Figure 2.9. The instability spacing constant, $K^{'}$, needed in these equations was found using the initial experimental conditions and regression of equation (2.10) to the data for λ. The $K^{'}$ value from regression was then used to produce the line for α in Figure 2.9b. The α obtained from the measured $W_{s,eff,ex}/V_f$ data lends credibility to the basic functionality predicted by the critical Grashof equation and the geometry relation (equations (2.10) and (2.11)).

Equation (2.13) can simplify to an expression for bulk settling velocity due to settling driven convection and effective active leaking area that is based on C_o in the buoyant layer. The importance of developing such equation for effective settling velocity has been previously pointed out by Blanchette and Bush (2005) and Yu et al. (2013). Simplifying equation (2.13) leads to a theoretical effective settling velocity $W_{s,eff,th} = \alpha V_f$. Furthermore, substituting in equations (2.7), (2.10), and (2.11) and regrouping the constant terms leads to:

$$W_{s,eff,th} = K^{''}\left(\beta^{'}C_o\right)^{13/9} \tag{2.14}$$

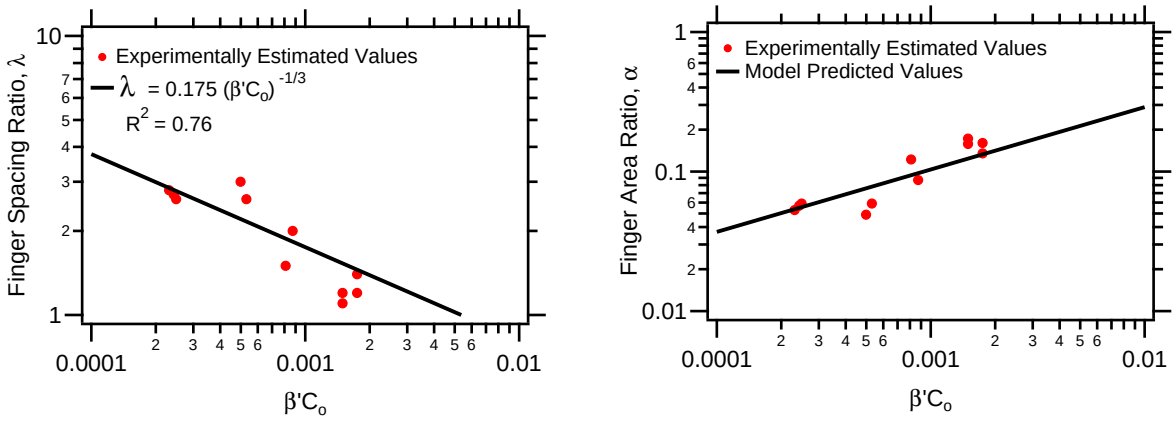

Figure 2.9: a) Fitting equation (2.10) to experimental non-dimensional instability spacing parameters to find the best $K^{'}$ and comparison of the predicted values to experimental values b) Comparison of the experimental non-dimensional leaking area parameters to the predicted values from equations (2.10) and (2.11)

where, $K^{''}$ is velocity constant in units of m/s. Equation (2.14) is one of the key findings of this study. The constant $K^{''}$ contains the critical Grashof number, ν_a, g, and r.

Plotting the effective settling velocities extracted from the concentration time series, $W_{s,eff,ex}$, against the theoretical trend of $W_{s,eff,th}$ from equation (2.14) results in good agreement between the two when $K^{''}$=5.96 (R^2=0.93). The ability of equation (2.14) to capture the trend in $W_{s,eff,ex}$ over the range of experimental $\beta^{'}C_o$ values shows the reasonableness of the $(\beta^{'}C_o)^{13/9}$ dependence. Regression was also done using an equation of the form $W_{s,eff,th} = K^{''}(\beta^{'}C_o)^{P}$ to see if another power other than 13/9 better described the data. However, allowing both P and $K^{''}$ to both be regression coefficients still yielded $P = 1.444$, or 13/9.

2.5 Discussion

2.5.1 Effective Settling Velocity

Yu et al. (2014) numerically measured the effective settling velocity directly from the instability advective flux as $W_{s,eff}=\langle W^{'}C^{'}\rangle$. Their values for sediment sizes of 4 and 20 μm are plotted as a function of concentration along with our data in Figure 2.10. All of the simulations for Yu et al. (2014) are for unflocculated, uniform-sized sediment at much higher concentrations than what we have investigated. Nevertheless, comparing resulting $W_{s,eff}$ values from the two studies yields a few observations that are worth discussing.

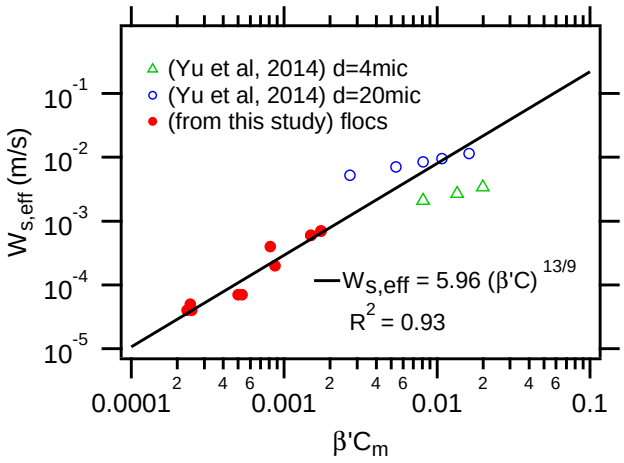

Figure 2.10: Fitting equation (2.14) to experimental effective settling velocities to find the best $K^{''}$, Comparison of the predicted effective settling velocities to experimental values and numerical results of Yu et al. (2014)

Extrapolating our relation to higher concentrations shows that equation 2.14 plots right through the middle of the Yu et al. (2014) effective settling velocities for simulations with 20 μm sediment. This is true even though our sediment technically has an unflocculated mean size of about 5 μm, i.e., clay mud. The fact that our data better aligns with the simulations of silt is not surprising since most of the mud is flocculated. In fact, using our average floc

size of 80 μm and the average floc settling velocity of, $W_{s,f}$=0.4 mm/s actually results in an equivalent Stokes diameter of 21 μm. The comparison therefor suggests that a primary impact of flocculation on interface processes comes simply through alteration of the settling velocity. Secondly, the fact that our effective settling velocity equation is more inline with the 20 μm simulation of Yu et al. (2014) and not the 4 μm further confirms that the interface instabilities in our experiments are more inline with settling-driven leaking and Rayleigh-Taylor properties. The third observation in the comparison is that there is a difference in the functionality of the effective settling velocity between the two studies. In our experiments, $W_{s,eff}$ is more sensitive to concentration than in Yu et al. (2014). It is difficult to know why this is the case. It is possible that the difference in slope could be due to the different ways in which $W_{s,eff}$ was calculated in the two studies, or it could simply be a reflection of the slight process differences between the experimental polysized flocculation suspension and DNS continuum calculations of uniform size solid particles. For example one could speculate that given the same total sediment mass, a suspension of porous flocs, with greater overall surface area, could induce a larger net drag on the surrounding fluid relative to a suspension of solid spheres. Thereby resulting in a stronger dependence of the effective settling velocity on concentration.

2.5.2 $C = C(t)$ Modeling: Top Layer

Here we use the developed effective settling velocity model and initial conditions to predict the top layer trends in $C = C(t)$. The time dependent conservation equation for the top

layer is:

$$\frac{dm}{dt} = -\alpha\rho A V_f C \tag{2.15}$$

Using equations (2.7) and (2.10 - 2.11) and simplifying leads to:

$$\frac{dC}{dt} = \frac{-K''}{h_1}\left(\beta' C\right)^{13/9} C \tag{2.16}$$

Equation (2.16) is more difficult to analytically solve than equation (2.3) due to the changes in the flux formulation. Therefore, equation (2.16) was solved numerically using forward finite difference scheme. For the simulation, we use Δt=60 s, K''=5.96 m/s, volumetric expansion coefficient, β'=0.623, and top layer depth, h_1=0.18 m. Predicted values are compared to the OBS data for $C = C(t)$ in Figure 2.11. The previously introduced lags which are due to point measurements of concentration in the buoyant layer have been applied to predicted data. Figure 2.11 shows that the model is capable of reasonably predicting the measured values of C over all experimental conditions even with the constant coefficient for K''.

2.5.3 Range of Validity for the $W_{s,eff}$ model

The 11 experiments can be divided into two categories in terms of the model's ability to predict the experimental data (Figure 2.11). The first category includes runs 4-7 (moderate C_o), where the model does a good job predicting the experimental data throughout the duration of the experiment. The second category includes runs 1-3 (low C_o) and 8-11 (high C_o). In both the higher and lower concentration runs, the model tends to under-predict removal rates in the later parts of the experiment. We suspect that the failure of the model

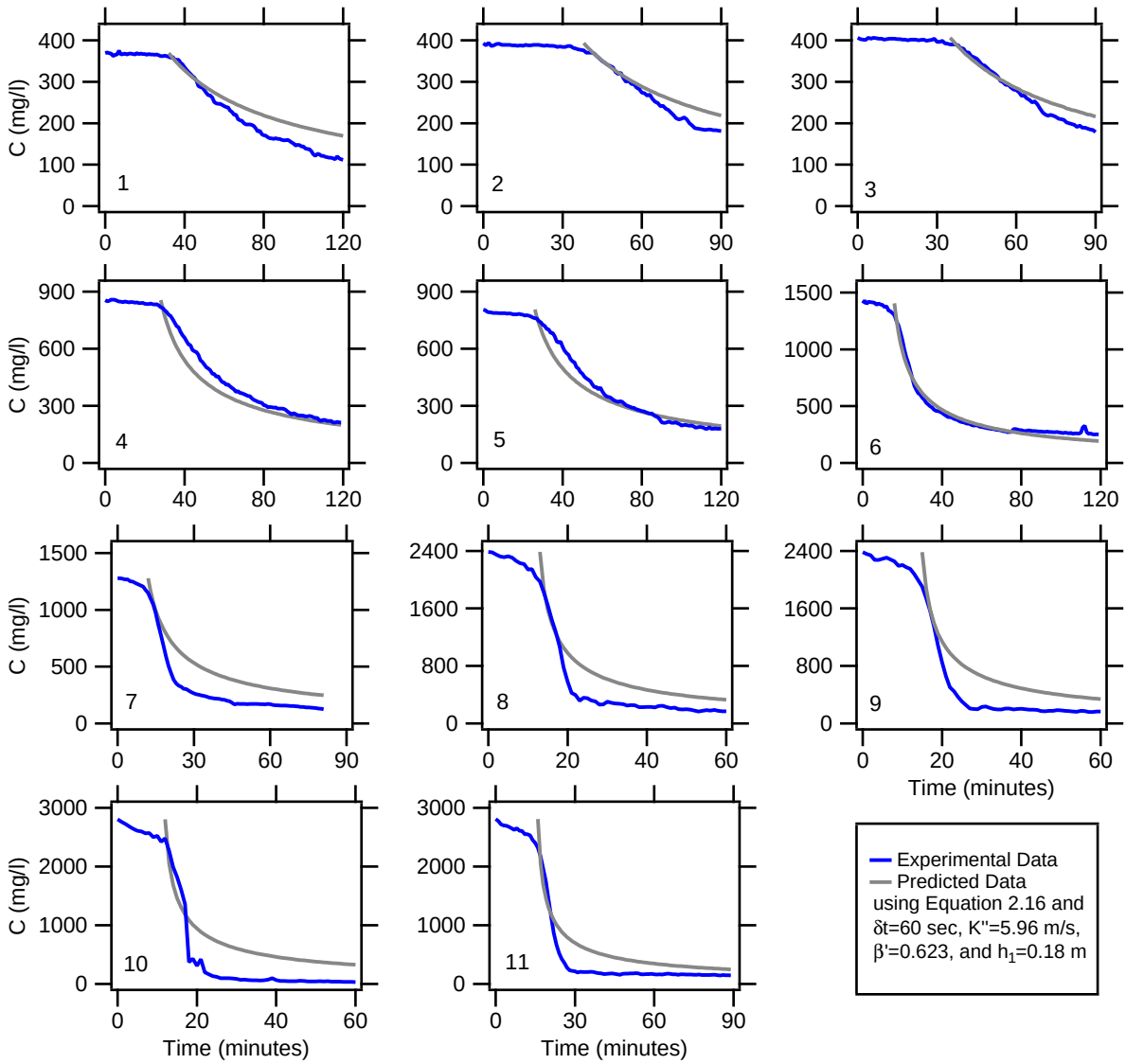

Figure 2.11: Comparison of experimentally measured top layer concentrations with predictions made using equation 2.16

later on in these runs is due to the disappearance of a strong bulk density difference between the interface layer and the underlying ambient.

Figure 2.12a and 2.12c present the predicted time series of C for runs 3 (low C_o) and 9 (high C_o). In the figures the time between the dashed lines highlights the period where the model performed well. Figure 2.12d and 2.12f compare the calculated density of the different layers in the corresponding runs. Again, the dashed lines show the time period where the model performs well. Examining the density time series confirms that the model of removal due to leaking performs well only when the density of the interface layer is higher than the density of the bottom layer. Once the density difference disappears, due to sourcing of sediment to the bottom layer, leaking ceases and the model begins to under predict the removal rate. Interestingly, the effective settling velocity model was able to predict $C = C(t)$ over a larger span of time for the moderate concentration cases (runs 4-7) (Figure 2.12b). Examining the density time series for run 6 (Figure 2.12e) shows that the density of the interface layer is higher than the density of the bottom layer over a longer period of time for this case. We suspect the extended time of significant density difference is responsible for the models good performance over a long span of time.

2.5.4 $C = C(t)$ Modeling: Bottom Layer

We also use the effective settling velocity formulation to model C in the bottom layer. To formulate the governing equation, we assume that sourcing into the bottom layer is due to leaking from above, that sediment leaves the bottom layer through individual particle settling, $\rho A W_{s,f} C$, and that the bottom layer is well mixed due to convection. In the

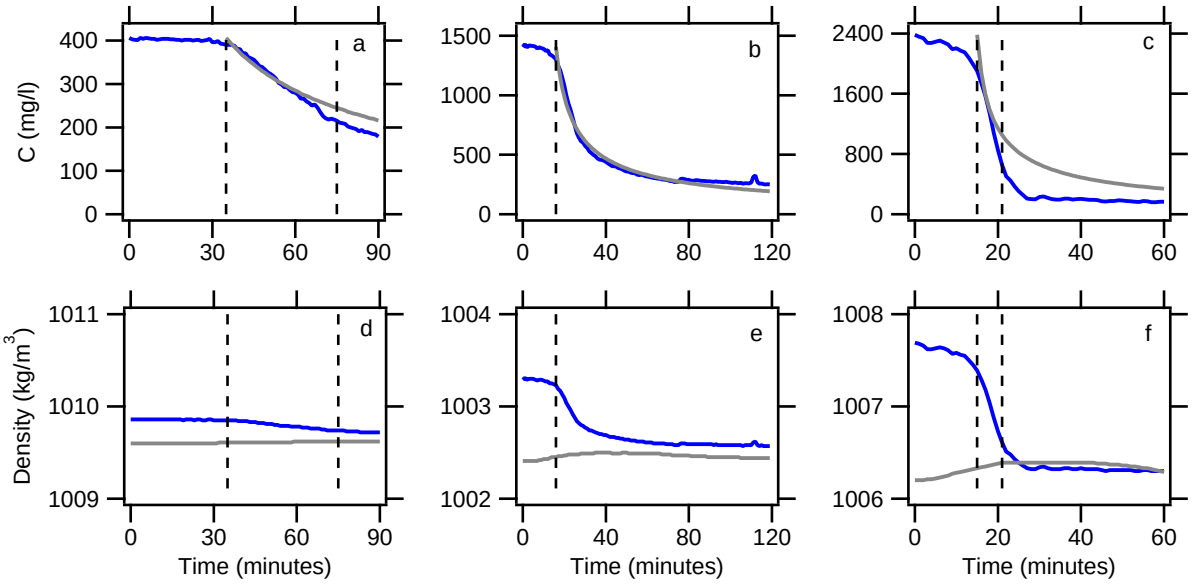

Figure 2.12: From left to right, top row graphs, (a, b, c) present the model performance to predict experimental data and bottom row graphs, (d, e, f) present the excess density analysis of runs 3, 6, and 9 respectively. In the top row graphs, the blue lines are the measured and gray lines are the predicted data. In the bottom row graphs, the gray lines are the densities of bottom layers and the blue lines are the densities of interface layers. From left to right, dashed lines denote the time to kick off and time to cessation of settling driven convections respectively.

model, resuspension from the tank floor is not considered, though can possibly occur if convection is strong enough (Hoyal et al., 1999b). Under these assumptions, the time-dependent conservation equation is:

$$\frac{dm_2}{dt} = \alpha \rho A_1 V_f C_1 - \rho A_2 W_{s,f} C_2 \tag{2.17}$$

where, subscripts 1 and 2 denote the top and bottom layers respectively. Substituting equations (2.7), (2.10), and (2.11) into equation (2.17) and simplifying leads to:

$$\frac{dC_2}{dt} = \frac{A_1}{A_2}\frac{K''}{h_2}\left(\beta' C_1\right)^{13/9} C_1 - \frac{W_{s,f}}{h_2} C_2 \tag{2.18}$$

Equation (2.18) was solved numerically using forward finite difference and the values for Δt, K'', and β' from the top-layer modeling. h_1 and h_2 are the top and bottom layer depths and A_1 and A_2 are the cross-sectional areas.

Equations (2.16) and (2.18) were used to predict the bottom layer concentration time series. Predictions are compared to the experimental data in Figure 2.13. In general, the proposed model reasonably predicts $C = C(t)$. Since the physical distance between the bottom OBS and the fluids interface is almost the same as that between the surface of the top layer and the top OBS, the lags that were introduced previously, which are due to point measurements of concentration, have been applied to predicted data. Among all the runs, a calibrated particle settling velocity of 0.1-0.2 mm/s which corresponds to a floc diameter of 30-50 μm was capable of scaling the outward flux of the suspended sediment from the control volume (Table 2.1). Slower settling velocities and smaller floc diameters than what was observed in experiments can be described in light of the resuspension process.

2.5.5 How Important is the Initial Stability Ratio?

For each initial sediment concentration condition, at least two experiments were run with different salinities in the bottom layer. This was done to examine the importance of bottom-layer salinity and the overall initial system stability ratio R_s on the interface instabilities and the sediment removal rates (Table 2.1). For any pair of experiments with similar C_o, all other parameters were kept constant. Among the pairs, no distinguishable difference was observed in either the plume descent rate or the top layer time series for C (Figure 2.4 and 2.5). This observation is consistent with our proposition that it is the total sediment concentration in

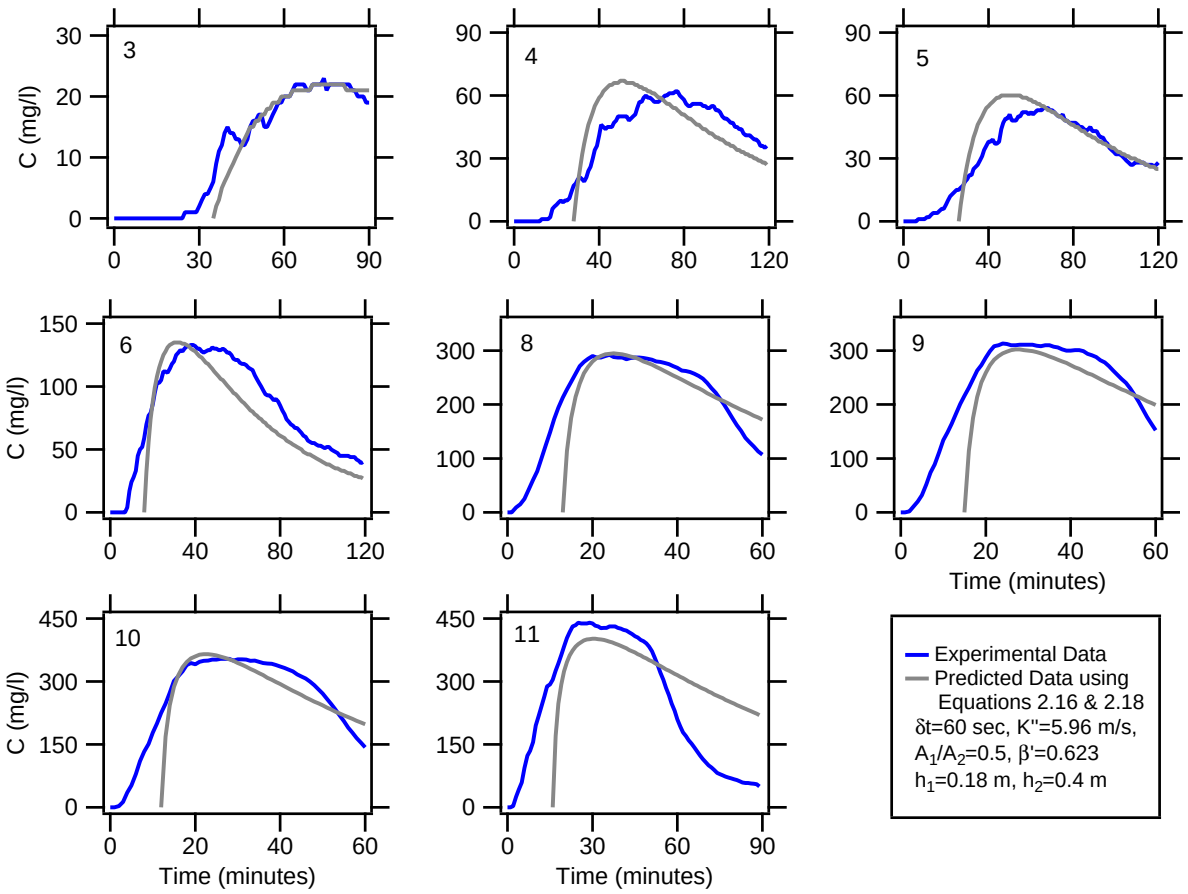

Figure 2.13: Comparison of experimentally measured bottom layer concentrations with predictions made using equations 2.16 and 2.18

the upper layer that dictates the instability plume speed and removal removal rates and not the initial stability of the system based on bulk density.

While the initial stability ratio did not influence the plume speed or removal rate, changing the bottom salinity while keeping the upper layer concentration the same did result in one small systematic difference. All other conditions being equal, the runs with higher salinity tended to produce a very small increase in the peak bottom layer C relative to their lower salinity counterparts (for example, compare panels 4 and 5, 8 and 9, 10 and 11 in Figure

2.4). Our explanation for this is, that the increase in salt sightly reduces the individual floc settling velocity in the lower layer by reducing the submerged specific gravity and thereby reducing the rate of deposition. In the bottom layer, sediment is sourced from the upper layer through interface convection, and sediment leaves the layer through individual floc settling to deposit on the tank floor. Therefore, since top layer C_o sets the rate of sourcing, a small reduction in the deposition rate would lead to a higher concentration within the lower layer.

2.5.6 Floc Behavior at the Interface

An attempt was made to visually track the downward motion of individual flocs during different stages of the experiment. During the interface creation phase, flocs settled downward without much buildup at the fresh and saltwater interface. However, once the interface layer thickened to the point of incipient leaking, the general path of individual flocs falling through the interface layer was modified. Instead of settling down in a straight line, flocs would either be pulled into a convecting plume, or would stagnate at the bottom of the interface layer between descending plumes (Figure 2.14). Flocs that built up here would often slowly make their way towards a leak location and, with time, get sucked into the downward convecting fluid. We suspect that the general circulation pattern generated by the downward convecting plumes is largely responsible for the stagnation of flocs near the interface once leaking began. Downward convecting fluid will drive corresponding upward motion to either side of a descending plume, and it is likely this upward converging motion helps to lock in the plume spacing and to keep the flocculated mixture behaving as a continuum with relatively

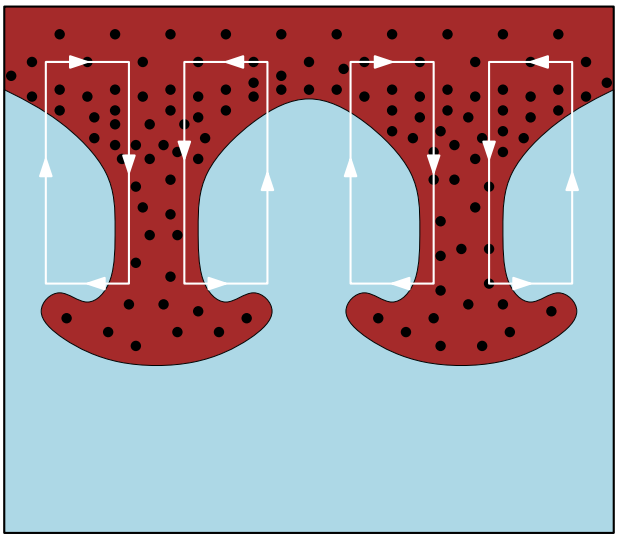

Figure 2.14: Presentation of the settling driven convection through descending plumes, and particle and fluid paths

few flocs settling out between the plumes (Figure 2.14). This circulation pattern and the onset of strong horizontal motions with Rayleigh-Taylor instabilities is discussed in detail in Burns and Meiburg (2015). Furthermore, Burns and Meiburg (2015) show that the salinity interface (located near the top of the interface layer), acts as a lid on the overturning flows generated by the Rayleigh-Taylor instabilities at the bottom of the interface layer and enhances the horizontal motions within the interface.

2.5.7 Flocculation and Settling Instabilities

For the sake of simplicity, past experimental studies have attempted to suppress flocculation during the investigation of settling and double-diffusion interface instabilities. However, one of the goals of this study was to see if floc formation inhibits or alters the growth of such instabilities. Therefore, in our experiments, flocs were both generated prior to the start of each run and they were allowed to grow with time during each experiment. Images of the

flocs during the experiments confirmed that flocs typically grew as the experiment progressed. Floc growth did not, however, seem to alter or change the general nature or downward speed of the instabilities once they started. We suspect that the main influence of flocs is to push the system away from double-diffusive influence and towards settling-driven behavior due to the increase in particle settling velocity relative to unflocculated mud (Burns and Meiburg, 2012; Yu et al., 2013, 2014).

In our experiments, while floc suspension had a much higher settling velocity than the individual unflocculated mud, the flocs still had settling velocities that were lower than the downward convecting plume velocities. One question that this study was not able to investigate is whether or not leaking could be sustained if the individual floc or particle settling velocities were greater than the plume descent rate. Figure 2.15 compares the resultant plume descent rates for a given concentrations with the settling velocities of flocs of any diameter. Settling velocities of different floc diameters based on equation (2.1) are presented as solid black line. Plume descent rates at different concentrations are marked by red dashed lines. Obviously, for higher concentrations, higher plume descent rates are expected. In this figure, for any given concentration and floc size, the region to the left of the solid line shows the area in which the plume descent rate is higher than the floc settling velocity. Data from these experiments all fall in this range.

2.6 Summary and Concluding Remarks

This study has examined settling of flocculated mud from a stagnant, and stably stratified, freshwater mixture overlying saltwater at isothermal conditions. Sediment concentration in

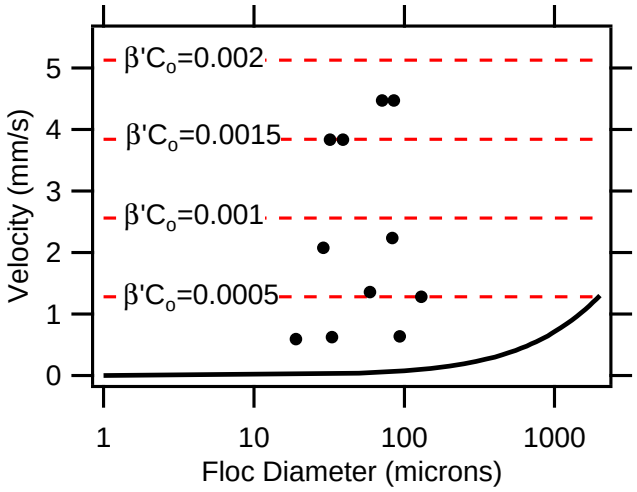

Figure 2.15: Presentation of the resultant plume descent rates for given concentrations along with the settling velocities of flocs of any diameter

the experiments ranged from 0.37 to 2.8 g/l and the salinity differences ranged from 5 to 15 ppt. In all cases, settling driven gravitational instabilities formed and led to continuum convection of a saltwater and sediment laden fluid that formed as mud flocs settled out of the upper freshwater layer to form an interface layer. The thickness of the convecting interface layer was found to be inversely related to initial concentration in the upper layer, nearly disappearing when concentrations where greater than 2 g/l. Continuous measurements of sediment concentration were made at the bottom of the freshwater layer and at the bottom of the saltwater layer. The concentration data was supplemented with multiple spot measurements of floc size and the downward velocity of the convecting plumes.

Several important results came out of these experiments. The first is that flocculation of mud leads to higher settling velocities than would be present without flocculation and therefore the dominance of settling-driven leaking and Rayleigh-Taylor interface instabilities over double-diffusive instabilities.

The second conclusions is that the velocity of settling driven descending plumes is not dependent on the initial bulk stability ratio of the two-fluid system. Instead, it dependents primarily on the concentration of the sediment in the buoyant upper layer and can be very well described by the linear relationship of equation (2.7).

Thirdly, for the experimental conditions tested, the backcalculated effective settling velocities show that downward flux of sediment from the upper layer is on the same order as that predicted from individual floc settling velocity. However, the downward flux also shows systematic deviation with concentration from that predicted by floc settling velocity, and the functionality of this deviation is directly in line with the changes observed in plume decent speed with concentration. This leads us to conclude that removal rates of sediment are influenced by interface instabilities, but that the overall basic magnitude of the removal rate is reasonably predicted by the floc settling velocity. The results also showed that the backcalculated effective settling velocities were much lower than the speed of the instability generated plumes. This implies that an active area of leaking must be defined if descending plume speeds are to be used in predicting overall sediment removal rates from the buoyant layer.

A fourth key outcome of this study was the development of a simple model for predicting the effective settling velocity based on equations for the plume descent speed and the fractional area experiencing leaking. Relations for these two key variables were developed using a simple, cylinder-based force balance that yielded the basic functionally of the plume descent rate, and a thermal-analog critical Grashof relations coupled with geometry and the

assumption of constant diameter instabilities. Combining these two relations gives the effective settling velocity of the mixture due to convection as being proportional to $(\beta' C_o)^{13/9}$ (equation (2.14)). The utility of equation (2.14) is that it can be used along with a standard conservation of mass relation to predict downward flux of sediment due to settling-driven gravitational instabilities.

Bibliography

Blanchette, F. and Bush, J. W. M. (2005). Particle concentration evolution and sedimentation-indiced instabilities in a stably stratified environment. *Physics of Fluids*, 17:073302.

Burns, P. and Meiburg, E. (2012). Sediment-laden fresh water above salt water: linear stability analysis. *Journal of Fluid Mechanics*, 691:279–314.

Burns, P. and Meiburg, E. (2015). Sediment-laden fresh water above salt water: nonlinear simulations. *Journal of Fluid Mechanics*, 762:156–195.

Chen, C. F. (1997). Particle flux through sediment fingers. *Deep Sea Research*, 44, No. 9-10:1645–1654.

Chen, S.-N., Geyer, W. R., Sherwood, C. R., and Ralston, D. K. (2010). Sediment transport and deposition on a river-dominated tidal flat: An idealized model study. *Journal of Geophysical Research*, 115(C10040).

Dyer, K. R. (1989). Sediment processes in estuaries: future research requirements. *Journal of Geophysical Research*, 94(C10):14327–14339.

Geyer, W. R., Hill, P. S., and Kineke, G. C. (2004). The transport, transformation and dispersal of sediment by buoyant coastal flows. *Continental Shelf Research*, 24(7-8):927 – 949.

Geyer, W. R. and Smith, J. D. (1987). Shear instability in a highly stratified estuary. *Journal of Physical Oceanography*, 17:1668–1679.

Gratiot, N. and Manning, A. (2004). An experimental investigation of floc characteristics in a diffusive turbulent flow. *Journal of Coastal Research*, SI 41:105–113.

Green, T. (1987). The importance of double diffusion to the settling of suspended material. *Sedimentology*, 34:319–331.

Green, T. and Kirk, R. (1971). Descent rates of salt fingers. *Nature (Physical Science)*, 232:123–124.

Harris, C. K., Traykovski, P. A., and Geyer, W. R. (2005). Flood dispersal and deposition by near-bed gravitational sediment flows and oceanographic transport: A numerical modeling study of the Eel River shelf, northern California. *Journal of Geophysical Research*, 110(C09025).

Houk, D. and Green, T. (1973). Descent rates of suspension fingers. *Deep Sea Research*, 20:757–761.

Hoyal, D. C. J. D., Bursik, M. I., and Atkinson, J. F. (1999a). The influence of diffusive convection on sedimentation from buoyant plumes. *Marine Geology*, 159(1-4):205 – 220.

Hoyal, D. C. J. D., Bursik, M. I., and Atkinson, J. F. (1999b). Settling-driven convection: A mechanism of sedimentation from stratified fluids. *Journal of Geophysical Research*, 104:7953–7966.

Keyvani, A. and Strom, K. (2013). A fully-automated image processing technique to improve measurement of suspended particles and flocs by removing out-of-focus objects. *Computers & Geosciences*, 52:189–198.

Krone, R. B. (1963). A study of rheological properties of estuarine sediments. Committee on Tidal Hydraulics Final Report 63-88, Waterways Experiment Station, Corps of Engineers, US Army.

Kumar, R. G., Strom, K. B., and Keyvani, A. (2010). Floc properties and settling velocity of san jacinto estuary mud under variable shear and salinity conditions. *Continental Shelf Research*, 30:2067–2081.

Manning, A., Friend, P., Prowse, N., and Amos, C. (2007). Preliminary findings from a study of medway estuary (uk) natural mud floc properties using a laboratory mini-flume and the labsfloc system. *Continental Shelf Research*, BIOFLOW SI:1080–1095.

Manning, A. and Schoellhamer, D. (2013). Factors controlling floc settling velocity along a longitudinal estuarine transect. *Marine Geology*, 345:266–280.

Maxworthy, T. (1999). The dynamics of sedimenting surface gravity currents. *Journal of Fluid Mechanics*, 392(1):27–44.

McCool, W. W. and Parsons, J. D. (2004). Sedimentation from buoyant fine-grained suspensions. *Continental Shelf Research*, 24:1129–1142.

Mietta, F., Chassagne, C., Manning, A. J., and Winterwerp, J. C. (2009). Influence of shear rate, organic matter content, ph and salinity on mud flocculation. *Ocean Dynamics*, 59:751–763.

Parsons, J. D., Bush, J. W. M., and Syvitski, J. P. M. (2001). Hyperpycnal plume formation from riverine outflows with small sediment concentrations. *Sedimentology*, 48(2):465–478.

Parsons, J. D. and Garcia, M. H. (2000). Enhanced sediment scavenging due to double-diffusive convection. *Journal of Sedimentary Research*, 70(1):47–52.

Partheniades, E. (2009). *Cohesive Sediments in Open Channels*. Butterworth-Heinemann/Elsevier, Burlington, MA.

Schmitt, R. W. (1979). Flux measurements on salt fingers at an interface. *Journal of marine Research*, 37:419–436.

Strom, K. and Keyvani, A. (2011). An explicit full-range settling velocity equation for mud flocs. *Journal of Sedimentary Research*, 81:921–934.

Tambo, N. and Hozumi, H. (1979). Physical aspects of flocculation process II. contact flocculation. *Water Research*, 13:441–448.

Turner, J. (1967). Salt fingers across a density interface. *Deep Sea Research*, 14(5):599 – 611.

Winterwerp, J. C. and van Kesteren, W. G. M. (2004). *Introduction to the physics of cohesive sediment in the marine environment*, volume 56 of *Developments in Sedimentology*. Elsevier, Amsterdam, The Netherlands.

Yu, X., Hsu, T.-J., and Balachandar, S. (2013). Convective instability in sedimentation: linear stability analysis. *Journal of Geophysical Research*, 118:256–272.

Yu, X., Hsu, T.-J., and Balachandar, S. (2014). Convective instability in sedimentation: 3d numerical study. *Journal of Geophysical Research: Oceans*, 119:8141–8161.

3 Sedimentation from Buoyant Muddy Plumes in the Presence of Shear Instabilities

3.1 Introduction

Rivers are the primary mechanism for delivery of terrigenous sediment to coastal waters. Dispersal of this sediment from river plumes over the prodelta and broader shelf is highly dependent on the downward vertical sediment flux from the buoyant freshwater layer (Hill et al., 2000; Geyer et al., 2004). Common practice sets this flux as a product of the local plume sediment concentration and the settling velocity of the sediment. In most cases, the settling velocity is determined using standard individual particle settling velocity equations (e.g., Dietrich, 1982; Ferguson and Church, 2004); though some tuning of this value can be needed to allow for adequate matching between predictions and observations (Hoyal et al., 1999a; Harris et al., 2005; Chen et al., 2010). Furthermore, field studies of sediment transport characteristics in the near-field region of river mouth discharges have shown that the measured downward sediment fluxes can be higher than what would be expected from simple unaggregated individual particle settling, i.e., $F = W_s C$ (Hill et al., 2000; Kineke et al., 2000; Fox et al., 2004; Spahn et al., 2009; Nowacki et al., 2012). These observations lead to the idea of needing to define an effective settling velocity, $W_{s,eff}$ to relate the actual flux of sediment to the underlying water as a function of the plume suspended sediment

concentration, C, i.e. $F = W_{s,eff}C$. In this way, the effective settling velocity accounts for mechanisms in addition to individual particle gravitational settling that enhance or reduce the downward flux of sediment.

Flocculation is one such mechanism that can increase the downward flux of mud from river discharges over that predicted by individual settling rate of unaggregated river sediment. Flocculation, the process of aggregation and breakup of clay and silt size material, can complicate the estimation of the individual particle settling velocity since floc sizes and density can vary as a function of the local flow and sediment conditions (Dyer, 1989; Winterwerp and van Kesteren, 2004; Partheniades, 2009). This is perhaps particularly true in river mouth discharges where decaying turbulence levels and increases in salinity can lead to particle growth and increased settling velocities (Hill et al., 2000; Kineke et al., 2000; Fox et al., 2004; Strom and Keyvani, 2016).

Another mechanism that can potentially influence sediment flux in river plumes are gravitational and shear instabilities. Gravitational instabilities are classified by their initiation mechanism as double diffusive (Green, 1987; Chen, 1997; Hoyal et al., 1999a; Parsons and Garcia, 2000) or settling (Hoyal et al., 1999b; Blanchette and Bush, 2005) driven. They appear in the form of positive irregularities in the density field near the stratification interface of two stagnant, or possibly laminar, layers of fluid. As the density irregularities grow, they eventually evolve into downward advecting cells of fluid and sediment mixture in the form of small negatively buoyant plumes (Hoyal et al., 1999b; Burns and Meiburg, 2012; Yu et al., 2013, 2014; Burns and Meiburg, 2015). Instabilities at the stratification

interface can also be driven by shear between the hypopycnal river discharge and the receiving water body. Shear instabilities appear in the form of small rollers or cusps at the base of the plume and large amplitude waves at the stratification interface (Geyer and Smith, 1987; Maxworthy, 1999; McCool and Parsons, 2004; Yuan and Horner-Devine, 2013). These instabilities are known to be a primary means of mass and momentum exchange across the interface (Christodoulou, 1986; Geyer and Smith, 1987; McCool and Parsons, 2004; Yuan and Horner-Devine, 2013), but it has been suggested that they can also increase the vertical flux of sediment through the creation of packets of fluid and sediment within the instability that are locally more dense than the underlying ambient fluid; perhaps due to preferential concentration of sediment particles in zones of high strain around instabilities at moderate Stokes number (e.g., Raju and Meiburg, 1995; Dreier et al., 2000). In any case, the more dense packets of fluid and sediment could lead to small downward convecting plumes that result in rapid vertical transport of sediment (Maxworthy, 1999; McCool and Parsons, 2004; Henniger and Kleiser, 2012). For example, in their laboratory study, McCool and Parsons (2004) observed what they referred to as shear-induced downward flowing sediment plumes. These plumes had descent speeds an order of magnitude higher than the Stokes settling velocity of the suspended sediment. They argued that the increased mixing at the interface led to increases in the quantity of negatively buoyant sediment plumes from the stratification interface, and they therefore proposed a scaling link between the effective settling velocity of the system and turbulent energy.

A related, but slightly different and more general, mechanism for enhanced removal of

sediment from buoyant plumes is that of turbulent mixing. In the Columbia River plume, Spahn et al. (2009) and Nowacki et al. (2012) both found that measured effective settling velocities from the plume at both high and low discharge were greater than what would be expected for the single grains or aggregates that they observed in the estuary. They separated the contributions of single particle settling and turbulent sediment flux using collocated measurements of turbulent shear and suspended sediment concentration. The turbulent sediment flux was found to be almost an order of magnitude smaller than the total removal rates, implying that turbulent mixing was not as significant as individual particle settling in the plume, but that it could be an important mechanism for smaller suspended particle sizes.

In actively flowing river mouth discharges, it seems less likely that double-diffusive or settling driven instabilities will form and augment or replace individual particle settling, since these instabilities have only been observed in stagnant two layer systems. Hence, changes in the effective settling velocity within the near-field plume relative to that of individual particle settling (based on particle or aggregate size at the river mouth) would likely be driven by either flocculation or some form of shear instability induced (1) density anomaly (i.e., the mechanism of Maxworthy (1999) and McCool and Parsons (2004)) or (2) turbulent flux (i.e., the mechanism of Spahn et al. (2009) and Nowacki et al. (2012)). However, the mechanism of enhanced flux due to shear is not well understood, and no simple model exist to predict the effective settling velocity in the presence of shear based on the integral flow and sediment characteristics of the plume. Therefore, the objective of this study is to further explore

the role of interface shear on the effective settling velocity from freshwater suspensions of mud flowing over clear saltwater. We hypothesize that turbulence induced settling can be significant enough to compete with individual floc settling velocities and that the added flux can be linked to the mixing process at the stratification interface.

3.2 Methods

3.2.1 Overview

This hypothesis is tested in a laboratory stratification flume using freshwater suspensions of kaolinite clay overriding clear saltwater. Of significance in our experimental design is that we collect data on the effective settling velocity under steady-state conditions. This is in contrast to a transient, lock-exchange type experiment that is used to examine the interaction of a plume or current head with the ambient basin water (e.g., Maxworthy, 1999; Parsons and Garcia, 2000). Achieving steady-state was deemed important for our study since there can be significant differences in the mixing properties of a propagating plume or current head and the steady-state body (MacDonald and Geyer, 2004; Yuan and Horner-Devine, 2013), while it is the steady or quasi-steady body that delivers the largest volume of sediment during a storm event. During the experiments, measurements of sediment concentration, C, of both the entering and exiting flow were made with time. In addition, we measured profiles of velocity, U, and salinity, S, as well as the distribution of floc sizes, d_f, in both upper and lower layers. The floc size measurements were then used to calculate an average floc settling velocity, $W_{s,f}$. A suspended sediment mass conservation box model was used along with the collected concentration data to back-calculate an effective settling velocity,

$W_{s,eff}$, for different experimental conditions. Details regarding the method for extracting the effective settling velocity from experiments, as well as estimates of floc settling velocity, are elaborated in the results. To test the hypothesis, floc settling velocities are compared to the effective settling velocities, and visual observations and data are then combined with conceptual theory to develop a model for the effective settling velocity based on bulk flow and sediment properties. In this Methods section, we first provide a short background on the quantification of mixing followed by the details pertaining to the experimental setup, procedures, and conditions tested.

3.2.2 Mixing Theory

In stably stratified flows, both the morphologic form of any interface instability and the quantitative fluxes of mass and momentum across the interface are related to the relative magnitude of the difference in velocity (or shear) between the upper and lower layer fluids and the difference in the two fluid's bulk densities (Christodoulou, 1986; Yuan and Horner-Devine, 2013); that is, the ratio of the overturning or mixing forces (the velocity difference between the fluids) and the restorative positive density gradient moving from the free surface downward. This ratio is quantified with the Richardson number, Ri,

$$Ri = \frac{g^{'} h_p}{{U_{ps}}^2} \tag{3.1}$$

where, h_p is the thickness of the plume layer, U_{ps} is the plume surface velocity which also represents velocity gradient since velocity varies linearly from U_{ps} at the free surface down

to zero just below the stratification interface (Geyer and Smith, 1987; McCool and Parsons, 2004; Kilcher et al., 2012; Yuan and Horner-Devine, 2013), and $g^{'}$ is the reduced gravity defined as $g^{'} = g(\rho_a - \rho_p)/\rho_a$. Where, g is the gravity acceleration, ρ_a and ρ_p are the ambient and plume densities. The densities of ambient and plume fluids are calculated using the density of freshwater, ρ_{fw}, as the base fluid and salt and suspended sediment concentrations, S and C, as the density altering agents. Ambient fluid density is calculated as $\rho_a = \rho_{fw}(1 + \beta S)$, where β is the volumetric expansion coefficient for salt defined as $\beta = \delta\rho/\rho\delta S$, and S is the salt concentration expressed in units of mass/mass. Plume density is calculated as $\rho_p = \rho_{fw}(1 + \beta^{'} C_o)$, where $\beta^{'}$ is the volumetric expansion coefficient for sediment defined as $\beta^{'} = \delta\rho/\rho\delta C$, and C_o is the initial sediment concentration expressed in units of mass/mass.

Large Richardson numbers imply strong stability between the layers, whereas small Ri values characterize shear-induced mixing across the interface (Christodoulou, 1986; Geyer and Smith, 1987; Yuan and Horner-Devine, 2013). A critical Richardson number of 0.25 distinguishes between subcritical (Ri >0.25) and supercritical (Ri <0.25) regimes and a significant differences in instability morphology at, and mixing effectiveness across, the interface (Christodoulou, 1986; Geyer and Smith, 1987; Yuan and Horner-Devine, 2013). Note that this critical values switches to 1 when U_{ps} is replaced with the depth averaged velocity since the velocity profile is linear (i.e., U_{avg}=0.5U_{ps}). In natural settings, mixing takes place at the pycnocline and expands the mixing layer until the critical Richardson number of 0.25 is reached (Geyer and Smith, 1987).

The mixing process at the interface leads to entrainment of ambient lower-layer water into the flowing plume. In turn, the addition of the low momentum fluid causes the plume to thicken, and slow. In unconfined basins entrainment across the stratification interface is coupled with lateral expansion of the buoyant layer. In both the laterally confined and unconfined settings, the entrainment process leads to a reduction in both the shear and density difference between the upper layer and ambient as the plume propagates basinward.

Two distinct types of entrainment have been identified at small and large Richardson numbers (Christodoulou, 1986; Yuan and Horner-Devine, 2013) due to a change that occurs in the nature of the interface instabilities. Christodoulou (1986) provided an overview of turbulent mixing at the density interface through theoretical analysis and examination of more than 10 experimental datasets, and related the two types of entrainment to a transition from vortex entrainment (Kelvin-Helmholtz instabilities) to cusp entrainment (Holmboe waves) (Yuan and Horner-Devine, 2013). He suggests that the differentiation in entrainment is related to the distance between the location of primary turbulence production and the interface where it promotes mixing. In the case of vortex entrainment, there is internal turbulence produced in the interface itself. While in the case of cusp entrainment, there is only external turbulence which is produced near the free surface and is related to the inertia of the plume (Christodoulou, 1986). Intuitively, the internal turbulence should be much more efficient in producing mixing than the external one, since the latter has to act on the interface from some distance, over which it is subject to usual dissipation.

Classic parameterization of entrainment, $\delta_e = W_e/U_{avg}$, using a vertical entrainment

velocity, W_e, as some fraction of the plume average velocity, U_{avg}, leads to $\delta_e \propto Ri^{-1/2}$ when the bulk Richardson number (calculated using plume average velocity) is low (Ri <1) corresponding to supercritical regime (Christodoulou, 1986). When the bulk Richardson number is large (Ri >1), the flow is subcritical, and mixing is generated by the continuous bombardment of the interface by vortices generated away from the interface, creating sporadic cusps in the form of Holmboe waves. This process, referred to as cusp entrainment results in a relationship with a larger exponent; $\delta_e \propto Ri^{-3/2}$ (Christodoulou, 1986; Yuan and Horner-Devine, 2013). In subcritical regime, δ_e is related to Richardson number by:

$$\delta_e = \alpha Ri^{-3/2} \tag{3.2}$$

where, α is a coefficient which was found to be 0.007 for Christodoulou (1986). Both mechanisms are active in the intermediate range when bulk Richardson number is near its critical value of unity (Christodoulou, 1986; Yuan and Horner-Devine, 2013).

3.2.3 Experimental Setup

The experimental setup consists of an acrylic flume, an overhead mixing tank, a constant head tank, a gravity fed saltwater replacement system, and a floc imaging system. The flume is 2.5 m long, 0.6 m deep, and 0.113 m wide (Figure 3.1). The first 0.5 m of the flume is separated using a barrier and is equipped with an inlet plate at a height of 0.405 m to facilitate the creation of a plume lofting over a saltwater layer at the beginning of each run. The measurement section, beginning from the inlet, is 1.5 m long and ends with a sharp-

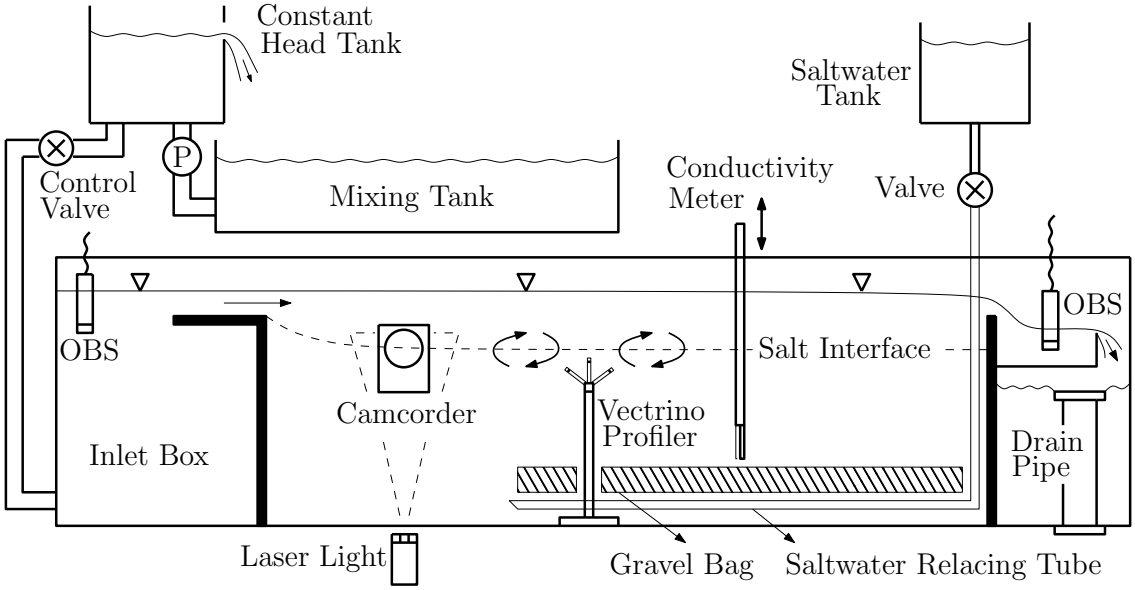

Figure 3.1: Schematic of the stratification flume setup and the experimental equipments

crest weir at the same height as that of the inlet. The measurement section is filled with saltwater of known salinity up to the level of the inlet plate prior to each run. Downstream of the outlet weir, a 0.2 m long and 0.05 m deep bowl collects the suspension that exits the measurement section (Figure 3.1). This collecting bowl provides space to position the OBS sensor to measure the outflow bulk concentration. The fluid that overtops the collecting bowl then enters the standing drain pipe and exits the system. The flume dimensions were designed to allow for placement and operation of the instrumentation and to allow for enough space for multiple instabilities to form across the stratification interface.

Measurement of suspended sediment concentration was carried out at two locations using a pair of OBS 3+ sensors. Both sensors were calibrated with mixtures of the flocculated kaolinite used in the experiment, and were placed to sample along the centerline of the flume at the entrance and exit (Figure 3.1). A digital camcorder was positioned 0.3 m downstream

of the inlet weir to monitor the overall dynamics and development of instabilities at the interface. Lighting for the video was provided by a laser sheet passing through the bottom of the acrylic flume (Figure 3.1). A Nortek Vectrino profiler was fixed upside down, 0.6 m downstream of the inlet weir to measure the plume velocity at 18 evenly spaced vertical locations with a sampling frequency of 32 Hz (Figure 3.1). The Vectrino covers 3.4 cm of the depth with a spatial resolution of 2 mm. The Vectrino was positioned such that the sampling range was 37.0-40.4 cm from the bottom. A MicroScale conductivity instrument was positioned at 1 m downstream of the inlet weir to measure salinity (Figure 3.1). The instrument was equipped to move vertically which enabled us to measure salinity at different elevations with a resolution of 0.5 cm. Prior to each run, the instrument was calibrated with saltwater used in the experiment at room temperature.

A 1000 liter polyethelene tank was elevated above the flume by 2 m, and was equipped with a mixer to prepare the flocculated kaolinite suspension, and keep the material in suspension throughout the run (Figure 3.1). A centrifugal pump transferred the flocculated suspension to a 20 liter constant head tank that was elevated 1 m above the mixing tank (Figure 3.1). The constant head tank prevented the decrease in discharge throughout each experiment ($\approx$30 minutes), and provided a relatively steady condition. Discharge of the suspension to the acrylic flume was controlled with a ball valve.

As the buoyant suspension flows over the saltwater, mixing and entrainment cause the interface to descend. To keep the interface from continually descending throughout the test, we fed saltwater back into the lower layer at a rate equal to that of the plume entrainment

rate (Figure 3.1). This allowed the buoyant layer to reach a steady state. The gravity-driven saltwater replacement setup consists of a 40 liter tank, a valve to control the discharge, and a plastic tube lying on the bottom of the flume with a series of small holes evenly distributed along its length. Gravel bags were placed on top of the tube to dampen the velocity of the saltwater exiting the holes in the tube (Figure 3.1).

During each run, physical water samples were gently extracted from both the overlying flocculated suspension and the underlying saltwater layer using an eight-millimeter inner diameter modified pipette to allow for imaging and sizing of the flocs. Similar methods of floc sampling have been used by (Gratiot and Manning, 2004; Manning et al., 2007; Mietta et al., 2009; Manning and Schoellhamer, 2013). The pipette was then fixed to the top of a settling column, and a floc camera system was used to image the flocs as they settled out of the pipet (Figure 3.2a). Each floc sample was imaged for 1 minute with a frequency of 2 Hz, and at least three samples were taken from each layer in each run. The image analysis routines of Keyvani and Strom (2013) were used to extract the floc size distribution in each frame. The data from the three samples were then averaged to report a single particle size distribution. An attempt to image the flocs within the stratification flume, instead of removing the flocs with the pipette, was attempted. However, the method ultimately failed due to poor lighting.

3.2.4 Experimental Condition and Procedures

For each experiment, a 1000 liter sample of pure kaolinite clay with a disaggregated d_{50} of 9 μm was first prepared by adding the clay to the mixing tank filled with tap water that

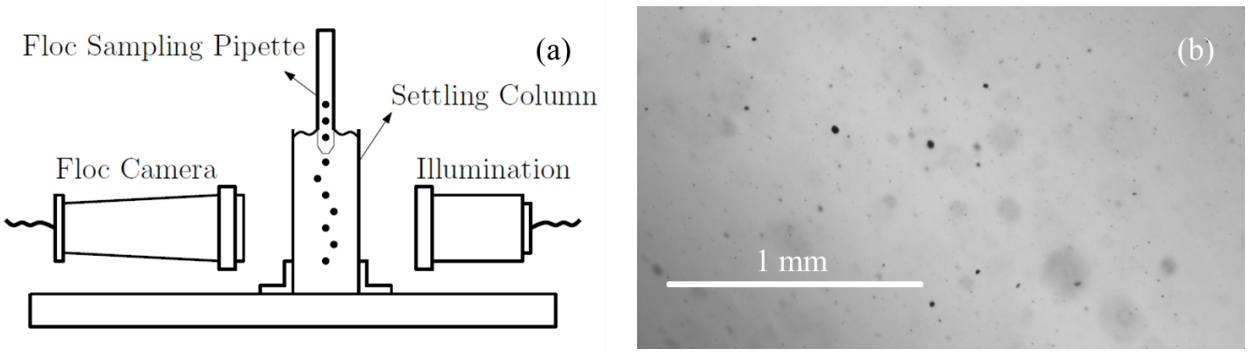

Figure 3.2: a) Schematic of the floc camera setup b) Sample floc image

had been left to sit for 24 hours to ensure that the water was at room temperature. The suspension was then stirred for one hour using a rotating-paddle to generate a flocculated suspension. During mixing, rhodamine dye was added to the mixing tank to provide better contrast in the experiment between the upper and lower layers when illuminated with the laser.

The lower layer fluid was prepared by adding salt to 120 liters of tap water that had been sitting at room temperature for 24 hours. The salinity of the mixture was set by adding specific amounts of salt by mass to the water while mixing. Following this, the salinity was checked with an Atago salt meter to ensure that the desired salinity had been reached. The lower region of the measurement section of the flume was then filled with 80 liters of the saltwater, up to the elevation of the inlet and outlet weirs, 0.405 m, (Figure 3.1). The remaining 40 liters of the prepared saltwater is stored in the saltwater replacement tank and is used later during the experiment.

To start the experiment, the control valve was gently open to fill the inlet box. Each run commenced once the suspension of kaolinite reached the inlet level, entered the measurement

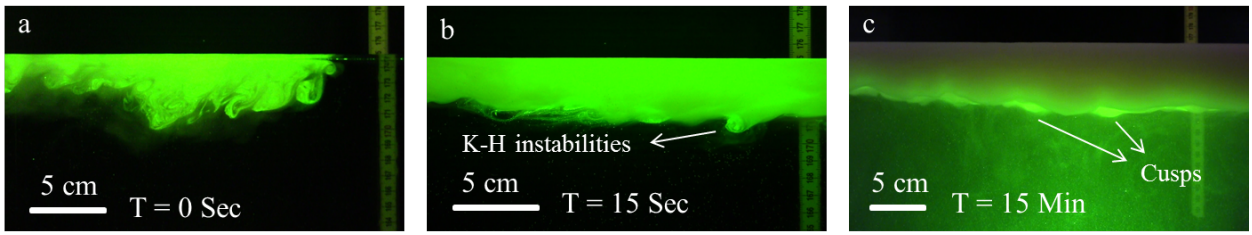

Figure 3.3: The plume and saltwater interface at different instants in time a) When the plume head is rights in front of the camera b) 15 seconds after the plume head has passed and the sharp interface is observed c) When the final steady state is reached

section, and lofted over the saltwater layer. The plume head propagated downstream with a celerity of 3-5 cm/s, and a thickness of 3-4 cm. The head was highly turbulent and mixed vigorously with the saltwater (Figure 3.3a). Interface monitoring and estimations of the Richardson number imply that the mixing at the plume head mostly took place by K-H type shear instabilities (Figure 3.3b). Vortices were generated at the base of the plume, and caused small packets of fluid and sediment to leave the sharp interface and enter the saltwater layer. These vortices typically rolled back inside the plume; though, on occasion, packets did braking away and settling.

Once the plume head reached the outlet weir, the upper portion flowed over the weir while a portion of the lower part of the head lingered along the weir wall. At this point, the saltwater replacement system was started. The system enabled the remainder of the lingering plume to flow over the outlet weir, and kept the plume interface in the measurement section of the flume from continuously descending. Exit of the plume head left only the thin, low-discharge plume body (1-2 cm and 1-2 cm/s) with a sharp interface and no shear instabilities. Following this, the plume discharge was increased in small stepwise increments until the desired plume discharge for each run was reached. A small amount of shear-induced mixing

and saltwater entrainment were stimulated near the leading edge of each small step up in discharge. The increase in discharge and mixing with each step led to an increase in plume thickness with each step. The process of increasing the discharge took several minutes (5-10 minutes) after which the plume hydraulic characteristics such as bulk thickness and velocity became steady.

The depth of the plume was observed visually and recorded once the desired plume discharge and steady state conditions were reached. Discharges of both the kaolinite suspension and the saltwater were calculated manually by measuring the time it took for a fixed volume of fluid to be used during the experiment. Discharge of the kaolinite suspension was also estimated using the velocity profile data and the plume depth readings. Salinity measurements were collected over the vertical through the two layers at 0.5 cm increments.

A summary of the experimental conditions are presented in Table 3.1. Three different initial concentrations and three different plume discharges for each initial concentration were run for a total of nine experiments. In all runs, the salinity of the saltwater was 9 ppt corresponding to a saltwater density of 1005.1 kg/m^3, and the mixture density is less than the density of the ambient saltwater in the basin. The top layer mixture densities, ρ_p, are calculated based on the initial sediment concentrations, C_{in}, and the temperature of the top layer.

Table 3.1: Summary of stratification flume experimental conditions and raw results of 9 runs

Run Name	C_{in} mg/l	C_{out} mg/l	Q_p l/s	Q_{sw} l/s	$C_{out,c}$ mg/l	ρ_p kg/m^3	g' m/s^2	h_p cm	U_{ps} cm/s	Ri -
C1Q1	329	239	0.160	0.021	270	998.40	0.065	5.3	4.14	2.02
C1Q2	361	288	0.296	0.022	309	998.42	0.065	13.1	7.21	1.64
C1Q3	354	293	0.469	0.020	305	998.42	0.065	16.4	10.59	0.95
C2Q1	680	497	0.166	0.020	557	998.62	0.063	6.3	4.01	2.48
C2Q2	699	533	0.210	0.022	589	998.63	0.063	9.8	5.03	2.44
C2Q3	726	607	0.424	0.014	627	998.65	0.063	16.3	10.58	0.92
C3Q1	1624	1133	0.141	0.020	1294	999.21	0.057	5.3	3.81	2.10
C3Q2	1654	1275	0.197	0.019	1398	999.23	0.057	10.8	5.34	2.17
C3Q3	1581	1313	0.350	0.021	1392	999.18	0.058	15.2	8.06	1.35

3.3 Results

3.3.1 General Behavior

At steady state condition, the freshwater suspension entering the basin quickly expanded in the vertical such that it reached its near maximum thickness at ≈ 30 cm from the end of the inlet and then remained nearly constant, at least by eye, along the rest of the measurement section (Figure 3.1). In the expansion region, both cusp and K-H instabilities were observed. However, in the rest of the measurement section, only cusps were observed once steady state conditions had been reach (Figure 3.3c). Calculated Richardson numbers (Table 3.1) show that all of our experiments were in the subcritical regime. Vortices created inside the plume bombarded the visual interface, thereby creating the cusp structures. These cusps continuously disturbed the interface, yet a distinct visual interface remained throughout each experiment. With time, concentration of suspended sediment in the lower layer increased as sediment moved from the plume to the lower saltwater layer (Figure 3.3).

No large-scale mass settling, due to breakaway fluid and sediment packets of more

dense fluid and sediment or local plumes (similar to what would be expected from settling-driven gravitational instabilities), were observed in any of the experiments. Gross visual observations of particles in the lower layer suggested that settling took place at a nearly constant rate with a uniform spatial distribution. However, upon close inspection of the images and video, it was observed that some particles were ejected, non-uniformly, from interface disturbances. The ejection occurred when the disturbances reached their lowest vertical position in the flow, just before they rolled back up into the plume. Particles leaving the disturbances had, at times, slightly higher velocities and local concentrations than those particles settling more uniformly out of the upper layer. This led to small non-uniformities in the sediment concentration and descent speed of the particles just below the interface (see the Supplemental Material for a video highlighting this process). Nevertheless, viscous drag and small convective motions below the interface produced a rather short transition zone to the nearly uniform concentration and particle descent speed that existed over the majority of the lower layer.

3.3.2 C, U, S, and $\mathbf{d_f}$ data

A summary of the primary data from the 9 runs is presented in Tables 3.1 and 3.2 and Figure 3.4. Final steady-state concentrations of both inflow, C_{in}, and outflow, C_{out}, are listed in Table 3.1. The top row of panels in Figure 3.4 shows the normalized downstream velocity at a height of 37-40.4 cm above the bottom of the flume; this range is located inside the flowing upper layer. In Figure 3.4, depth from the free surface is scaled with the thickness of the plume, h_p. In all runs, the velocity profile is linear, similar to other laboratory and field

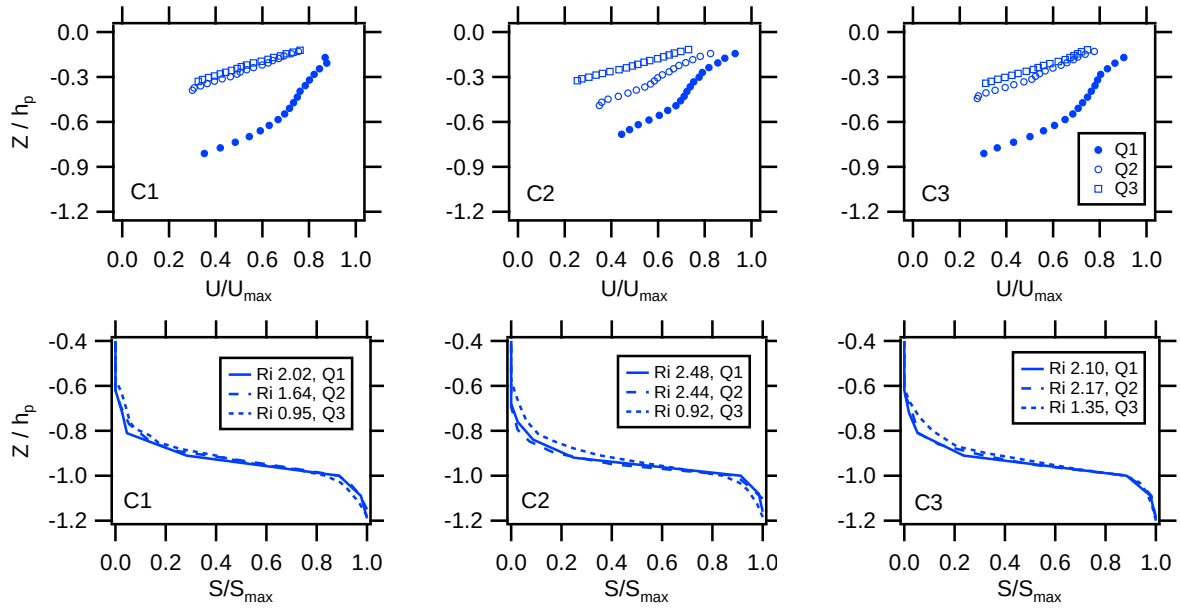

Figure 3.4: Summary of the primary data from the 9 runs of stratification flume experiment. Top row of panels are the velocity profiles at steady state condition. Bottom row of panels are the salinity profiles. In the profiles, the depth was normalized by the visual plume thickness and velocities and salinities were normalized by their maximum value at each run. The left column of panels are for three runs with different discharges for low concentration runs or C_1 runs, (C_{in} ≃350 mg/l), the middle column of panels are for mid concentration runs or C_2 runs, (C_{in} ≃700 mg/l), and the right column of panels are for high concentration runs or C_3 runs, (C_{in} ≃1600 mg/l).

studies of stratified flows (Geyer and Smith, 1987; McCool and Parsons, 2004; Kilcher et al., 2012; Yuan and Horner-Devine, 2013), with a given U/U_{ps} value being reach higher in the plume for lower Ri values (Yuan and Horner-Devine, 2013). The plume surface velocities were estimated by linearly extrapolating the velocity profile to the free surface in each run. The resulting plume surface velocities, U_{ps}, are listed in Table 3.1.

Plume thickness, h_p, plume discharge, Q_p, and the discharge of the replacement saltwater, Q_{sw}, are also listed in Table 3.1. The plume discharge was also calculated by integrating the extrapolated velocity profiles over the Z range from $U = U_{ps}$ to 0 and multiplying by plume width, these are the discharges reported in Table 3.1. The reduced gravity, $g^{'}$, was

Table 3.2: Summary of floc sizes and floc, effective, and shear-induced settling velocities of 9 runs of stratification flume experiment

Run Name	$d_{\mathrm{f50,p}}$ μm	$d_{\mathrm{f50,sw}}$ μm	$\sum_{i=1}^{n} P_i W_{s,fi}$ mm/s	$W_{s,eff}$ mm/s	$W_{s,t}$ mm/s	$\delta_s = W_{s,t}/U_{ps}$ -
C1Q1	18	27	0.180	0.185	0.005	0.001
C1Q2	21	30	0.213	0.269	0.056	0.008
C1Q3	20	30	0.206	0.408	0.202	0.019
C2Q1	16	30	0.178	0.196	0.018	0.004
C2Q2	21	26	0.206	0.212	0.006	0.001
C2Q3	22	23	0.218	0.367	0.149	0.014
C3Q1	15	24	0.171	0.189	0.018	0.005
C3Q2	17	26	0.176	0.195	0.019	0.004
C3Q3	22	28	0.216	0.263	0.047	0.006

calculated in each run based on the fluid densities. Based on the surface velocity definition of the Richardson number (equation. 3.1), Ri varied in the experiments from $Ri \approx 1$ up to $Ri \approx$2.5 (Table 3.1). This is in-line with the subcritical cusp-type interface instabilities observed during the experiments. Among all the runs with similar initial plume concentration, the runs with the lowest discharges had the lowest plume thicknesses and plume surface velocities. These two quantities increase with discharge (Table 3.1). Increase in both velocity and thickness resulted in a net lowering of the Richardson numbers with increase in the plume discharge.

The bottom row of panels in Figure 3.4 shows the steady state salinity profiles. In all cases, the visual plume interface coincides with a point where drastic change was observed in the salinity profile. In the figure, the depth below the surface was normalized by the visual depth of the plume, and salinities were normalized by the maximum salinity in the saltwater layer (9 ppt). The salinity profiles from all the runs look very similar in shape. Salinity starts increasing at a point near the mid depth ($Z/h_p \approx$-0.4) downward. It increases

with a S shape profile (concave up) with a mild slope down to the vicinity of the interface, a few cm above it. Close to the visual interface ($Z/h_p \approx$-0.9) the growth rate of the salinity increases such that the 0.95 maximum salinity is reached at the visual interface. Down from this point, salinity increases with a S shape profile (concave down) with a mild slope until it reaches its maximum at $Z/h_p \approx$-1.2. The only small difference in the salinity profiles of all 9 runs is a slight difference in the concavity of the S shape of the profiles with Ri. This difference is such that for the similar normalized depth, S/S_{max} is higher for the run with lower Richardson numbers (Figure 3.4). This implies that the runs with the highest Richardson number have the lowest saltwater entrainment and vice versa.

The salt entrainment ratio, δ_e, in our experiments was calculated by $\delta_e = Q_{sw}/Q_p$ as an integral value over the entire flume since the plume was confined and the plume width was constant. In our experiment, δ_e ranged from 0.033 to 0.142 with an average of 0.089. The entrainment ratios calculated from equation 3.2 however, ranged from 0.002 to 0.008 with an average of 0.004. The measured δ_e are an order of magnitude larger than the calculated ones. This is possibly due to the vigorous mixing and expansion that occurred just downstream of the inlet (Figure 3.1). The entrainment rate in this region would be much higher than that in the rest of the measurement section where the plume thickness remains approximately constant. It is possible that this explains why the experimental entrainment ratios are higher than the calculated values. Note that the saltwater discharges that were used in our experiments were found through multiple preliminary tests seeking the minimum saltwater discharge needed to keep the interface in place.

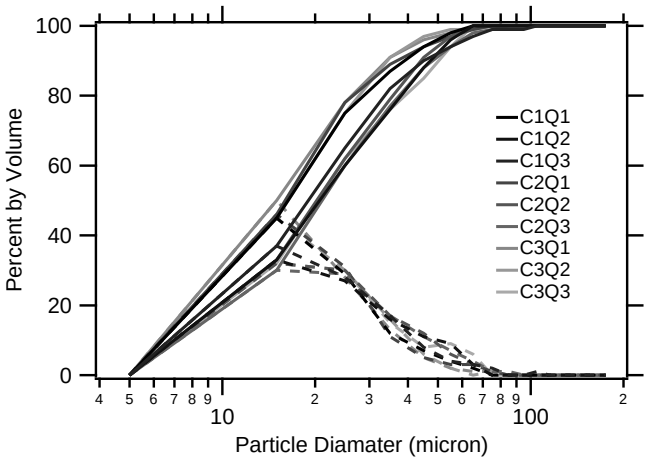

Figure 3.5: Size distributions of the suspended particulates in the upper layer for 9 runs of stratification flume experiment

The size distributions of the suspended particulates in the upper layer of 9 runs are shown in Figure 3.5. The d_{50} of the distributions in both layers for all the runs are listed in Table 3.2. In general, the compact aggregates are small and very similar in size among runs irrespective of the initial concentration or plume discharge. Floc d_{50} ranged from 15 to 22 μm in the upper layer, and from 23 to 30 μm in the lower layer with average of 19 and 27 μm respectively (Table 3.2). Similar floc size among all runs is possible due to (1) the consistence in preparation of the kaolinite suspension, (2) the high mixing levels needed to keep the mixture in suspensions within the mixing tanke (Figure 3.1), and (3) the relatively short residence time the flocs experienced within the lower shear environment of the flume. In all runs, flocs were larger in the saltwater layer than in the plume layer.

3.3.3 Floc and Effective Settling Velocities

Data from the experiments allows for calculation and comparison of two different process rates related to vertical movement of sediment. These two process rates are the individual

particle and floc settling velocity and the effective settling velocity. Both the primary particle and floc settling velocities were calculated using particle size data and settling velocity equations. The d_{50} of the primary particle distribution was used along with Stokes settling velocity equation to calculate primary particle settling velocity. Since the primary particles were the same in all the runs, a single Stokes settling velocity of $W_{s,p}$=0.067 mm/s is used for all experiments. For the flocs settling velocity, the size data from the image analysis routines was used along with the equation (Strom and Keyvani, 2011):

$$W_{s,f} = \frac{gR_s {d_f}^{n_f-1}}{b_1 \nu {d_p}^{n_f-3} + b_2 \sqrt{gR_s {d_f}^{n_f} {d_p}^{n_f-3}}} \tag{3.3}$$

In equation 3.3, R_s is the submerged specific gravity of the particles, d_f and d_p are the floc diameter and the primary particle size respectively, n_f is the floc fractal dimension, ν is the kinematic viscosity of water, and b_1 and b_2 are shape dependent parameters. Based on other flocculation experiments with the same sediment and water mixture (Kumar et al., 2010; Strom and Keyvani, 2011), a fractal dimension of n_f=2 along with shape coefficients of b_1=18 and b_2=0.548 where used; note that because the clay aggregates or flocs were quite low, the calculated values $W_{s,f}$ were fairly insensitive to the n_f value used.

The removal rate that is expected from individual floc settling is equal to the product of the floc settling velocity, $W_{s,f}$, and the floc concentration, C. To calculate the floc settling velocities for each run, floc size distributions of the top layer were used along with equation 3.3. The floc sizes were classified into bins of 10 μm and the fraction, P_i, of flocs in each bin was calculated by weight. Then, for each size bin, settling velocity, $W_{s,fi}$, was calculated

using equation 3.3 and the middle size of that bin. Concentration of flocs in each bin, C_i, was calculated by the product of the probability of the bin times the bulk concentration. Once the concentration and settling velocity for each bin is calculated, a floc size classified settling velocity was calculated as:

$$W_{s,f} = \frac{\sum_{i=1}^{n} C_i W_{s,fi}}{C} = \sum_{i=1}^{n} P_i W_{s,fi} \tag{3.4}$$

Since the floc size distributions are not all that different from run to run, the calculated floc settling velocities are also similar; ranging from 0.171 mm/s up to 0.218 mm/s with an average of approximately 0.2 mm/s (Table 3.2).

The second velocity scale extracted from the data is the effective settling velocity, $W_{s,eff}$, which is defined in this study as the settling velocity needed to satisfy the mass conservation box model. The box model is based on the conservation of suspended sediment mass in the plume making use of four assumptions: (1) sediment is sourced to the upper layer with a mass flow rate of $Q_{s,in}$ which equals the concentration of the inflow, C_{in}, times the plume volume discharge, Q_p; (2) sediment is removed from the control volume at the downstream outlet of the flume at a rate of $Q_{s,out}$, which is a product of the concentration of the outflow, C_{out}, and the combined plume and replacement saltwater discharge, $Q_p + Q_{sw}$; (3) sediment is lost through the base of the plume at a rate of $D = W_{s,eff} C_{in} A$, where A is the interface area; and (4) the upper layer is well mixed.

The outflow concentration is measured inside the collecting bowl just downstream of the sharp crested weir, and contains the freshwater, kaolinite, and saltwater. To determine the

effective settling velocity from the difference between the inflow and outflow concentrations, the outflow concentration must be corrected to ensure that drops in measured concentration are truly due to settling and not due to entrainment of clear ambient saltwater. This can be accomplished using:

$$C_{out,c} = \frac{Q_p + Q_{sw}}{Q_p} C_{out} \tag{3.5}$$

since the volumes of the two fluids in the bowl are proportional to their discharges. The corrected values, $C_{out,c}$, are listed in Table 3.1.

The suspended sediment mass conservation box model for the upper layer under the assumptions mentioned above is:

$$\frac{dm}{dt} = Q_{s,in} - (Q_{s,out} + D) \tag{3.6}$$

Replacing $Q_{s,in}$, $Q_{s,out}$, and D as well as dm/dt=0 (steady state) into equation 3.6 and solving leads to:

$$C_{out,c} = C_{in} \exp\left(\frac{-W_{s,eff} l}{U_{avg} h_p}\right) \tag{3.7}$$

or,

$$C_{out,c} = C_{in} \exp\left(\frac{-W_{s,eff} A}{Q_p}\right) \tag{3.8}$$

where, l is the length of the measurement section, A is the area of the interface (length times width), and U_{avg} is the plume mean velocity. It should be noted that our definition of $W_{s,eff}$ is a generic settling velocity that describes the drop in suspended sediment concentration

of the inflow and outflow based on the time it takes for the plume to travel this distance. Therefore, it is the net effect of all the processes that contribute to the removal and vertical transport of sediment, which include both individual floc settling and any interfacial mixing induced increases or decreases in sediment removal that may occur.

Calculated $W_{s,eff}$ values for the 9 runs range from 0.2 mm/s for the high Ri runs, up to 0.4 mm/s in the runs low Ri values (Tables 3.1 and 3.2). Floc settling velocities and effective settling velocities are plotted against Ri in Figure 3.6. To compare the two velocities among all the runs, bar graphs are plotted in Figure 3.7. Four key observations come examining these figures. First, in all cases the effective settling velocity is greater than, or nearly equal to, floc settling velocity. Second, the discrepancy between the two velocities is larger for the low Ri runs. Third, both velocities are relatively uncorrelated with plume concentration. And, forth, the floc settling velocity is uncorrelated with Ri, whereas the effective settling velocity appear to be sensitive to Ri. Regression gives $W_{s,eff}=0.356Ri^{-0.729}$ with $R^2=0.89$ (Figure 3.6).

These observations reveal that the downward flux of sediment under the influence of shear instabilities is significant enough to compete with flocculation enhanced individual particle settling in our experiments. Shear instabilities enhance the removal fluxes of sediment due to turbulent mixing generated by the shear between the layers.

3.3.4 Effective Settling Velocity Model

The fact that in all runs, the effective settling velocity is greater than the floc settling velocity, and that the discrepancy between the two velocities increase with a decrease in Ri implies

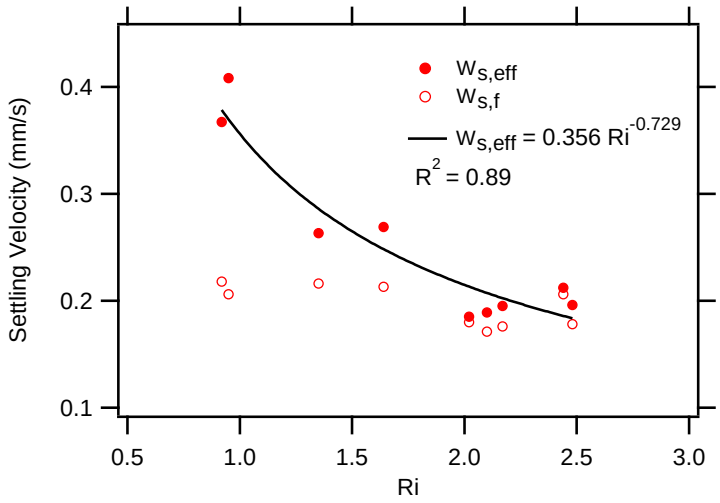

Figure 3.6: Floc and effective settling velocities of 9 runs of stratification flume experiment plotted against Richardson umber

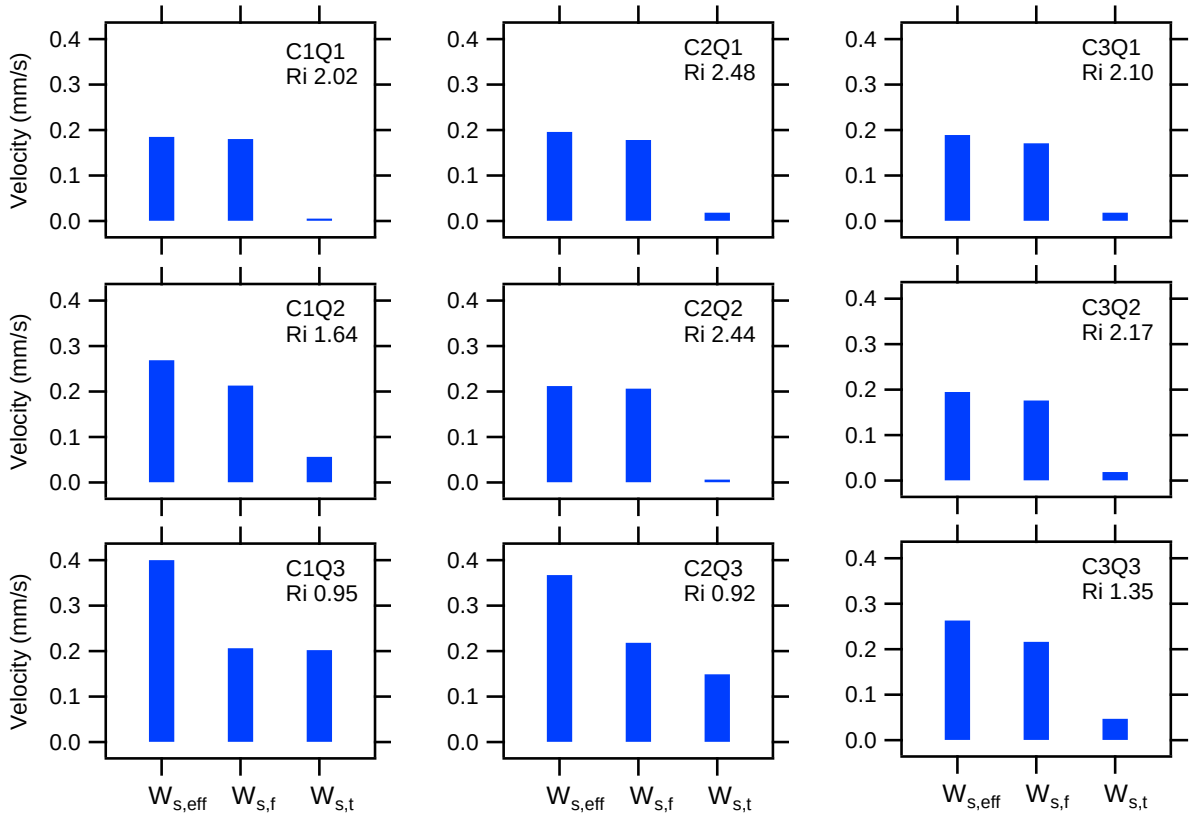

Figure 3.7: Bar graphs of the effective, floc, and shear-induced settling velocities of 9 runs of stratification flume experiment

that the total removal rate is controlled by a combination of floc settling velocity and an additional velocity that is induced by the shear mixing between the layers. This general behavior is similar to the findings of (McCool and Parsons, 2004), but the mechanism for enhancement is more inline with that of Syvitski et al. (1998) and Nowacki et al. (2012). Similar to Nowacki et al. (2012), we fractionate the effective settling velocity into two parts; one dictated by individual floc settling and the other by Ri (turbulence and mixing at the interface). We term this second component of the effective settling velocity the shear-induced settling velocity, $W_{s,t}$, and calculate it as:

$$W_{s,t} = W_{s,eff} - W_{s,f} \tag{3.9}$$

Calculated $W_{s,t}$ values are listed in Table 3.2 and plotted against Ri in Figure 3.8a. They are also included in the bar graphs of Figure 3.7. The calculations show that the shear-induced settling velocity is negligible in the runs with high Ri, but that $W_{s,t}$ grows as large as the floc settling velocity for the low Ri runs. Previously, Nowacki et al. (2012) noted that the shear-induced sediment removal becomes more important for finer particles, which is similar to the case in these experiments since our mud aggregates did not grow into large flocs. Finally, for our experimental condition, $W_{s,t}$ is insensitive to plume concentration (Figure 3.7); suggesting that it is not controlled by density instabilities.

To establish a non-dimensional relation between the shear-induced settling velocity and the Richardson number, $W_{s,t}$ was divided by the plume surface velocity to create a non-dimensional parameter, δ_s, where $\delta_s = W_{s,t}/U_{ps}$ (Table 3.2). The relationship between,

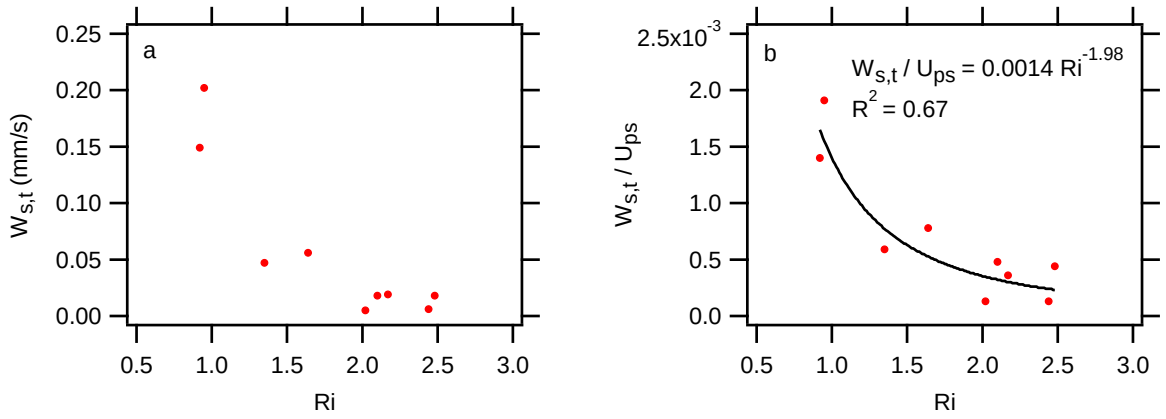

Figure 3.8: a) Shear-induced settling velocities of 9 runs of stratification flume experiment against the Richardson numbers b) Relationship between the non-dimensional shear-induced settling velocity and the Richardson number

δ_s and Ri is shown in Figure 3.8b. Regression shows that δ_s goes with Ri raised to the power of ≈-2 (Fig. 3.8b). Hence, we propose:

$$\delta_s = K_1 Ri^{-2} \tag{3.10}$$

where, K_1 is a non-dimensional constant (equal to 0.0014 in our experiments; see Figure 3.8b). Rearranging equation 3.10 leads to a formula to predict the shear-induced settling velocity as a function of Richardson number and plume surface velocity as follows:

$$W_{s,t} = K_1 U_{ps} Ri^{-2} \tag{3.11}$$

Equation 3.11 is plotted along with our experimental data in Figure 3.9a and the strong linear relationship between $W_{s,t}$ and $U_{ps}Ri^{-2}$ is shown (R^2=0.92). Plugging the definition of Ri (equation 3.1) into equation 3.11 leads to a relationship of $W_{s,t}$ and U_{ps} with an exponent

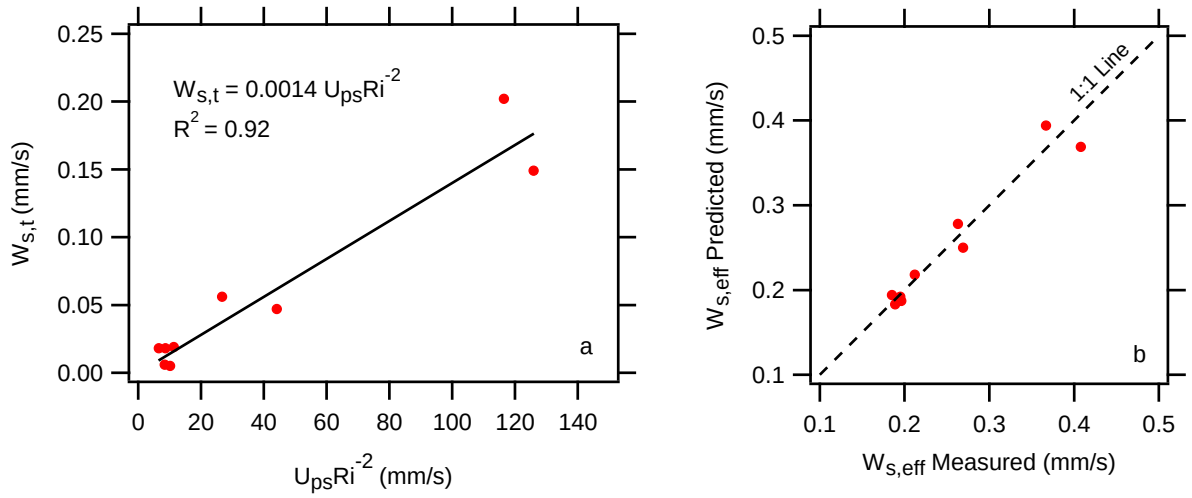

Figure 3.9: a) Linear relationship between $W_{s,t}$ and $U_{ps}Ri^{-2}$ in stratification flume experimental data b) Comparison of the predicted and measured effective settling velocities of 9 runs of stratification flume experiment

of 5:

$$W_{s,t} = K_1(g'h_p)^{-2}{U_{ps}}^5 \tag{3.12}$$

With the relations for $W_{s,t}$ (equation 3.11), predictions of the net effective settling velocities can be made by adding $W_{s,t}$ to the individual floc settling velocity:

$$W_{s,eff} = W_{s,f} + K_1 U_{ps} Ri^{-2} \tag{3.13}$$

The non-dimensional constant, K_1 was set to the value 0.0014 (Figure 3.8b). The comparison between the predicted and measured effective settling velocities of 9 runs is made in Figure 3.9b.

3.4 Discussion

3.4.1 A Conceptual Model to Explain the Functionality of Equation 3.12

The traditional way to calculate the sediment removal flow rate from a plume is by multiplying W_s, and C with the area of the interface, A. The fraction of the sediment removal that is due to the shear instabilities can be formulated in the same way by replacing A and W_s, with surrogates that incorporate the physics involved in enhancement of sedimentation by the shear mixing.

To do this, the total interface area is first replaced with the area of the interface that is disturbed by shear instabilities, i.e., cusps in this study. We term this the active mixing area and denote it by A_m. Intuitively, the active mixing area increases as shear goes up and decreases as the layers become more stable. To build the conceptual model, we propose that $A_m \propto l_m^2$ and that:

$$l_m \propto \frac{{U_{ps}}^2}{g'} \tag{3.14}$$

In this way, l_m increases as the U_{ps} increases or g' decreases. The area of active mixing can be nondimensionalized by the total interface area such that $A_m/A = m$. In this way, m quantifies the fraction of the total interface area that is under active mixing. Since $A_m \propto {l_m}^2$,

$$mA \propto \frac{{U_{ps}}^4}{{g'}^2} \tag{3.15}$$

Since the total interface area, A was constant in our experiments, we can further simplify

equation 3.15 to:

$$m \propto \frac{1}{A}\frac{{U_{ps}}^4}{g'^2} \tag{3.16}$$

Note that A is the total interface area, and therefore is a site specific parameter.

Unfortunately, it was not possible to make measurements of A_m or m in our experiments; however, estimates of the m can been made using the data. To do this, we replace the settling velocity in the traditional flux formula with a product of K_2 (a constant) and the plume surface velocity. In this way, the plume velocity is used as a surrogate for the velocity of packets of fluid and sediment that are transferred across the interface into the saltwater layer by the vortices and cusps. We set the traditional flux formula equal to the flux that is calculated using replaced parameters:

$$AW_{s,t}C = A_m K_2 U_{ps} C \tag{3.17}$$

Rearranging equation 3.17 leads to a linear relationship between m and the normalized shear-induced settling velocity:

$$m = \frac{1}{K_2}\frac{W_{s,t}}{U_{ps}}. \tag{3.18}$$

$W_{s,t}$ and U_{ps} are both measured in our experiments and are related to m through equation 3.18. Combining Equations 3.16 and 3.18 results the following relation between $W_{s,t}$ and U_{ps}:

$$W_{s,t} \propto K_3 {g'}^{-2} {U_{ps}}^5 \tag{3.19}$$

In equation 3.19, K_3 is a dimensional constant with units of m^{-2}. Equation 3.19 is plotted along with the data from the experiments in Figure 3.10. The power function between $W_{s,t}$ and U_{ps} with an exponent of 5, that was found in the results from regression, is further confirmed by this conceptual model and the data from our experiments.

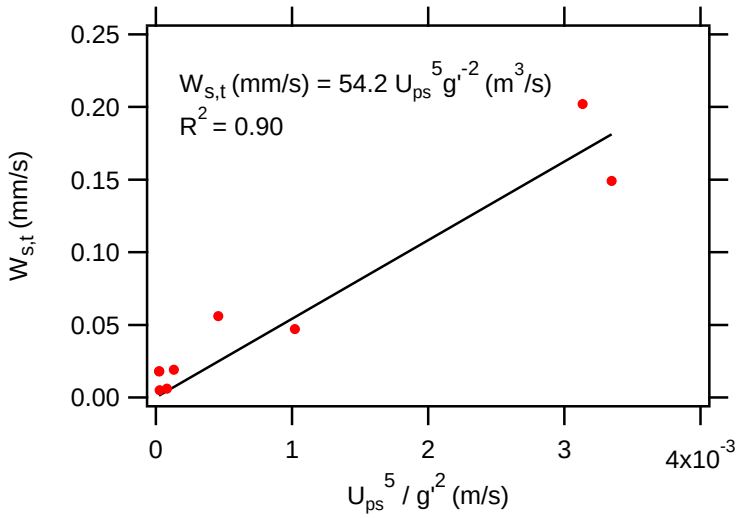

Figure 3.10: Equation 3.19 along with the data from the stratification flume experiments, linear relationship between the shear-induced settling velocity and ${U_{ps}}^5 {g'}^{-2}$.

3.4.2 Modeling Shear-Induced Sediment Flux as a Diffusion Process

The shear-induced sediment removal flux form a buoyant plume can also be modeled as a diffusion process (Syvitski et al., 1998; Nowacki et al., 2012) such that the flux is equal to a diffusion coefficient times the sediment concentration gradient across the layers:

$$W_{s,t}C = D_{s,t}\frac{dC}{dz} \tag{3.20}$$

Here $D_{s,t}$ is the shear-induced sediment diffusion coefficient. In most river plumes, the sediment concentration in the ambient saltwater is negligible with respect to that in the

river plume. Assuming that the concentration in saltwater is zero, and using C/h_p as a first-order approximation of dC/dz along with equation 3.11, leads to an expression for $D_{s,t}$.

$$D_{s,t} = K_1 U_{ps} h_p Ri^{-2} \tag{3.21}$$

$D_{s,t}$ calculated from equation 3.21 will have dimensions of L^2/T which is the dimension of a typical diffusion coefficient and can be used along with equation 3.20 to estimate the shear-induced vertical sediment flux.

3.4.3 Model Application to Other Studies

Here, we examine the capability of equation 3.11 to explain data from the laboratory study of McCool and Parsons (2004) and the field study of Nowacki et al. (2012).

McCool and Parsons (2004) measured the vertical sediment flux from the plume body in a recirculating race track flume and found that the vertical sediment flux was positively related to the plume velocity. Using ADV measurements of velocity, they calculated the rate at which the turbulent kinetic energy was dissipated, ϵ, and linked this to the vertical sediment flux, which was measured using a row of point sensors. All the quantities needed to calculate the Richardson number were directly measured except the plume thickness. However, if it is assumed that turbulent production and dissipation are balanced, the proportionality given by Imberger and Ivey (1991) for plumes,

$$\epsilon \propto \frac{U^3}{h_p} \tag{3.22}$$

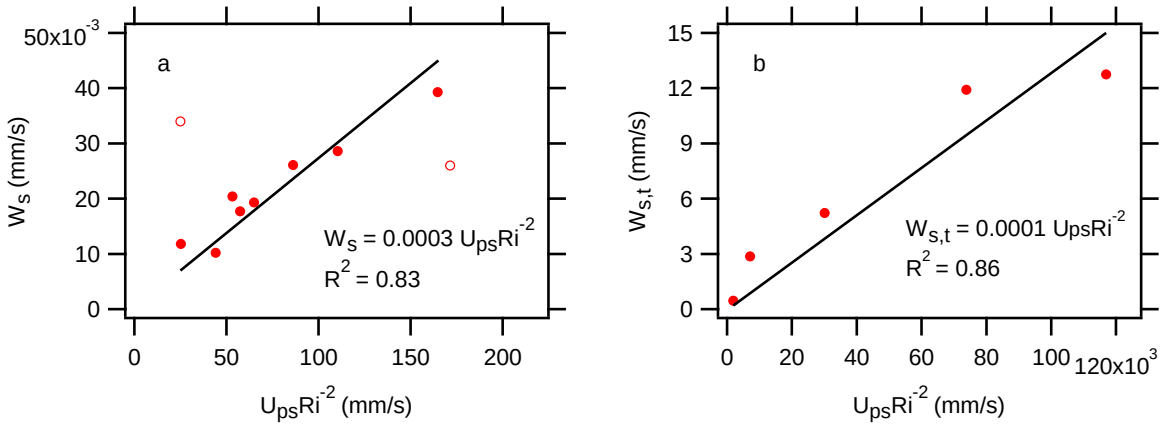

Figure 3.11: a) Settling velocities of the experiments of McCool and Parsons (2004) plotted against the estimations of $U_{ps}Ri^{-2}$ and strong linear relationship between them. Two data points presented by open circles are excluded in calculation of R^2. b) Shear-induced settling velocities of the Nowacki et al. (2012) plotted against the estimations of $U_{ps}Ri^{-2}$ and strong linear relationship between them.

can be used to replace h_p in equation 3.1, leading to $Ri \propto g^{'}U_{ps}/\epsilon$. Plugging this expression of the Richardson number into equation 3.11 gives the settling velocity that is due to shear instabilities. Note that any constant in the proportionality between Ri and $g^{'}U_{ps}/\epsilon$ will be wrapped up in the constant K_1 in equation 3.11 when plotting W_s against $U_{ps}Ri^{-2}$. Settling velocities of the experiments of McCool and Parsons (2004) are calculated by dividing the measured fluxes by the plume concentrations and plotted against the estimations of $U_{ps}Ri^{-2}$ in Figure 3.11a. Regression shows a strong linear relationship between the W_s and $U_{ps}Ri^{-2}$ with a constant K_1 of 0.0003 and R^2 of 0.83. Two of the ten runs of the experiment, presented by open circles in Figure 3.11a, are excluded in the calculation of R^2.

Nowacki et al. (2012) measured the total vertical sediment flux from the Columbia River plume using a control volume method, based on the longitudinal difference of advective sediment flux. They fractionated the total flux into two contributors; flux due to floc

settling and due to turbulent diffusion. They made multiple passes of measurements along a longitudinal line starting from 4 km away from the river mouth. Measured plume surface velocity, thickness, salinity, and sediment concentrations were all used to calculate the Richardson numbers. For the comparison, we use the data from pass 39 of Nowacki et al. (2012) at every 0.5 km between 4 and 6 km away from the river mouth (five points). Pass 39 was chosen for the comparison because it showed the greatest variation in both velocity and concentration. Effective settling velocities for pass 39 were extracted from Figure 8b of Nowacki et al. (2012), and the size-classified floc settling velocity was calculated as 1 mm/s using equation 3.4 and the particulate size data provided in Nowacki et al. (2012). The shear-induced settling velocities were then calculated by subtracting the floc settling velocity from the total effective settling velocity. These effective settling velocities are plotted against estimations of $U_{ps}Ri^{-2}$ in Figure 3.11b. Regression demonstrates that equation 3.11 can capture the primary trend of $W_{s,t}$ versus $U_{ps}Ri^{-2}$ with a constant K of 0.0001 and R^2 of 0.86.

These two comparisons further suggest that $U_{ps}Ri^{-2}$ is a reasonable scaling parameter for the shear-enhanced component of the effective settling velocity in both the laboratory and field.

3.5 Conclusion

We examined the sediment removal rates from suspensions of kaolinite in freshwater flowing over clear saltwater. All experiments were performed in a laterally confined laboratory flume at isothermal conditions, and sediment removal rates were measured during steady-state long

after the plume head had passed. A novel saltwater replacement system was used to eliminate return flow in the flume and achieve steady-state plume thickness along the measurement section. Measurements of particle or floc sizes were made in both the upper and lower layer throughout the duration of the experiment. This data, coupled with incoming and outgoing suspended sediment concentration data, allowed for the measurement of both the individual particle or floc settling velocity and the total effective settling velocity of the system over a range of initial plume concentrations and Richardson numbers.

The data from the experiments showed that the effective settling velocities were equal to or higher than the individual particle settling velocities in all cases. Furthermore, the discrepancy between the two, defined as the shear-induced settling velocity, increased with increases in plume velocity. Mixing at the interface only led to breakaway packets of fluid and sediment descending in small streams or plumes when the head of the current propagated across the basin at the initiation of each experiment. Under steady state conditions, no wholesale leaks or breakaway packets of fluids and sediment were observed. This observation, coupled with a lack of dependence of the shear-induced settling velocity on plume concentration, leads us to conclude that the shear-driven density anomalies of Maxworthy (1999) and McCool and Parsons (2004) were not responsible for the increases in the observed effective settling velocity during the steady state portions of our experiment. Instead of wholesale breakaway and mass settling, we observed that some particles were ejected from the base of the plume when turbulent structures, from within the flow, bombarded the stratification interface. As would have also been the case with the mechanism of McCool and Parsons

(2004), this more general shear or turbulence enhanced removal (similar to that of Nowacki et al., 2012) was found to increase with decreases in the Richardson number.

Based on the empirical data, and the visual observations of the role of turbulent interface disturbances, we proposed a conceptual model for the prediction the turbulence, or shear-induced, settling velocity $W_{s,t}$ that is $\propto U_{ps} Ri^{-2}$ (i.e., equation 3.11 and 3.19). This scaling was also applied to the field data of Nowacki et al. (2012) and the laboratory data of McCool and Parsons (2004) with good results. If the constant of proportionality in the equation 3.11 or 3.19 can be determined for a given plume, then the total effective settling velocity can be calculated as a combination of the individual particle settling velocity and the shear-induced settling velocity (Figure 3.9). An effective settling velocity equation of this nature would be useful for predicting deposition rates from integral river mouth discharge models (e.g., Jirka, 2007; Hetland, 2010; Strom and Keyvani, 2016) or even more detailed hydrodynamic models that cannot resolve the eddying motion at the plume interface by altering the turbulent sediment diffusivity in the vertical direction (equation. 3.21).

For the time being, use of the resulting shear induced settling velocity in a predictive way relies on pre-calibrated or determined constants. Further work is needed to understand the dependence of these constants on physical conditions. Additionally, future work should seek to expand upon the Richardson numbers and suspended sediment and floc sizes examined here in.

Bibliography

Blanchette, F. and Bush, J. W. M. (2005). Particle concentration evolution and sedimentation-indiced instabilities in a stably stratified environment. *Physics of Fluids*, 17:073302.

Burns, P. and Meiburg, E. (2012). Sediment-laden fresh water above salt water: linear stability analysis. *Journal of Fluid Mechanics*, 691:279–314.

Burns, P. and Meiburg, E. (2015). Sediment-laden fresh water above salt water: nonlinear simulations. *Journal of Fluid Mechanics*, 762:156–195.

Chen, C. F. (1997). Particle flux through sediment fingers. *Deep Sea Research*, 44, No. 9-10:1645–1654.

Chen, S.-N., Geyer, W. R., Sherwood, C. R., and Ralston, D. K. (2010). Sediment transport and deposition on a river-dominated tidal flat: An idealized model study. *Journal of Geophysical Research*, 115(C10040).

Christodoulou, G. C. (1986). Interfacial mixing in stratified flows. *Journal of Hydraulic Research*, 24:77–92.

Dietrich, W. E. (1982). Settling velocity of natural particles. *Water Resources Research*, 18(6):1615–1626.

Dreier, T., Blaser, S., Kinzelbach, W., Virant, M., and Maas, H.-G. (2000). Simultaneous measurement of particle and fluid velocities in a plane mixing layer with dispersion. *Experiments in Fluids*, 29(5):486–493.

Dyer, K. R. (1989). Sediment processes in estuaries: future research requirements. *Journal of Geophysical Research*, 94(C10):14327–14339.

Ferguson, R. and Church, M. (2004). A simple universal equation for grain settling velocity. *Journal of Sedimentary Research*, 74(6):933–937.

Fox, J., Hill, P., Milligan, T., and Boldrin, A. (2004). Flocculation and sedimentation on the Po River Delta. *Marine Geology*, 203:95–107.

Geyer, W. R., Hill, P. S., and Kineke, G. C. (2004). The transport, transformation and dispersal of sediment by buoyant coastal flows. *Continental Shelf Research*, 24(7-8):927 – 949.

Geyer, W. R. and Smith, J. D. (1987). Shear instability in a highly stratified estuary. *Journal of Physical Oceanography*, 17:1668–1679.

Gratiot, N. and Manning, A. (2004). An experimental investigation of floc characteristics in a diffusive turbulent flow. *Journal of Coastal Research*, SI 41:105–113.

Green, T. (1987). The importance of double diffusion to the settling of suspended material. *Sedimentology*, 34:319–331.

Harris, C. K., Traykovski, P. A., and Geyer, W. R. (2005). Flood dispersal and deposition by near-bed gravitational sediment flows and oceanographic transport: A numerical modeling study of the Eel River shelf, northern California. *Journal of Geophysical Research*, 110(C09025).

Henniger, R. and Kleiser, L. (2012). Temporal evolution, morphology, and settling of the sediment plume in a model estuary. *Physics of Fluids*, 24(8).

Hetland, R. D. (2010). The effects of mixing and spreading on density in near-field river plumes. *Dynamics of Atmospheres and Oceans*, 49(1):37 – 53.

Hill, P. S., Milligan, T. G., and Rockwell Geyer, W. (2000). Controls on effective settling velocity of suspended sediment in the Eel River flood plume. *Continental Shelf Research*, 20(16):2095–2111.

Hoyal, D. C. J. D., Bursik, M. I., and Atkinson, J. F. (1999a). The influence of diffusive convection on sedimentation from buoyant plumes. *Marine Geology*, 159(1-4):205 – 220.

Hoyal, D. C. J. D., Bursik, M. I., and Atkinson, J. F. (1999b). Settling-driven convection: A mechanism of sedimentation from stratified fluids. *Journal of Geophysical Research*, 104:7953–7966.

Imberger, J. and Ivey, G. (1991). On the nature of tubulence in a stratified fluid. part ii: Application to lakes. *Journal of Physical Oceanography*, 21:659–677.

Jirka, G. H. (2007). Buoyant surface discharges into water bodies. ii: Jet integral model. *Journal of Hydraulic Engineering*, 133(9):1021–1036.

Keyvani, A. and Strom, K. (2013). A fully-automated image processing technique to improve measurement of suspended particles and flocs by removing out-of-focus objects. *Computers & Geosciences*, 52:189–198.

Kilcher, L. F., Nash, J. D., and Moum, J. N. (2012). The role of turbulence stress divergence in decelerating a river plume. *Journal of Geophysical Research*, 117:C05032, doi:10.1029/2011JC007398.

Kineke, G. C., Woolfe, K. J., Kuehl, S. A., Milliman, J. D., Dellapenna, T. M., and Purdon, R. G. (2000). Sediment export from the sepik river, papua new guinea: evidence for a divergent sediment plume. *Continental Shelf Research*, 20:2239–2266.

Kumar, R. G., Strom, K. B., and Keyvani, A. (2010). Floc properties and settling velocity of san jacinto estuary mud under variable shear and salinity conditions. *Continental Shelf Research*, 30:2067–2081.

MacDonald, D. G. and Geyer, W. R. (2004). Turbulent energy production and entrainment at a highly stratified estuarine front. *Journal of Geophysical Research*, 109, C05004:doi:10.1029/2003JC002094.

Manning, A., Friend, P., Prowse, N., and Amos, C. (2007). Preliminary findings from a study of medway estuary (uk) natural mud floc properties using a laboratory mini-flume and the labsfloc system. *Continental Shelf Research*, BIOFLOW SI:1080–1095.

Manning, A. and Schoellhamer, D. (2013). Factors controlling floc settling velocity along a longitudinal estuarine transect. *Marine Geology*, 345:266–280.

Maxworthy, T. (1999). The dynamics of sedimenting surface gravity currents. *Journal of Fluid Mechanics*, 392(1):27–44.

McCool, W. W. and Parsons, J. D. (2004). Sedimentation from buoyant fine-grained suspensions. *Continental Shelf Research*, 24:1129–1142.

Mietta, F., Chassagne, C., Manning, A. J., and Winterwerp, J. C. (2009). Influence of shear rate, organic matter content, ph and salinity on mud flocculation. *Ocean Dynamics*, 59:751–763.

Nowacki, D. J., Horner-Devine, A. R., Nash, J. D., and Jay, D. A. (2012). Rapid sediment removal from the columbia river plume near field. *Continental Shelf Research*, 35:16–28.

Parsons, J. D. and Garcia, M. H. (2000). Enhanced sediment scavenging due to double-diffusive convection. *Journal of Sedimentary Research*, 70(1):47–52.

Partheniades, E. (2009). *Cohesive Sediments in Open Channels*. Butterworth-Heinemann/Elsevier, Burlington, MA.

Raju, N. and Meiburg, E. (1995). The accumulation and dispersion of heavy particles in forced two-dimensional mixing layers. part 2: The effect of gravity. *Physics of Fluids*, 7(6):1241–1264.

Spahn, E. Y., Horner-Devine, A. R., Nash, J. D., Jay, D. A., and Kilcher, L. F. (2009). Particle resuspension in the columbia river plume near field. *Journal of Geophysical Research*, 114:C00B14, doi:10.1029/2008JC004986.

Strom, K. and Keyvani, A. (2011). An explicit full-range settling velocity equation for mud flocs. *Journal of Sedimentary Research*, 81:921–934.

Strom, K. and Keyvani, A. (2016). Flocculation in a decaying shear field and its implications for mud removal in near-field river mouth discharges. *Journal of Geophysical Research, Oceans*, 121:doi:10.1002/2015JC011169.

Syvitski, J. P., Skene, K. I., Nicholson, M. K., and Morehead, M. D. (1998). Plume1.1: Deposition of sediment from a fluvial plume. *Computers and Geosciences*, 24:159–171.

Winterwerp, J. C. and van Kesteren, W. G. M. (2004). *Introduction to the physics of cohesive sediment in the marine environment*, volume 56 of *Developments in Sedimentology*. Elsevier, Amsterdam, The Netherlands.

Yu, X., Hsu, T.-J., and Balachandar, S. (2013). Convective instability in sedimentation: linear stability analysis. *Journal of Geophysical Research*, 118:256–272.

Yu, X., Hsu, T.-J., and Balachandar, S. (2014). Convective instability in sedimentation: 3d numerical study. *Journal of Geophysical Research: Oceans*, 119:8141–8161.

Yuan, Y. and Horner-Devine, A. R. (2013). Laboratory investigation of the impact of lateral spreading on buoyancy flux in a river plume. *Journal of Physical Oceanography*, 43:2588–2610.

4 An Analysis of the Sediment Removal Mechanisms and Rates at Play Along the Length of a River Mouth Plume

4.1 Introduction

4.1.1 Overview

Predicting the fate of terrestrial sediment delivered to coastal areas is predicated on a precise understanding of the mechanisms that affect the sediment removal from the river mouth discharge (Syvitski et al., 1998; Hill et al., 2000; Harris et al., 2005; Chen et al., 2010). When the density of the riverine fluid is less than that of the estuarine fluid, a buoyant (hypopycnal) river plume forms and distributes the sediment in the ambient waters (Mulder and Syvitski, 1995; Gladstone and Pritchard, 2010). For a buoyant plume, where the riverine freshwater and sediment mixture lofts and propagates over the denser saline estuarine water, the most well-known sediment removal mechanisms are: (1) individual particle (floc) settling (Hill et al., 2000; Harris et al., 2005; Chen et al., 2010), (2) convective sedimentation due to gravitational or shear instabilities (Maxworthy, 1999; Hoyal et al., 1999a,b; Parsons et al., 2001; McCool and Parsons, 2004; Yu et al., 2014; Burns and Meiburg, 2015), and (3) turbulent mixing or shear-induced settling (Syvitski et al., 1998; Nowacki et al., 2012). A brief introduction of the above sediment removal mechanisms is provided below.

In a buoyant plume, sediment particles descend under their own weight, leave the plume

layer, enter the ambient saltwater, and eventually deposit to the ocean floor (Hill et al., 2000; Geyer et al., 2004; Chen et al., 2010). Removal of sediment due to gravity acting on the individual particles is referred to here as individual particle settling, and its rate is scaled using typical settling velocity equations. In the presence of cohesive mud, flocculation can increases the individual particle settling velocity through the formation of flocs (Dyer, 1989; Hill et al., 2000; Manning and Schoellhamer, 2013).

While individual disaggregated and aggregated particles settle under their own weight, other mechanisms may enhance sediment removal from buoyant plumes through the onset of downward advecting negatively buoyant packets of fluid and sediment, also known as leaks and/or fingers (Green, 1987; Hoyal et al., 1999a,b; Parsons and Garcia, 2000; Parsons et al., 2001; Burns and Meiburg, 2012; Yu et al., 2013, 2014; Burns and Meiburg, 2015). Fingering and leaking are two different phases of irregular sedimentation due to gravitational instability formation near the stratification interface. Gravitational instabilities are classified by their initiation mechanism as being double diffusive (Green, 1987; Chen, 1997; Hoyal et al., 1999a; Parsons and Garcia, 2000; Burns and Meiburg, 2012; Yu et al., 2013) or settling (Hoyal et al., 1999b; Blanchette and Bush, 2005; Burns and Meiburg, 2012; Yu et al., 2013) driven instabilities. Shear-induced mixing across the interface can also enhances sediment removal and creates irregular deposition (Syvitski et al., 1998; Maxworthy, 1999; McCool and Parsons, 2004; Nowacki et al., 2012). Note that the influence of all the above mechanisms can be wrapped up inside an effective settling velocity, $W_{s,eff}$, that describes the total removal rate (McCool and Parsons, 2004; Henniger and Kleiser, 2012; Yu et al., 2014).

The removal of sediment takes place under a combination of removal mechanisms, but one mechanism often dominates the system (Parsons et al., 2001; Burns and Meiburg, 2012; Yu et al., 2013). In this paper, a few key comparisons are made between the two of the most well-known mechanisms that trigger irregular sedimentation, in order to better understand their role on the total removal in the length of a plume. The two are the settling-driven gravitational instabilities (also known as leaking), and the shear-enhanced settling, that both induce rapid sedimentation rates (McCool and Parsons, 2004; Nowacki et al., 2012; Henniger and Kleiser, 2012; Yu et al., 2014; Burns and Meiburg, 2015). To do so, first, we provide a more detailed background on the physics of the two mechanisms. Then, we make the comparisons in terms of conditions that lead to dominance of one mechanism over the other, and the orders of the magnitude of their influence on the effective settling velocity.

4.1.2 Background

Settling-driven gravitational instabilities develop in stagnant stratified systems due to creation of a layer of fluid that is denser than the fluid below it (Hoyal et al., 1999b; Parsons et al., 2001; Burns and Meiburg, 2012; Yu et al., 2013). The band of heightened density is generated by particles settling across the saltwater interface and creating an unstable band of sediment-laden saltwater, so-called the interface layer. The interface thickens with time as sediment continues to settle. At first, surface tension keeps this layer in place. But, with time, the gravitational forces overcome and lead to downward advection of centimeter scale Rayleigh-Taylor plume structures, at rates that exceed the individual particle settling velocity (Hoyal et al., 1999b; Parsons et al., 2001; Yu et al., 2014; Burns and Meiburg, 2015).

Once packets of fluid begin to descend, the interface layer cease to thicken and a distinct leaking phase commences.

This phenomenon has been experimentally observed by Hoyal et al. (1999b), Parsons et al. (2001), and in Chapter 2 of this study, and examined through linear stability analysis by Burns and Meiburg (2012) and Yu et al. (2013) and Direct Numerical Simulation (DNS) by Yu et al. (2014) and Burns and Meiburg (2015). A few key observations have been that the thickness of the interface layer, and the spacing between points of downward convection tend to increase as concentration goes down. But, the diameters and the downward velocities of the instabilities increase with concentration or sediment settling velocity. These observations imply that the sediment concentration in the upper layer (not the initial stability of the system) plays the major role in setting the instability plume speed, the active leaking area, and the total removal rate (Chapter 2).

When a turbulent layer of freshwater and sediment flows over a stagnant body of saltwater, shear instabilities appear in the form of small rollers, cusps, and large amplitude waves at the stratification interface (Geyer and Smith, 1987; McCool and Parsons, 2004; Yuan and Horner-Devine, 2013). Shear instabilities are known to be the primary mechanism for mixing of mass and momentum across the interface by the means of continuously disturbing the interface. Interfacial mixing influences the removal of sediment and increases the effective settling velocity (McCool and Parsons, 2004; Nowacki et al., 2012). Of note is that physical shapes, dimensions, and effectiveness of mixing alter by the degree of shear between the two layers. Mixing is scaled with the Richardson number, Ri (Christodoulou, 1986; Geyer and

Smith, 1987; Kilcher et al., 2012; Yuan and Horner-Devine, 2013) defined as:

$$Ri = \frac{g^{'}h}{U^2} \tag{4.1}$$

where, h is the thickness of the plume, U is the plume bulk velocity, and $g^{'}$ is the reduced gravity defined as $g^{'} = g(\rho_a - \rho_p)/\rho_a$. Where, g is the gravity acceleration, ρ_a and ρ_p are the ambient and plume densities. The densities of ambient and plume fluids are calculated using the density of freshwater, ρ_{fw}, as the base fluid and salt and suspended sediment concentrations, S and C, as the density altering agents. Ambient fluid density is calculated as $\rho_a = \rho_{fw}(1 + \beta S)$, where β is the volumetric expansion coefficient for salt defined as $\beta = \delta\rho/\rho\delta S$, and S is the salt concentration expressed in units of mass/mass. Plume density is calculated as $\rho_p = \rho_{fw}(1 + \beta^{'}C)$, where $\beta^{'}$ is the volumetric expansion coefficient for sediment defined as $\beta^{'} = \delta\rho/\rho\delta C$, and C_o is the initial sediment concentration expressed in units of $mass/mass$.

Two distinct types of mixing prevail at small and large Richardson numbers due to a change that occurs in the nature of the interface instabilities. The two types are vortex entrainment (Kelvin-Helmholtz instabilities) and cusp entrainment (Holmboe waves) (Christodoulou, 1986; Yuan and Horner-Devine, 2013). A Richardson number of unity distinguishes between vortex entrainment (supercritical) and cusp entrainment (subcritical) regimes. In subcritical regime, irregular and non-uniform ejection of particles from the plume occurs when the disturbances (cusps) reach their lowest vertical position in the flow, just before the fluid rolls back up into the plume. Particles leaving the disturbances have

slightly higher velocities and local concentrations than those particles settling more uniformly out of the upper layer (Chapter 3). No large-scale mass settling due to breakaway fluid and sediment packets of heightened density (similar to leaking) is expected at least, in subcritical buoyant plumes.

Sedimentation from the body of buoyant plumes under the effects of shear instabilities has been experimentally observed by McCool and Parsons (2004) and in Chapter 3 of this study, and studied through field measurements by Nowacki et al. (2012), and Direct Numerical Simulation (DNS) by Henniger and Kleiser (2012). A key observation from these studies is that individual particle settling and turbulent mixing are both modes of sediment removal in the presence of shear instabilities (Nowacki et al., 2012). Moreover, the total removal of sediment is positively related to the plume velocity and turbulent kinetic energy dissipation rate (McCool and Parsons, 2004), and hence inversely related to the Richardson number (Chapter 3). These observations imply that the aggregate settling velocity, the strength of the shear, and the initial stability of the system dictate the removal rates under shear instabilities.

A distinction between leaking and shear-induced sediment removal is whether or not there is turbulence mixing at the interface between the plume and the receiving water body. If there is, then settling-driven Rayleigh-Taylor structures are not expected. However, when mixing is suppressed due to lack of mean plume advection, an interface layer can form that develops leaks. Since profound differences exist both in the nature of the phenomena and in the conditions that lead to dominance of one mechanism over the other, it is of interest

to seek to understand where, and under what conditions, these different mechanisms may impact or drive sedimentation. In the following section we present the difference between the two mechanisms in terms of the dependence of the resultant effective settling velocity on the plume concentration.

4.1.3 Dependence of $W_{s,eff}$ on C

The total sediment removal flow rate from a plume is calculated by multiplying effective settling velocity, $W_{s,eff}$, and sediment concentration, C, with the area of the interface, A. In the case of leaking, $W_{s,eff}$ is a function of the concentration, C, and a calibration coefficient, K_l, and independent of particle settling velocity (Chapter 2). However, in case of shear-enhanced settling, $W_{s,eff}$ is independent of C, and consists of two parts; one due to individual floc settling and the other due to interfacial mixing (Nowacki et al., 2012). Note that the effect of the concentration on floc size is considered a secondary effect. With these two components, the first is dependent on the size of the particulates in the suspension, and the latter is a function of the plume velocity, U, the Richardson number, Ri, and a calibration coefficient, K_t (Chapter 3).

The functionality of $W_{s,eff}$ on C upon the occurrence of leaking in numerical study of Yu et al. (2014), and experiments of Chapter 2 is shown in Figure 4.1a. In the experiments of Chapter 2, $W_{s,eff}$ is more sensitive to concentration than in Yu et al. (2014). The difference in slope could be due to the different ways in which $W_{s,eff}$ was calculated in the two studies. Data from Yu et al. (2014) implies that $W_{s,eff}$ is also a function of the particle size. However, no distinguishable trend was observed in $W_{s,eff}$ as a function of floc size in the experiments

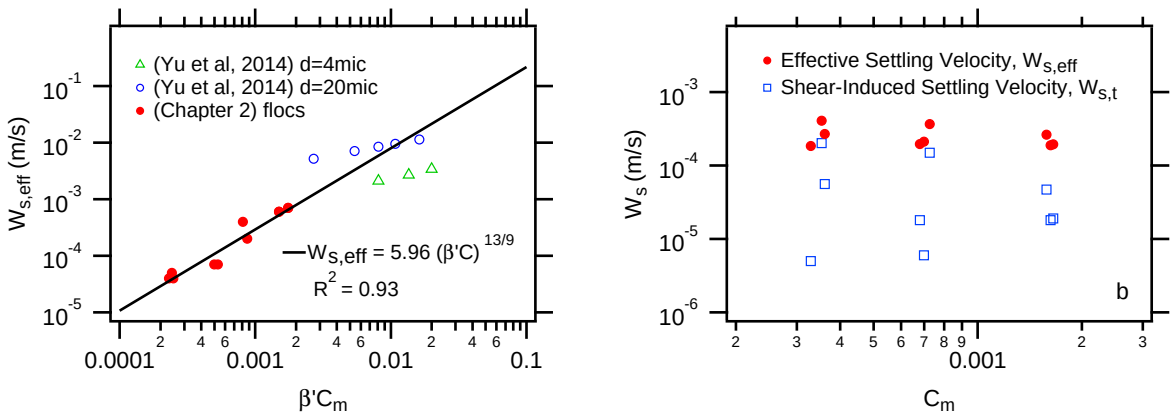

Figure 4.1: a) Functionality of the effective settling velocity, $W_{s,eff}$ on the plume concentration, C, under leaking condition. Data from numerical study of Yu et al. (2014), and experiments of Chapter 2. b) Independence of $W_{s,eff}$ and $W_{s,t}$ on the plume concentration under shear instabilities in experiments of Chapter 3.

of Chapter 2. In Figure 4.1b, $W_{s,eff}$, and its shear-induced fraction, $W_{s,t}$, under the effects of shear instabilities, from Chapter 3 are plotted against C. Near independence of the two velocities on the plume concentration is revealed in the plot. The fact that $W_{s,eff}$ under leaking is only a function of C implies that it can be less than the floc settling velocity, $W_{s,f}$, at some low concentrations. However, under shear instabilities, $W_{s,eff}$ is always greater than $W_{s,f}$ because of the addition of the shear-induced fraction of settling.

The difference in functionality of the effective settling velocity on the parameters under each of the two mechanisms is due to the fact that they are fundamentally different physical mechanisms. In the case of leaking, formation of the unstable interface layer, that appears as anomalies in the density field (Burns and Meiburg, 2012; Yu et al., 2013), and downward motion of convective plumes control the interface dynamics and sediment removal rates. In this case, individual particle settling does not play a significant role, and the effective settling velocity is a strong function of the plume concentration. This is because the active leaking

area and the downward speed of the convections are set by the plume concentration (Chapter 2). Under the effects of shear instabilities, no such density anomalies are observed (Yuan and Horner-Devine, 2013), and sediment removal takes place due to individual particle settling and the shear-induced sediment diffusion (Nowacki et al., 2012). Therefore, shear instabilities do not cause significant alteration to the physics of the settling process. Although, they exert enhancement on the removal rate by the addition of a shear-induced diffusive flux (Chapter 3).

In the following section, we present semi-empirical relations and computational methods that were used in this study to make the comparison in the orders of the magnitude of the settling velocities under the influence of various mechanisms. The goal of this study is to present an analysis that seeks to contextualize the removal rates and zones of operation of these mechanisms over the length of a plume.

4.2 Methods

A quantitative comparison on the extents of the influence of the two mechanisms on the total sediment removal is made by calculation of the individual floc settling velocity and the expected effective settling velocities under each of the two mechanisms. This is followed by a qualitative discussion on the conditions leading to dominance of one process over the other.

Calculations of the individual floc, leak, and shear-induced settling rates are made using settling velocity equation of Strom and Keyvani (2011), and the semi-empirical relations that were developed in Chapter 2 and 3 of this study. A simplified buoyant jet model that includes a flocculation model is used to compute the hydraulic characteristics and the floc sizes of a

hypothetical river plume in the crossshore direction.

When leaking occurs,

$$W_{s,eff} = K_l\left(\beta' C\right)^{13/9} \tag{4.2}$$

where, K_l is a velocity constant in units of m/s that contains a critical Grashof number, kinematic viscosity of the ambient fluid, ν_a, gravity acceleration, g, and thickness of the leaks, r. K_l was found to be 5.96 m/s for the experimental data of Chapter 2.

Under the effects of shear instabilities,

$$W_{s,eff} = W_{s,f} + W_{s,t} \tag{4.3}$$

where, $W_{s,t}$ is the shear-induced settling velocity, and

$$W_{s,t} = K_t U Ri^{-2} \tag{4.4}$$

The non-dimensional constant, K_t was found to be 0.0014 for the experimental data of Chapter 3, and 0.0001 for the field data of Nowacki et al. (2012).

The buoyant jet model (Strom and Keyvani, 2016) solves the 1-D, steady, and layer-averaged governing equations for conservation of fluid mass, volume, and momentum, as well as suspended sediment mass in a laterally unbounded discharge entering a denser ambient basin with no cross flow. The formulation is based on that of Hetland (2010), and assumptions are that vertical and lateral velocities are negligible, that the Boussinesq approximation holds, and that the flow and scalar quantities can be described using top-hat profiles. The

system of equations is solved using fourth-order Runge-Kutta for the plume velocity, U, thickness, h, width, W, and the density anomaly, $\Delta\rho = \rho_a - \rho_p$, from the mouth through the initial few kilometers from the river mouth where the plume dynamics are dominated by shear and advection. The boundary conditions are: initial discharge, Q_o, the river mouth width, W_o, the initial suspended sediment concentration, C_o, and the salinity, S.

To close the system, the entrainment function of Christodoulou (1986) was used:

$$\delta_e = \frac{W_e}{U} = \alpha_e Ri^{-1} \tag{4.5}$$

where, δ_e and W_e are the entrainment ratio and velocity. The calibration parameters for the model are the lift-off Froude number, Frd_{cr}=1.25, and the entrainment coefficient, α_e=0.002, in equation 4.5.

The size of the average floc is also modeled in space as a function of the flow and sediment properties using the Winterwerp (1998) method. This method is based on the conservation of floc number density, a uniform average floc size, and a three dimensional fractal description of flocs. The model balances the floc aggregation rate, A, and the floc breakup rate, B, which are primarily dependent on the turbulent shear-driven collision rate, and turbulent shear stress, respectively, such that the difference between the two rates gives the floc growth rate. The floc aggregation and breakup rates are calculated as:

$$A = K_A G C {d_f}^{4-n_f} \tag{4.6}$$

$$B = K_B G^{q+1} (d_f - d_p)^p {d_f}^{2q+1} \tag{4.7}$$

where, $K_A = {k'}_A {d_p}^{n_f-3}/n_f\rho_s$ and $K_B = {k'}_B({d_p}^{-p}/n_f)(\mu/F_y)^q$. ${k'}_A$ and ${k'}_B$ are collision and breakup coefficients, C is sediment concentration (g/l), G is shear rate defined as $\sqrt{\epsilon/\nu}$ (S^{-1}), ϵ is turbulent kinetic energy dissipation rate, μ and ν are dynamic and kinematic viscosity of fluid, d_f and d_p are floc and primary particle size, ρ_s is density of sediment, F_y is floc strength (=1.0^{-10} N), n_f is floc fractal dimension, and p and q are empirical coefficients (set as 1 and 0.5 in this study).

Assuming that the flocs are at equilibrium (i.e., A=B), and the floc fractal dimension is 2, the equilibrium floc size, d_{fe}, can be calculated as:

$$d_{fe} = d_p + \left(\frac{K_A}{K_B}\right)\frac{C}{\sqrt{G}} \tag{4.8}$$

Floc settling velocity, $W_{s,f}$, is calculated using the equation of Strom and Keyvani (2011):

$$W_{s,f} = \frac{g R_s {d_f}^{n_f-1}}{b_1 \nu {d_p}^{n_f-3} + b_2\sqrt{g R_s {d_f}^{n_f} {d_p}^{n_f-3}}} \tag{4.9}$$

where, R_s is the submerged specific gravity of the particles, and b_1 and b_2 are shape dependent parameters. Based on other flocculation experiments (Strom and Keyvani, 2011), a fractal dimension of n_f=2 along with shape coefficients of b_1=20 and b_2=1.258 where used.

Capability of the layer-averaged model was confirmed, and the calibration parameters were tuned in Strom and Keyvani (2016) using data of the Merrimack River (Massachusetts). We also used information of the Merrimack River at low and high flows, for the boundary

conditions. Merrimack River plume enters the Atlantic ocean through a pair of jetties with a distance of approximately 300 m (Google Earth) and, lifts off for discharges of about 300 cms and higher (Hetland and MacDonald, 2008). Over the last 70 years, the largest flood in Merrimack River was recorded in May of 2006 with a discharge of 2700 cms (Chen et al., 2009; MacDonald et al., 2007). Accordingly, we used, two initial plume discharge, Q_o, of 600 and 2000 cms as low and high flow events, with an initial width, W_o, of 300 m, ambient salinity, S, of 35 ppt, and initial suspended sediment concentration, C_o, of 0.1 g/l. Then, for the case with low initial discharge, a C_o, of 3.0 g/l with three different constant floc sizes of 20, 100, and 200 μm were also examined. For the cases with low initial concentration, the primary particle and the initial floc sizes were 9 and 20 μm, and d_f and d_{fe} were calculated using equations 4.6-4.8 over the crossshore.

4.3 Sediment Removal Rate Comparison

In this section, the floc, shear-induced, and leaking settling velocities of the two plumes with the low sediment concentration and both the low and high discharges are compared. Then, the same comparison is made for the low discharge plume, with a high sediment concentration, and three different floc sizes.

The shear-induced settling velocity was calculated by inputting the plume hydraulic data in equation 4.4, and using three different K_t values. The value of K_t was on the order of O(10^{-4}) in the experiments of Chapter 3, but for the field data of Nowacki et al. (2012), K_t was on the order of O(10^{-5}). The orders of magnitude change of K_t from laboratory to field can be described by the difference in the velocity of a natural plume and that of a

simulated laboratory plume. Note that in equation 4.4, Ri is a non-dimensional number, whereas the plume velocity, U, is dimensional and significantly different in laboratory and field. Therefore, we adopted two values of 10^{-4} and 10^{-5} to K_t in our calculations.

The depth, velocity, density difference, sediment concentration, and floc size of different hypothetical plume cases were calculated over the crossshore distance that the plume remains supercritical. The velocity, depth, sediment concentration, and Richardson number of the case with low Q_o, and low C_o are plotted in Figure 4.2. For the case with high Q_o the trends were the same as those in the case with low Q_o. The main differences between the two cases were: (1) that from the case with low Q_o to the case with high Q_o, the length of the supercritical region increased from 0.7 km to 1.6 km, and (2) that the case with high Q_o has larger depths and velocities, and lower Richardson numbers. The two cases were very much similar in the results of sediment concentration and floc size. The primary observation from Figure 4.2a is that after lift off, the thickness increases and the velocity decreases as the plume propagates basinward, due to interfacial mixing and saltwater entrainment. The decrease and increase in the plume velocity and thickness respectively, result in growth of the Richardson number in the crossshore direction (Figure 4.2b). Note that equation 4.4 is valid for subcritical regime (Chapter 3); however, we assumed that the functionality of $W_{s,t}$ on the Ri with an exponent of -2 holds for the supercritical region. The reasonableness of this assumption is, to some extent, based on the fact that the scaling argument developed in the subcritical laboratory work was able to reasonably describe the trends exhibited in the Nowacki et al. (2012) Columbia River plume data, which was supercritical for the first few

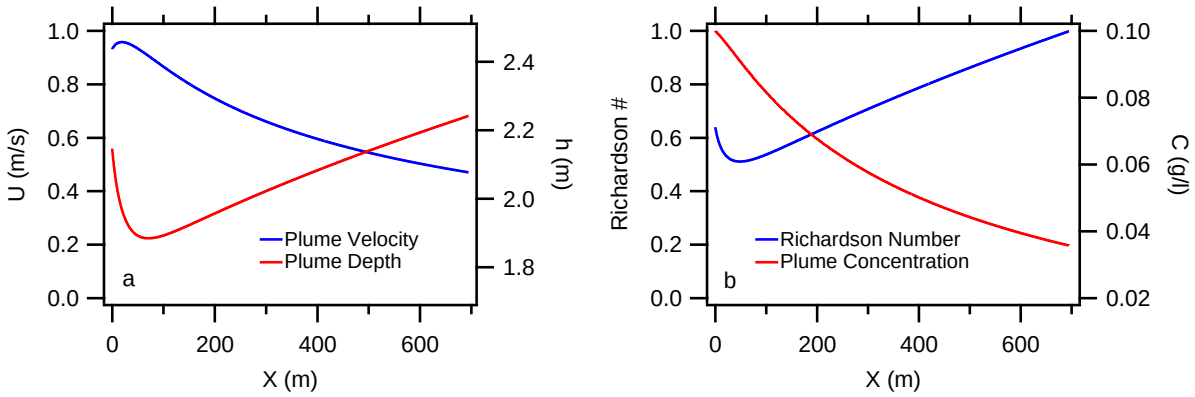

Figure 4.2: a) Velocity and thickness of the plume with low Q_o and low C_o over the crossshore in the supercritical region b) Suspended sediment concentration and Richardson number of the plume with low Q_o and low C_o over the crossshore in the supercritical region

kilometers.

For leaking, the effective settling velocity was calculated by plugging the plume concentration (Figure 4.2b) into equation 4.2, and using a K_l of 10 m/s. In the model, individual floc settling is accounted for and contributes to the drop in C. The floc size, d_f, and the ultimate floc size, d_{fe}, were outputs of the model, and used along with equation 4.9 to calculate the two floc settling velocities over the crossshore. The floc settling velocity, $W_{s,f}$, the ultimate floc settling velocity, $W_{s,fe}$, the leak effective settling, $W_{s,eff}$, and the shear-induced settling velocity, $W_{s,t}$, for two cases of low and high discharge plumes with C_o of 0.1 g/l are compared in Figure 4.3a and Figure 4.3b, respectively. In Figure 4.3, all types of settling velocities are normalized by typical settling velocity of sand particles (1 cm/s) as a reference.

The floc size, based on the Winterwerp (1998) model, remained approximately 20 μm over the crossshore for both low and high-discharge plumes. However, the ultimate equilibrium floc size was nearly constant in the crossshore direction for both cases, being

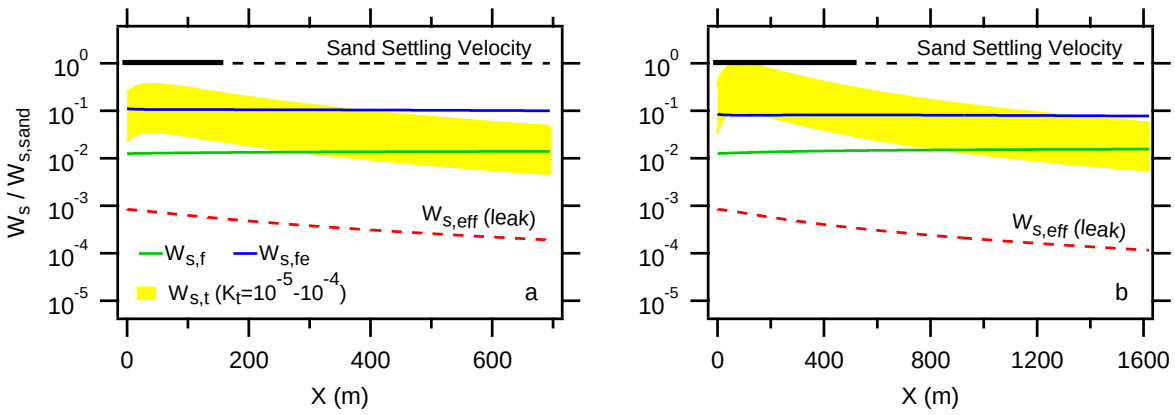

Figure 4.3: a and b present the floc settling velocity, $W_{s,f}$, the ultimate floc settling velocity, $W_{s,fe}$, the leak effective settling, $W_{s,eff}$, and the shear-induced settling velocity, $W_{s,t}$, in space in supercritical region for two cases of low and high-discharge plumes with C_o of 0.1 g/l, respectively. All types of settling velocities are normalized by typical settling velocity of sand particles (1 cm/s) as a reference. The solid black lines present the distance over which the sand is expected to deposit. This approximation is made using the settling velocity of the sand, the velocity and thickness of two plume cases, and by setting $l_{sand} \approx Uh/W_{s,sand}$.

approximately 200 μm for the low-discharge plume, and 150 μm for the high-discharge plume. Therefore, the ultimate floc settling velocity is an order of magnitude greater than that of the flocs, over the crossshore for both cases (Figure 4.3a and b). The difference indicates that flocs were being advected through the system before they could come into equilibrium with local conditions. The shear-induced settling velocity is larger near the river mouth, where the Richardson number is the lowest (Figure 4.2b), and decreases in the crossshore direction as the Richardson number grows. $W_{s,t}$ is on the order of the ultimate floc settling velocity, $W_{s,fe}$, near the river mouth, and drops to the order of the floc settling velocity, $W_{s,f}$, at the end of the supercritical region. This trend is common in both low and high-discharge cases, expect that in the case with higher discharge, the shear-induced settling velocity is slightly larger than that in the case with lower discharge (Figure 4.3). This is because of slightly

lower Richardson numbers in the high-discharge case. The typical settling velocity of sand is greater than that of all other mechanisms. This is the case even in the first few hundred meters for the plume with higher discharge, where the shear-induce settling velocity is the greatest. This point has been made to emphasize the fact that in presence of sand (coarser particle sizes), the share of the individual particle settling in total sediment removal becomes dominant (Nowacki et al., 2012). Therefore, the shear-induced fraction of the total settling velocity, which is independent of particle size and concentration, plays a greater role near the river mouth for smaller particle size distributions.

Leaking is not expected in the supercritical region, but we included the leak effective settling velocity in Figure 4.3 for the sake of comparison. In both low and high-discharge cases, the effective settling velocity due to the leaks is much lower than that of all other mechanisms, and decreases in the crossshore direction as the concentration drops (Figure 4.2b). Note that the leak effective settling velocity only depends on the plume sediment concentration at the time of occurrence of leaking (equation 4.2) and, that in turn depends on its initial magnitude, and the rate at which it is decaying due to the sediment removal from the plume. Since the initial concentration, C_o, was low (0.1 g/l), one could speculate that at higher initial plume concentrations, the effective settling velocity due to leaking can be as large as that of other mechanisms. The difficulty to test higher C_o was that the flocculation model (Winterwerp, 1998) outputs unreasonably large flocs for high concentrations. Therefore, to make a better comparison, we considered a case with a Q_o of 600 cms, a concentration of 3.0 g/l, and three (small, medium, and large) constant floc sizes.

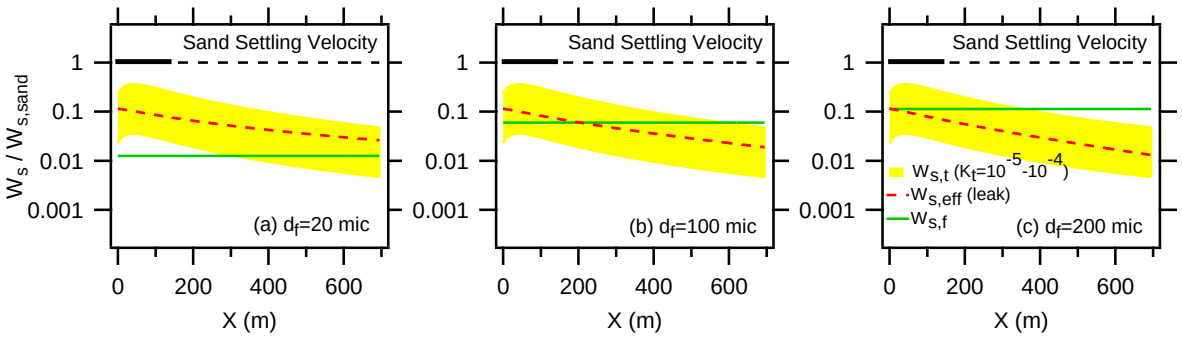

Figure 4.4: a, b, and c present the floc settling velocity, $W_{s,f}$, the leak effective settling, $W_{s,eff}$, and the shear-induced settling velocity, $W_{s,t}$, in space in supercritical region for the plume with lower Q_o, and C_o of 3.0 g/l, with three floc sizes of 20, 100, and 200 μm, respectively. All types of settling velocities are normalized by typical settling velocity of sand particles (1 cm/s) as a reference. The solid black lines present the distance over which the sand is expected to deposit. This approximation is made using the settling velocity of the sand, the plume velocity and thickness, and by setting $l_{sand} \approx Uh/W_{s,sand}$.

The floc settling velocity, $W_{s,f}$, the leak effective settling, $W_{s,eff}$, and the shear-induced settling velocity, $W_{s,t}$, of the plume with lower Q_o, and C_o of 3.0 g/l, with three floc sizes of 20, 100, and 200 μm are compared in Figure 4.4a, b, and c respectively. The three floc sizes correspond to floc settling velocities of approximately 0.1, 0.6, and 1 mm/s. In Figure 4.4, all types of settling velocities are normalized by typical settling velocity of sand particles (1 cm/s) as a reference. In all three cases, the leak effective settling velocity at the end of the supercritical region falls on the range of the shear-induced settling velocities. Comparison between $W_{s,eff}$ due to the leaks in Figure 4.3a and that in Figure 4.4a, b, and c (low and high C_o) reveals that considerable removal of sediment due to leaking is only expected at high plume concentrations.

In Figure 4.5a, the sediment concentration for the plumes with d_f of 20, 100, and 200 μm are plotted in space. In Figure 4.5b, the expected leak effective settling velocities at the

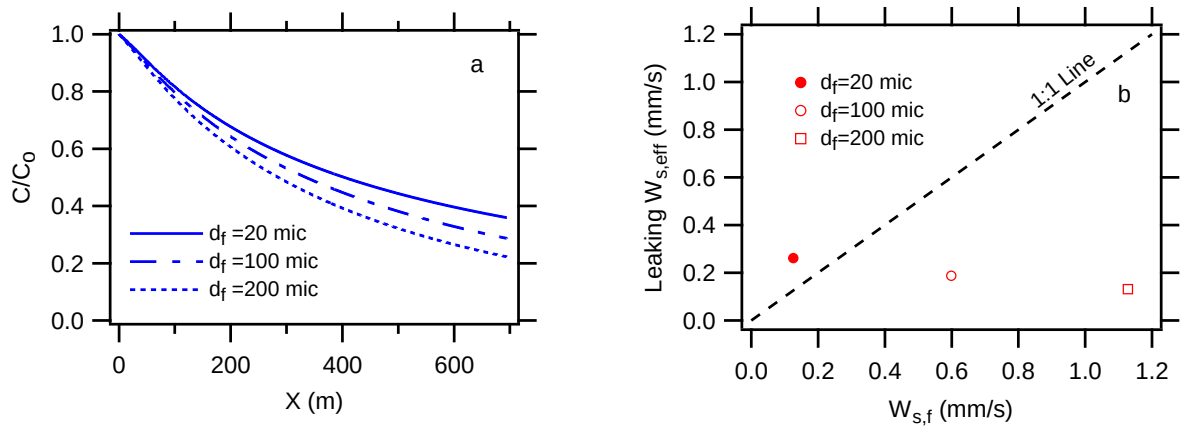

Figure 4.5: a) The suspended sediment concentration in space for the plume with lower Q_o, and C_o of 3.0 g/l, with three floc sizes of 20, 100, and 200 μm b) Comparison of the expected leak effective settling velocities at the end of the supercritical region with the floc settling velocities for the three floc sizes

end of the supercritical region are compared with the floc settling velocities for the three floc sizes. For the case with floc size of 20 μm, the leak effective settling velocity is larger than the floc settling velocity at the end of the supercritical region (Figure 4.4a and 4.5b). However, for the cases with floc sizes of 100 and 200 μm, the effective settling velocity due to the leaks is lower than that of flocs (Figure 4.4b, c, and 4.5b). The reasons are that the floc settling velocity is greater for larger flocs, and that the plume concentration decays slower in the case with smaller flocs. In the case with smaller flocs, concentration decays slower, such that it is larger at the end of the supercritical region, so the expected leak effective settling velocity is higher than that in the cases with larger flocs.

4.4 Where Might the Different Mechanisms Operate

Figure 4.6 provides a schematic of a river plume highlighting where various sediment removal mechanisms may be operating along the length of the plume, along with the relative magni-

tude of each. The general description is that near the river mouth, once the river lofts over the ambient saline seawater, the plume goes supercritical and highly turbulent, such that the vortex entrainment induce intense mixing at the density interface (Yuan and Horner-Devine, 2013; Horner-Devine et al., 2015). In this region, removal of sediment is expected due to the individual particle and the shear-induced settling mechanisms. The supercritical region is on the order of O(10^3) m long for our hypothetical cases, and natural river plumes (Horner-Devine et al., 2015). Of note is that the settling velocity of sand is much higher than that of other mechanisms (Figure 4.3 and 4.4). So, the sand is expected to deposit very close to the river mouth, in crossshore distances on the order of O(10^2) m. This approximation is made using sand settling velocity of 1 cm/s, the plume velocity and thickness in our hypothetical cases, and by setting $l_{sand} \approx Uh/W_{s,sand}$.

Moving away from the inlet, the flow slows and expands in the vertical and lateral directions due to shear, buoyant spreading, entrainment, and the loss of the constant downstream-oriented gravitational body force present in the confined river (Figure 4.2a). As flows continue to slow and thicken, Ri increases and eventually becomes subcritical at distances from the inlet on the order of O(10^3) m. When this occurs, interface mixing reduces due to the transition from vortex to cusp entrainment. In this subcritical region, individual particle settling and shear-induced settling are still the two mechanisms that are expected to operate in removing sediment from the plume.

To our knowledge, no research has been done on the transition from settling under the effects of shear instabilities to that under leaking. However, it is known that the leaking

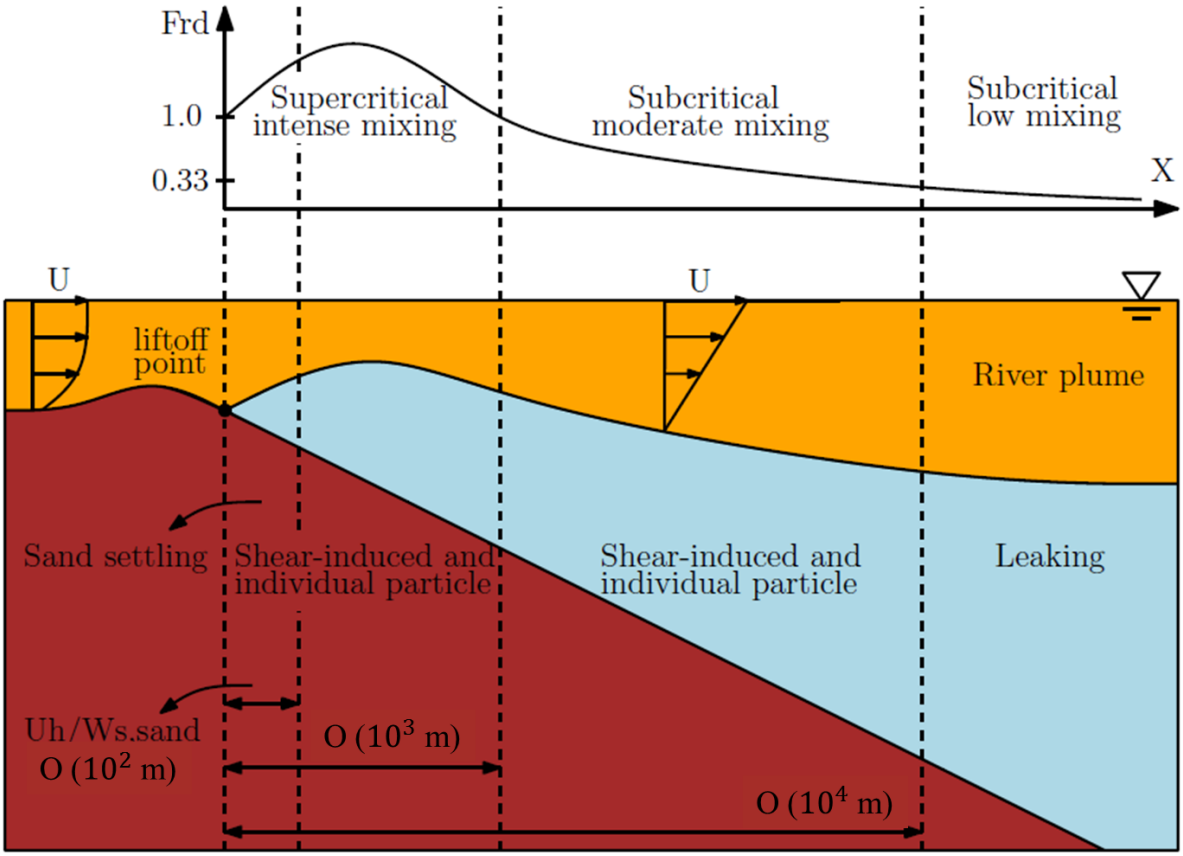

Figure 4.6: Schematic of a river plume highlighting where various sediment removal mechanisms may be operating along the length of the plume, and the relative magnitude of each

occurs when there is no interfacial mixing between the two layers (Hoyal et al., 1999b). Interactions of the shear instabilities with the salt interface (mixing and entrainment) disturb the interface constantly, and prevent formation of the unstable interface layer. We suggest that the shear-induced particle entrainment ceases and the potential for leaking commences at Ri on the order of 10; where entrainment efficiently ceases (Christodoulou, 1986). At this point (crossshore distances on the order of 10^4 m), the interfacial mixing diminishes, the interface layer forms, and leaking commences. Therefore, leaking is not expected in the

near-field region (the first few km) of a typical river plume.

4.5 Conclusions

Settling driven gravitational instabilities (leaking) and shear instabilities are significantly different in nature, and in the conditions that lead to dominance of one over the other. In the case of leaking, dynamics are controlled by formation of the gravitationally unstable interface layer that breaks away in the form of small descending packets of fluid and sediment (leaks). The resultant effective settling velocity is nearly independent from individual particles, and is a strong function of the plume concentration. However, in case of shear instabilities, no such band of heightened density, and no significant alteration to the physics of settling are observed. In this case, sediment removal takes place due to the individual particle settling plus a shear-induced diffusive process.

The magnitude of shear-induced settling velocity is the greatest near the river mouth, where the Richardson number is the lowest, and decreases in the crossshore direction as the Richardson number grows. However, the share of that in the overall settling rate increases in the crossshore direction, since sand and large particulates deposit near the inlet and only small particles (with relatively low settling velocity) remain as the plume propagates. The magnitude of the leak effective settling velocity depends on the plume concentration at the time of occurrence of leaking, which is in turn dependent on its initial value and its decay rate. Therefore, leaking only becomes considerable at high concentrations where the descent rates of the leaks are greater than that of individual particles. In general, comparisons among different process rates suggests that use of the developed empirical relations

(equations 4.2-4.4) in a predictive way relies on pre-calibrated or determined constants, K_l and K_t. Therefore, the implementation of these empirical relations needs further work to understand the dependence of the constants on the physical conditions.

A typical river plume can be broken into three regions in the crossshore direction. Immediately after the lift off point, the Richardson number is lower than one, the plume is supercritical, and the sediment removal takes place due to the individual particle and the shear-induced settling mechanisms. This region is typically in the order of O(10^3) m long. As the Richardson number grows above unity, the plume becomes subcritical, and intensity of the interfacial mixing reduces. In the subcritical region, individual particle settling in addition to the shear-induced settling are still the two mechanisms that remove the sediment from the plume. Note that the sand deposits very close to the river mouth, so no sand is expected in the subcritical region. The third region starts when the interfacial mixing diminishes, the interface layer forms, and the leaking commences. We suggest that this happens once the Richardson number grows larger than 10, and fluid entrainment becomes negligible. However we believe, further research is required to draw distinct bounds on the Richardson numbers that lead to occurrence of leaking.

Bibliography

Blanchette, F. and Bush, J. W. M. (2005). Particle concentration evolution and sedimentation-indiced instabilities in a stably stratified environment. *Physics of Fluids*, 17:073302.

Burns, P. and Meiburg, E. (2012). Sediment-laden fresh water above salt water: linear stability analysis. *Journal of Fluid Mechanics*, 691:279–314.

Burns, P. and Meiburg, E. (2015). Sediment-laden fresh water above salt water: nonlinear simulations. *Journal of Fluid Mechanics*, 762:156–195.

Chen, C. F. (1997). Particle flux through sediment fingers. *Deep Sea Research*, 44, No. 9-10:1645–1654.

Chen, F., MacDonald, D. G., and Hetland, R. D. (2009). Lateral spreading of a near-field river plume: Observations and numerical simulations. *Journal of Geophysical Research*, 114:C07013.

Chen, S.-N., Geyer, W. R., Sherwood, C. R., and Ralston, D. K. (2010). Sediment transport and deposition on a river-dominated tidal flat: An idealized model study. *Journal of Geophysical Research*, 115(C10040).

Christodoulou, G. C. (1986). Interfacial mixing in stratified flows. *Journal of Hydraulic Research*, 24:77–92.

Dyer, K. R. (1989). Sediment processes in estuaries: future research requirements. *Journal of Geophysical Research*, 94(C10):14327–14339.

Geyer, W. R., Hill, P. S., and Kineke, G. C. (2004). The transport, transformation and dispersal of sediment by buoyant coastal flows. *Continental Shelf Research*, 24(7-8):927 – 949.

Geyer, W. R. and Smith, J. D. (1987). Shear instability in a highly stratified estuary. *Journal of Physical Oceanography*, 17:1668–1679.

Gladstone, C. and Pritchard, D. (2010). Patterns of deposition from experimental turbidity currents with reversing buoyancy. *Sedimentology*, 57:53–84.

Green, T. (1987). The importance of double diffusion to the settling of suspended material. *Sedimentology*, 34:319–331.

Harris, C. K., Traykovski, P. A., and Geyer, W. R. (2005). Flood dispersal and deposition by near-bed gravitational sediment flows and oceanographic transport: A numerical modeling study of the Eel River shelf, northern California. *Journal of Geophysical Research*, 110(C09025).

Henniger, R. and Kleiser, L. (2012). Temporal evolution, morphology, and settling of the sediment plume in a model estuary. *Journal of Physics of Fluid*, 24:086601.

Hetland, R. D. (2010). The effects of mixing and spreading on density in near-field river plumes. *Dynamics of Atmospheres and Oceans*, 49, Issue 1:37–53.

Hetland, R. D. and MacDonald, D. G. (2008). Spreading in the near-field merrimack river plume. *Ocean Modeling*, 21:12–21.

Hill, P. S., Milligan, T. G., and Rockwell Geyer, W. (2000). Controls on effective settling velocity of suspended sediment in the Eel River flood plume. *Continental Shelf Research*, 20(16):2095–2111.

Horner-Devine, A. R., Hetland, R. D., and MacDonald, D. G. (2015). Mixing and transport in coastal river plumes. *Annual Revew of Fluid Mechanics*, 47:569–594.

Hoyal, D. C. J. D., Bursik, M. I., and Atkinson, J. F. (1999a). The influence of diffusive convection on sedimentation from buoyant plumes. *Marine Geology*, 159(1-4):205 – 220.

Hoyal, D. C. J. D., Bursik, M. I., and Atkinson, J. F. (1999b). Settling-driven convection: A mechanism of sedimentation from stratified fluids. *Journal of Geophysical Research*, 104:7953–7966.

Kilcher, L. F., Nash, J. D., and Moum, J. N. (2012). The role of turbulence stress divergence in decelerating a river plume. *Journal of Geophysical Research*, 117:C05032, doi:10.1029/2011JC007398.

MacDonald, D. G., Goodman, L., and Hetland, R. D. (2007). Turbulent dissipation in a near-field river plume: A comparison of control volume and microstructure observations with a numerical model. *Journal of Geophysical Research*, 112:C70026.

Manning, A. and Schoellhamer, D. (2013). Factors controlling floc settling velocity along a longitudinal estuarine transect. *Marine Geology*, 345:266–280.

Maxworthy, T. (1999). The dynamics of sedimenting surface gravity currents. *Journal of Fluid Mechanics*, 392(1):27–44.

McCool, W. W. and Parsons, J. D. (2004). Sedimentation from buoyant fine-grained suspensions. *Continental Shelf Research*, 24:1129–1142.

Mulder, T. and Syvitski, J. P. M. (1995). Turbidity currents generated at river mouths during exceptional discharges to the world oceans. *Journal of Geology*, 103(3):285–299.

Nowacki, D. J., Horner-Devine, A. R., Nash, J. D., and Jay, D. A. (2012). Rapid sediment removal from the columbia river plume near field. *Continental Shelf Research*, 35:16–28.

Parsons, J. D., Bush, J. W. M., and Syvitski, J. P. M. (2001). Hyperpycnal plume formation from riverine outflows with small sediment concentrations. *Sedimentology*, 48(2):465–478.

Parsons, J. D. and Garcia, M. H. (2000). Enhanced sediment scavenging due to double-diffusive convection. *Journal of Sedimentary Research*, 70(1):47–52.

Strom, K. and Keyvani, A. (2011). An explicit full-range settling velocity equation for mud flocs. *Journal of Sedimentary Research*, 81:921–934.

Strom, K. and Keyvani, A. (2016). Flocculation in a decaying shear field and its implications for mud removal in near-field river mouth discharges. *Journal of Geophysical Research, Oceans*, 121:doi:10.1002/2015JC011169.

Syvitski, J. P., Skene, K. I., Nicholson, M. K., and Morehead, M. D. (1998). Plume1.1: Deposition of sediment from a fluvial plume. *Computers and Geosciences*, 24:159–171.

Winterwerp, J. C. (1998). A simple model for turbulence induced flocculation of cohesive sediment. *Journal of Hydraulic Research*, 36(3):309–326.

Yu, X., Hsu, T.-J., and Balachandar, S. (2013). Convective instability in sedimentation: linear stability analysis. *Journal of Geophysical Research*, 118:256–272.

Yu, X., Hsu, T.-J., and Balachandar, S. (2014). Convective instability in sedimentation: 3d numerical study. *Journal of Geophysical Research: Oceans*, 119:8141–8161.

Yuan, Y. and Horner-Devine, A. R. (2013). Laboratory investigation of the impact of lateral spreading on buoyancy flux in a river plume. *Journal of Physical Oceanography*, 43:2588–2610.

5 Conclusions

5.1 Summary of Key Findings

Four main findings came out of the stagnant stratification tank experiments of Chapter 2. The first is that flocculation of mud leads to higher settling velocities than would be present without flocculation and therefore the dominance of settling-driven leaking and Rayleigh-Taylor interface instabilities over double-diffusive instabilities. The second conclusion is that the velocity of settling driven descending plumes is not dependent on the initial bulk stability ratio of the two-fluid system. Instead, it is dependent primarily on the concentration of the sediment in the buoyant upper layer and can be very well described by a linear function. Thirdly, for the experimental conditions tested, the effective settling velocities show that downward flux of sediment from the upper layer is on the same order as that predicted from individual floc settling velocity. However, the downward flux also shows systematic deviation with concentration from that predicted by floc settling velocity. The functionality of this deviation is directly in line with the changes observed in the instability generated plume decent speed with concentration. This leads us to conclude that removal rates of sediment are influenced by interface instabilities. A fourth key outcome of Chapter 2 was the development of a simple model for predicting the effective settling velocity based on equations for the plume descent speed and the fractional area experiencing leaking. Relations for these

two key variables were developed using a simple, cylinder-based force balance that yielded the basic functionally of the plume descent rate, and a thermal-analog critical Grashof relations coupled with geometry and the assumption of constant diameter instabilities. Combining these two relations gives the effective settling velocity of the mixture due to settling-driven convection as being proportional to $C^{13/9}$.

The data from the stratified flume experiments of Chapter 3 showed that under the effects of shear instabilities, the effective settling velocities were equal to or higher than, the individual particle settling velocities. The discrepancy between the two velocities, defined as the shear-induced settling velocity, increased with increases in plume velocity. Under steady-state conditions, no wholesale leaks or breakaway packets of fluids and sediment were observed. Instead, we observed that some particles were ejected from the base of the plume when turbulent structures, from within the flow, bombarded the stratification interface. This observation, coupled with a lack of dependence of the shear-induced settling velocity on plume concentration, leads us to conclude that the enhancement of sediment removal is driven by interfacial mixing. This shear or turbulence-enhanced removal was found to increase with decreases in the Richardson number. Based on the empirical data, and the visual observations of the role of turbulent interface disturbances, we proposed a conceptual model for the prediction the turbulence, or shear-induced, settling velocity that is proportional to URi^{-2}. This scaling was also applied to the historic field and laboratory data with good results. If the constant of proportionality can be determined for a given plume, then the total effective settling velocity can be calculated as a combination of the

individual particle settling velocity and the shear-induced settling velocity.

In the comparison presented in Chapter 4 between the settling driven gravitational instabilities (leaking) and shear instabilities, it was noted that the process of sediment removal is significantly different under the effects of each of these mechanisms. In the case of leaking, dynamics are controlled by formation of a gravitationally unstable interface layer that breaks away in the form of small descending packets of fluid and sediment (leaks). However, in case of shear instabilities, no such band of heightened density is observed, and sediment removal takes place due to the individual particle settling plus a shear-induced diffusive process. Three main conclusions based on the comparisons among different process rates in Chapter 4 were made. The first is that the magnitude of shear-induced settling velocity is the greatest near the river mouth, where the Richardson number is the lowest, and decreases in the crossshore direction as the Richardson number grows. However, its share in the overall settling rate increases in the crossshore direction since sand and large particulates deposit near the inlet, leaving only small particles (with relatively low settling velocity) in the plume as it propagates basinward. Secondly, it was found that leaking-driven effective settling velocities only becomes considerable at high concentrations where the descent rates of the leaks are greater than that of individual particles. The third key conclusion was that use of the developed semi-empirical relations in a predictive way relies on pre-calibrated or determined proportionality constants. Therefore, the implementation of these empirical relations needs further work to understand the dependence of the constants on the physical conditions.

Finally, in the light of the conclusions drawn from this study, it is suggested that a typical river plume can be conceptually broken into three Richardson number zones in the crossshore direction that have different vertical sediment flux behavior. Immediately after lift off, the plume is supercritical, and the sediment removal takes place due to the individual particle and the shear-induced settling mechanisms. This region (region 1) is typically on the order of O(10^3) m long. As the plume propagates further, intensity of the interfacial mixing reduces and the plume becomes subcritical. In the subcritical region (region 2), individual particle settling and shear-induced settling are still the two mechanisms that remove the sediment from the plume. However, no sand is expected in the subcritical region, since sand will likely deposit close to the river mouth (typically on the order of O(10^2) m far). Therefore, within the subcritical region 2, it is likely that shear-induced settling will provide a significant contribution compared to the individual or floc settling until Richardson rises above 2.5-3. For the remainder of region two, where $3 < Ri < 10$, individual floc settling likely dominates. The third region starts when the interfacial mixing nearly vanishes. At this point, it is possible for an interface layer to develop as individual particles and flocs settle into the lower layer. If enough sediment makes it out to this distance, it is possible that leaks could then form from the interface layer. We suggest that this happens once the Richardson number grows to about a value of 10, i.e. the value when fluid entrainment ceases. However, further research is required to draw distinct bounds on the Richardson numbers that lead to occurrence of leaking.

Here, I listed some of the main limitations of the work presented in this dissertation.

(1) All of our experiments were conducted at isothermal condition where no temperature difference exists between the two layers of fluid. This was mainly done to suppress double diffusive fingering. However, natural conditions will also likely exhibit some form of thermal stratification. (2) In all of the experiments, a single type of sediment (pure Kaolinite clay) with similar primary particle size distribution was used. (3) By design, the flume experiments were laterally confined. In natural discharges, hypopycnal plumes are free to expand laterally due to shear and buoyant spreading. While it has been shown that the strength of turbulent mixing at the base of the plume is independent of lateral confinement, the overall hydraulics of the plume in the crossshore direction are different in confined and unconfined conditions. (4) The flume experiments all fall in the subcritical flow range, while natural plumes are usually supercritical in the near-field region. Because of the differences in mixing between super and subcritical regimes, it is hard to generalized the results from the experimental work to supercritical flows. (5) The effects of surface and internal waves and local currents are suppressed in our experiments, analysis, and model development. It is unclear as to whether or not the turbulence that is generated due to the surface waves impacts the nature of interface instabilities and the deposition flux. For the internal waves however, it is suspected that interfacial mixing will be boosted due to the turbulence that is generated at the interface.

To extent the utility of this study's findings, it will be necessary to understand the dependence of the calibration constants used with the semi-empirical relations on physical conditions. If values for these constants can be linked to physical conditions, then the scaling relationships could be implemented in computational models to improve predictions of

vertical sediment flux from river plumes. Also, more research is needed to determine whether or not the proportionality between the non-dimensional shear-induced settling velocity, δ_s, (sediment entrainment ration) and the Richardson number with an exponent of -2 holds when the plume is supercritical. This is of interest since previous work has shown that for saltwater entrainment, the exponent in the proportionality changes depending on whether the plume is subcritical or supercritical. As far as the sediment flux zonation, further research is required to illustrate the conditions leading to commencement of leaking. Here, it is suggested that occurrence of leaking should be linked to cessation of interfacial mixing, and hence, a growth of the Richardson number above a certain value. However, we still lack a distinction on the Richardson numbers that lead to occurrence of leaking.

5.2 Presentations and Publications

Findings from this study were presented in following four conferences:

1. Rouhnia, M., Strom, K., and Liu, X., (2016). Experiments and modeling of density instabilities driven by interface shear and their influence on removal of sediment from buoyant plumes. Published in the proceedings of the International Conference on Fluvial Hydraulics (River Flow 2016), St. Louis, USA, 11-14 July 2016. Eds. G. Constantinescu, M. Garcia, and D. Hanes.

2. Rouhnia, M. and Strom, K., (2015). Localized density instabilities driven by interface shear and their influence on removal of sediment from buoyant plumes. Abstract ID: EP21C-0931, AGU Fall Meeting 2015, San Francisco, California.

3. Strom, K. and Rouhnia, M., (2014). Comparison of individual mud floc settling rates and particle settling driven gravitational instabilities in a muddy freshwater suspension overlying saltwater. Abstract ID: 654, EWRI 2014, Portland, Oregon.

4. Rouhnia, M. and Strom, K., (2014). Density driven removal of sediment from a buoyant muddy plume. Abstract ID: EP31B-3527, AGU Fall Meeting 2014, San Francisco, California.

The components of the work have been published, or are under preparation for publication, in three journal papers as follows:

1. Rouhnia, M. and Strom, K., (2016). An analysis of the sediment removal mechanisms and rates at play on the length of a river mouth plume. Under preparation to submit to Continental Shelf Research.

2. Rouhnia, M. and Strom, K., (2016). Sedimentation from buoyant muddy plumes in the presence of shear instabilities: An experimental study. Under review, submitted to Journal of Geophysical Research, Oceans.

3. Rouhnia, M. and Strom, K., (2015). Sedimentation from flocculated suspensions in the presence of settling driven gravitational interface instabilities. Journal of Geophysical Research, Oceans, Vol: 120, 6384-6404.